PREFERENTIAL MICROSTRUCTURAL PATHWAYS OF STRAIN LOCALIZATION WITHIN NICKEL AND TITANIUM ALLOYS
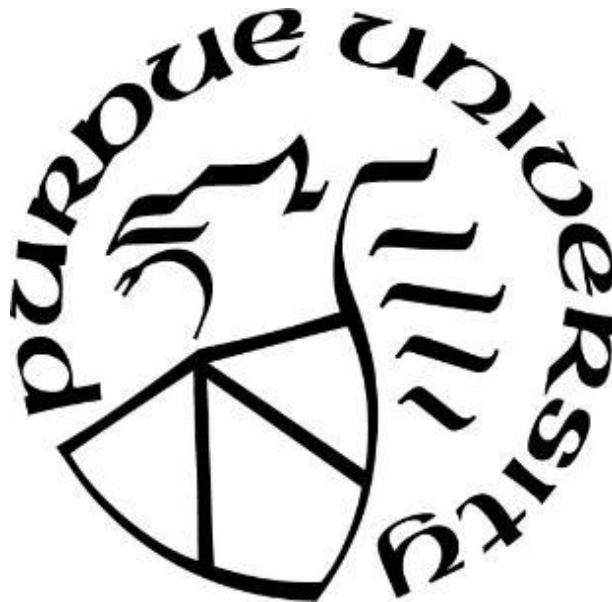
by

John Rotella

A Dissertation

Submitted to the Faculty of Purdue University

In Partial Fulfillment of the Requirements for the degree of

Doctor of Philosophy

School of Materials Engineering

West Lafayette, Indiana

December 2021

THE PURDUE UNIVERSITY GRADUATE SCHOOL
STATEMENT OF COMMITTEE APPROVAL

Dr. Michael D. Sangid, Co-Chair

School of Aeronautics and Astronautics

Dr. Rodney Trice, Co-Chair

School of Materials Engineering

Dr. Carol Handwerker

School of Materials Engineering

Dr. David F. Bahr

School of Materials Engineering

Approved by:

Dr. David F. Bahr

To Kelsey and Declyn

ACKNOWLEDGMENTS

TABLE OF CONTENTS

LIST OF TABLES

LIST OF FIGURES

NOMENCLATURE

ALA	As-large-as
AOI	Area of Interest
BSE	Backscatter Electron
CTB	Coherent Twin Boundary
DB	Deformation Band
DBD	Deformation Band Deviation
DIC	Digital Image Correlation
DOF	Degree of freedom
EBSD	Electron Backscatter Diffraction
FCC	Face-Centered Cubic
GB	Grain Boundary
HAGB	High Angle Grain Boundary
HAS	High Stress Amplitude
HCP	Hexagonal Close-Packed
HEDM	High Energy Diffraction Microscopy
ISI	Incremental Slip Intensity
LSA	Low Stress Amplitude
MPSS	mesoscale plastic strain sizing
MSS	Maximum Shear Stress
PSB	Persistent Slip Band
RVE	Representative Volume Element
SEM	Scanning Electron Microscope

EQUATION VARIABLES

$\overline{A}_{DB}$	Average area of a deformation band
$\overline{DB}_{AF}$	Average deformation band area fraction
$\widetilde{r}_\emptyset$	Overall mechanical error
$\dot{\gamma}_o$	Reference shear strain rate
$\overline{\gamma}_{RVE}^{max}$	Average maximum in-plane shear strain within a specific RVE
$\sigma_{pq_{Converged}}$	Converged stress state
b_{in}	Incident dislocation Burgers vector
b_{out}	Outgoing dislocation Burgers vector
b_r	Residual Burgers vector
b^α	Slip direction
DB_{AF}	Pixel fraction of deformation bands relative to total area
D_{ij}	Deformation rate tensor
$d\varepsilon_{ij}^p$	Change in plastic strain between deformation states
$E_{Total}^{residual}$	Residual combined global strain
$\mathcal{M}_{ij}^\alpha \ \& \ \mathcal{M}_{pq}^\alpha$	Schmid tensors
n_{DB}	Number of deformation bands
n_{ep}	Number of RVE edge lengths
n_{exp}	Number of experiments
n^α	Slip plane normal
$\widetilde{r}$	Average macroscopic error
t_x	Grain boundary tangent in the x-direction
t_y	Grain boundary tangent in the y-direction
$u'_{i_{resolved}}$	Grain boundary sliding magnitude
$u_{resolved}$	Resolved displacements along a Grain Boundary
u_x	Grain boundary normal vector in the x-direction
u_y	Grain boundary normal vector in the y-direction
$\Gamma_{Applied}^{Shear}$	Global shear strain

γ^{max}	Maximum in-plane shear strain
$E_{Applied}^{Tension}$	Global tensile strain
E_{Total}	Combined global strain
ε_{xx}	Axial strain
ε_{xy}	In-plane shear strain
ε_{yy}	Transverse strain
ε_{zz}	Out-of-plane strain
σ_{ij}	Stress tensor
$\bar{\tau}$	Reference stress
τ^{α}	Resolved shear stress
$d\gamma$	shear increment or incremental slip
m'	Geometric alignment factor between slip systems
n	Rate sensitivity coefficient
r	Reasonable deviation
W	Work as established by the principle of minimum work
Ω	Strain coaxiality

ABSTRACT

Modern structural materials utilize tailored microstructures to retain peak performance within the most volatile operating conditions. Features such as grain size, grain boundary (GB) character and morphology and secondary phases are just a few of the tunable parameters. By tailoring these types of microstructural features, the deformation behavior of the material is also altered. The localization of plastic strain directly correlated to material failure. Thus, a systematic approach was utilized to understand the effect of microstructural features on the localization of plastic deformation utilizing digital image correlation (DIC). First, at the macroscopic scale, strain accumulation is known to form parallel to the plane of maximum shear stress. The local deviations in the deformation pathways at the meso-scale are investigated relative to the plane of maximum shear stress. The deviations in the deformation pathways are observed to be a function of the accumulated local plastic strain magnitude and the grain size. Next, strains characterized via DIC were used to calculate a value of incremental slip on the active slip systems and identify cases of slip transmission. The incremental slip was calculated based on a Taylor-Bishop-Hill algorithm, which determined a qualitative assessment of deformation on a given slip system, by satisfying compatibility and identifying the stress state by the principle of virtual work. Inter-connected slip bands, between neighboring grains, were shown to accumulate more incremental slip (and associated strain) relative to slip bands confined to a single grain, where slip transmission did not occur. These results rationalize the role of grain clusters which lead to intense strain accumulation and thus serve as potential sites for fatigue crack initiation. Lastly, at GB interfaces, the effect of GB morphology (planar or serrated) on the cavitation behavior was studied during elevated temperature dwell-fatigue at 700 °C. The resulting γ' precipitate structures were characterized near GBs and within grains. Along serrated GBs coarsened and elongated γ' precipitates formed and consequently created adjacent regions that were denuded of γ' precipitates. Dwell-fatigue experiments were performed at low and high stress amplitudes which varied the amount of imparted strain on the specimens. Additionally, the regions denuded of the γ' precipitates were observed to localize strain and to be initial sites of cavitation. These results present a quantitative strain analysis between two GB morphologies, which provided the micromechanical rationale for the increased proclivity for serrated GBs to form cavities.

16

1. INTRODUCTION

1.1 Microstructural features and strain accumulation

An object subjected to a stress may experience reversible and irreversible types of deformation. Reversible deformation is referred to as elastic deformation and is relieved when the applied stress is removed. Conversely, irreversible deformation or plastic deformation remains following the removal of the applied stress. The accumulation of plastic deformation within materials has shown to be a precursor to failure[1]. Thus, identification and characterization of material features which accelerate or localize plastic deformation are of interest, in order to understand where material failure is likely to occur.

Plastic deformation occurs across many length scales. At the macroscopic scale, plastic deformation is most noticeable when a material begins to neck or locally reduce its cross section when subjected to a stress. Engineering materials possess complex microstructural features to resist the onset of plastic deformation. Specifically, material classes of Ni-based superalloys and titanium alloys employ strengthening mechanisms which span many length scales, such as crystallographic orientation, grain size, grain boundary (GB) morphologies and character, and secondary particle size, distribution, and volume fraction. In a component, the aforementioned microstructural features would be tailored based on the anticipated loading conditions and service life.

Modern turbine engines, specifically turbine discs offer a prime example of tailored microstructure. Due to the large mechanical gradients at the bore and thermal gradients at the rim, constant microstructural features, such as grain size, produce performance trade-offs in either location. In order to combat these trade-offs, the dual-microstructure turbine disc was conceived which utilizes fine grains in the bore location to provide strength and crack growth resistance and coarse grains at the rim region to provide increased creep resistance[2]. To produce this dual-microstructure disc the thermal history is controlled independently for the bore and rim region. In addition to grain size, the underlying precipitate phase and GB morphology are also affected. Each microstructural modification has an impact on how the material accumulates deformation and thus performs. In this thesis, the impact of microstructural features will be addressed from the perspective of plastic strain accumulation.

It is a well-accepted concept that deformation in metals is attributed to the movement of dislocations along slip planes in distinct slip directions. Dislocations emission is classically thought of as a Frank-Read source producing circular strings of dislocations[3], but can also include absorption and emission from a GB or other defect. Due to these observations, strain accumulation must occur heterogeneously throughout a structure. This is important because, even though a part or component could be operating far below its yield or max allowable stress, it could still fail due to local weak links within its given microstructure. Where a weak link is a location such as a void, particle or neighborhood of grains that have favorable conditions for strain build up and crack initiation. This phenomenon can be seen commonly in parts such as drive shafts for automobiles and jet engine turbine discs. Since these structures and those like them operate in a cyclic fashion, it allows the material to incrementally accrue plastic deformation at these weak links.

This information is useful when we talk about how dislocations start to merge to form persistent slip bands (PSBs). PSBs have been observed to form in superalloys[4–6]. During the formation of slip bands, the spacing between dislocations is decreased due to the repeated forward and backward movement of dislocations on a given plane. This repeated motion and opposite signs of dislocations makes it possible for them to align such that their energy is minimized[7]. A slip band will impinge at a surface or GB leading to the formation of an intrusion/extrusion. Extrusions cause stress concentrations and eventually crack formation[1,8,9] or void nucleation[10].

1.2   Gap statement

The primary research objective of this thesis is to quantify accelerated plastic strain accumulation in polycrystalline materials relative to microstructural features. Specifically, grain size, GBs, grain clusters, GB character and morphology. First, a thought experiment of the simplest case, wherein plastic strain accumulation occurs within a single crystal. In this case, none of the prior features are present. Plastic strain accumulation occurs along the slip system(s) which have a resolved shear stress that is greater than the critical value to cause slip[11]. However, most engineering materials are a departure from the simple case outlined above and present an unclear cause and effect relationship between plastic strain accumulation and the microstructural features responsible for their performance.

First, a simple Ti7Al model material with only high angle grain boundaries (HAGB) will be studied. Previous studies have implemented techniques such as DIC [12], EBSD [13] or combinations

of both techniques [14] to study deformation across length scales. In uniaxial deformation, DIC studies have observed partitioning of strain accumulation into banded structures which form parallel to the plane of maximum shear stress (MSS) [14,15]. However, the direct impact of microstructural features on the development of the macroscopic deformation pathways have yet to be uncoupled from the macroscopic loading conditions.

The next step is to investigate more complex microstructural features. Two previously identified features are the grain cluster and GBs with differing morphology. The first feature, grain clusters, are defined as aggregates of grains which act collectively to propagate plastic deformation through a microstructure and are subsequently nucleation locations of fatigue cracks [16]. While the behavior of a grain cluster has been documented, the additional strain accumulation caused within grain clusters due to inter-connected slip has not been shown relative to the isolated deformation of one or two grains. The second feature, GB morphology, more specifically serrated GBs are thought to slow the accumulation of creep strain[17] and elevated temperature fatigue crack growth[18]. GB serrations are created via the coarsening of a secondary phase, such as the γ' precipitate phase [19] at the GB interface. While GB serrations have documented benefits, the local GB deformation, and its relationship to other detrimental behaviors, such as the formation of cavities, remains unclear. In order to investigate grain clusters and GB morphology an engineering material, RR1000, will be utilized, due to the ability to tailor different aspects of the microstructure.

1.3   Research Contributions

There are three research contributions covered in this thesis. First, by removing the effect of the plane of MSS, the influence of microstructural features, such as grain size, grain orientation and GBs, on the developing primary and secondary deformation pathways can be assessed over many grains. Where the primary deformation pathways are aligned with the plane of MSS, and the secondary deformation pathways are any deviations from the plane of MSS. Secondly, the additional strain accumulation is quantified for grain clusters relative to other grain configurations at various length scales; investigating the intensity of slip within each slip band, progressing to the effect that slip transmission has on slip intensity, and finally analyzing the strain accumulation within groups of grains based on inter-connected slip bands. Lastly, the plastic strain accumulation occurring along the GBs are correlated with respect to the length fraction of GBs, which form

cavities and the underlying precipitate structure. These objectives are accomplished by implementing a full field deformation tracking technique known as digital image correlation (DIC) and the spatial information about the material. To date, no such similar measurements have been produced to address these three contributions.

1.4   Thesis outline

This thesis is organized into 7 chapters. Below, each chapter is summarized by contribution or topic.

Chapter 1 examines an overview of material deformation and the types and length scales of material strengthening mechanisms.

Chapter 2 presents a targeted literature review of deformation across length scales, specifically the effect of various microstructural features on the development of deformation pathways within a given microstructure.

Chapter 3 presents the experimental methods and characterization techniques utilized during this thesis. The topics of mechanical loading, material pedigree, electron imaging and DIC are discussed.

Chapter 4 examines the formation of deformation pathways within a model material, Ti7Al, during tension torsion loading, due to GBs, crystallographic orientation, and grain size. The local deviations in the deformation pathways are examined and the size of the developed deformation pathways are reported. Lastly, a representative volume element to encompass the identified deformation pathways is discussed relative to past literature investigations.

Chapter 5 explores the role of inter-connected slip between neighboring grains and the resulting slip intensity in an engineering alloy, RR1000. The specific methodology for this calculation is also presented. Lastly, strain co-axiality or the direction of strain accumulation relative to the applied load is correlated with slip inter-connectivity.

Chapter 6 presents the proclivity of cavity formation at GBs with differing morphologies during elevated temperature dwell fatigue in an engineering alloy, RR1000. A detailed description of the γ' precipitates at the GBs and within the bulk of the material are presented.

Chapter 7 summarizes the conclusions of this research. Lastly, possible future areas of research are listed.

2. LITERATURE REVIEW

Within this chapter, microstructural features and their impact on deformation pathways are reviewed. The first consideration in the development of deformation pathways is the global loading condition, as the developed plane of MSS plays a critical role in the development of deformation pathways within a material. Next, slip band continuity is reviewed and its detrimental effect on fatigue life. Lastly, the effect of GB morphology during elevated temperature deformation is reviewed.

2.1 Macroscopic deformation continuity via deformation band formation

The development of the deformation pathways within polycrystalline materials is a multi-scale process, wherein the macroscopic loading conditions and local microstructure dictate the mechanical response [1,20]. At the nanoscale, plastic deformation manifests as arrays of dislocations, i.e., slip bands within the material. Dislocations progress to GBs wherein they experience cross-slip, direct transmission, indirect transmission or no transmission [21]. Deformation bands, DBs, are created when slip events become inter-connected through many grains within the microstructure.

At the macroscopic scale, the primary pathways of deformation occur parallel to the plane of MSS [22] as determined by the loading condition and calculated through a Mohr's circle analysis [23–25]. These deformation pathways consist of both crystallographic and non-crystallographic deformation based on the local strain magnitudes [24,25]. In many cases, a slip plane is not directly aligned with the plane of MSS, and thus slip events across neighboring grains may be required, such that their cumulative deformation corresponds to the plane of MSS [26,27].

At the microstructural scale, the largest degree of deformation is observed to localize near the GBs [14]. Compatibility constraints and dislocation motion increase stress and promote deformation near GBs. Compatibility stresses are caused by neighboring grains with different crystallographic orientations, and localized deformations in adjacent grains [28]. Additional stresses are experienced due to dislocation pile-ups at a GB [29]. These complex stresses are relieved through slip transmission or the activation of an adjacent slip system. These slip events create a network of inter-connected slip events, which have shown to be key features in crack initiation and material failure [9,16].

In addition to GBs, other microstructural features such as grain size [16,30–32] and crystallographic texture [33–38] are important factors influencing the local deformation behavior. Hall [30] and Petch [31] observed material strength was inversely proportional to grain size. Deformation in smaller grains is more difficult due to the shorter mean free path for dislocation motion between GBs. As a consequence of dislocation pile-up, back stresses are imposed on the primary slip systems which cause secondary slip activity and work hardening [39]. In titanium alloys, a grain is termed "hard" or soft" based on the c-axis orientation relative to the loading axis, where hard grains have a c-axis that are near parallel to the loading direction. Conversely, soft grains have a c-axis that is nearly perpendicular to the loading direction and are well oriented for basal slip and prismatic slip. At the bulk scale, Evans et al. [38] observed crack initiation of textured materials is controlled by the basal planes orientation relative to the plane of MSS, where better alignment resulted in shorter material life. At the microscale, Harr et al. [37] observed grains well oriented for basal slip create long range slip traces which can traverse over 100 grain diameters.

2.2   Mesoscale slip continuity via inter-connected slip

Materials retaining high strength capabilities at elevated temperatures are of great importance to the aerospace gas turbine industry. Ni-based superalloys are one such class of materials, which exhibit this unique behavior due to their complex microstructure, including tailored precipitates [40,41], grain size optimization (for mechanical loading [42] and temperature conditions [2]), and GB distributions, predominantly high length fractions of annealing twin boundaries [43]. Strain localization is a precursor to fatigue crack initiation [1]. Identifying features at the microstructural scale contributing to strain accumulation is critical to establish a physical understanding of the microstructural configurations that may promote cracking. During fatigue of Ni-based superalloys, strain accumulation occurs heterogeneously along discrete slip bands [44]. Slip bands, which mediate dislocation motion, interact with the aforementioned complex microstructural elements, which result in strain localization and subsequent crack nucleation [1]. In this study, the cyclic response of a Ni-based superalloy is examined to identify microstructural attributes that accelerate plastic strain accumulation.

One of the most influential microstructural features is grain size, as it greatly effects the performance of Ni-based superalloys [45]. Thompson and coworkers observed that a reduction in grain size increased the cycles to failure in brass [42] and also increased work hardening behavior [46].

Further, Brogdon and Rosenberger [47] experimentally observed the largest grains present in the Ni-based superalloy Waspaloy, controlled the number of cycles to failure during fatigue loading. Experimental observation [48] and statistical analysis [49] of crack initiation during fatigue loading in Waspaloy, found that grains with sizes 50% or greater than the average grain size are the most likely sites of crack initiation under varying load ratios and temperature conditions. In general, longer fatigue life is observed in materials with finer grains [42,50–54] making the largest grains, termed as-large-as (ALA) grains, weak links during fatigue loading [9]. Similar to having an ALA grain serve as a weak link, Davidson et al. [16] suggested the supergrain theory. In this work, a supergrain, also known as a grain cluster, was defined as a group of grains that are crytallographically related, based on alignment of their slip planes, such that they can act collectively to allow slip to transmit across the boundaries between each grain. Davidson et al. observed 8 of 10 intergranular cracks initiated within or at the GB of a grain cluster in Waspaloy during fatigue loading [16]. Sangid et al. [9] investigated the crack initiation behavior of grain clusters in Udimet 720 via a physically based energy balance method which accounted for the microstructure of the material. Any grain with a misorientation less than 15° relative to its neighboring grain was grouped into a grain cluster. In their set of simulations, 2-7 grains were observed to act in concert to form a grain cluster, which promoted crack initiation [9]. An outstanding question is whether the presence of a grain cluster increases the localization of strain within the microstructure.

Each grain within the bulk of the polycrystalline aggregate contains several neighboring grains with varying orientations. There are five degrees of freedom (DOF) that describe the relationship between adjacent crystals. Three rotations describe how the orientation of one crystal lattice relates to its neighbor, while the remaining two DOF describe the interface plane separating the two crystals. Each configuration, of the five DOF, results in the GB exhibiting an energy associated with the inherent area defects [55], of particular interest in this study are the coherent twin boundaries (CTB). The CTB has the lowest energy compared to other types of GBs [56]. These low energy boundaries are less likely to nucleate a dislocation and provide a strong barrier to dislocation transmission [57] for similar incident dislocation types and applied stress states relative to the GB. However, screw type dislocations have been observed to readily cross-slip through CTBs [58,59]. Grain clusters may more readily form as a result of this cross-slip transmission mechanism, due to the high length fractions of CTBs that form within Ni-based superalloys.

2.3   Elevated temperature deformation accommodation at GBs

The need for higher temperature structural materials has driven efforts to tailor the microstructural features within Ni-based superalloys. As temperature and stress demands rise, additional deformation mechanisms, such GB sliding [60] and GB cavitation,[61] may become active. GB cavitation is a precursor to intergranular failure,[18] causing debits in elevated temperature dwell-fatigue life.[62] Since GB cavitation is recognized as a preceding mechanism to final fracture, identifying the microstructural configurations and micro-mechanical fields that promote GB cavitation are important to assess the high temperature material response of Ni-based superalloys.

In the continuing effort to enhance the high temperature performance of Ni-based superalloys, the contribution of tailorable microstructural features, such as precipitate size and distribution, [4,63] grain size,[64] GB character [65] and GB morphology,[2,66] have been studied. GB morphology, specifically serrated GBs, has been observed to reduce local creep strain rates at these microstructural features [17,67] and crack growth rates [18] during dwell-fatigue loading at elevated temperatures. Formation of serrated GBs occurs during the cooling process from a solution temperature, where secondary phase particles interact with a GB.[68,69] In γ' containing Ni-based superalloys, the amplitude of the serration increases with the growth of the secondary γ' phase.[19]

However, the implementation of serrated GBs will also promote GB cavity formation,[70] due to distributions in local microstructure strength caused by the coherency loss of the γ' precipitates within the γ matrix and/or GB regions denuded of the γ' phase.[71,72] Stress concentrations along serrated GBs are thought to originate at the interface of a secondary particle, [73] where the energy to nucleate a cavity is reduced [74]. One mechanism of cavity formation, in which a slip band intersects with a precipitate, creates the sustained stresses needed to form cavities, as shown schematically in Fig. 1.[75] In addition to the above, other mechanisms for GB cavitation have been proposed, these include vacancy accumulation via diffusion [76] and GB sliding coupled with localized deformation at an interface.[77,78] Preferential damage occurs along GBs,[79,80] specifically serrated GBs develop more strain localization sites per unit of length, relative to planar GBs.[60] Additionally, GB cavitation has been shown to be correlated with the applied macroscopic strain.[81,82] High resolution electron back-scatter diffraction studies [17,83] confirm regions of large elastic strain localized along serrated GBs, but also report the suppression of cavity formation, rather than the promotion of cavitation. Despite the detailed previous analyses, the relationship between local GB deformation and cavitation remains unclear.

2.4 Polycrystal deformation models

Polycrystalline deformation models address many length scales of deformation phenomena by simulating explicit or representative deformation behavior. A representative volume element (RVE), is the minimum volume simulated that captures the ensemble mechanical behavior and was described by Hill [84]. The characteristics of a RVE were described in two parts where (i) the distribution and dispersion of the microstructural features are matched to the material simulated and (ii) the volume is large enough such that the effective properties are independent of the boundary effects. In accordance with Hill's description, RVEs are commonly sized by matching a set of microstructural descriptor distributions [85], such as grain size, texture, grain morphology, etc. Additional verification for RVEs may include matching various mechanical properties, such as yield strength and hardening rate [86]. In addition to the two common methodologies above, RVE sizing interpretation has also been investigated by matching the spatial variability of in-plane plastic strain [87] or grain-to-grain variability based on elastic strains [88]. Balzani et al. [89] proposed a methodology to size an RVE, which minimized the error in the overall macroscopic deformation response while also considering the distribution of microstructural features within the RVE. This approach differs from the aforementioned approaches because it utilizes the post experimental deformation behavior at two length scales and does not consider any of the typical microstructural descriptors. Lastly, two-point statistics (autocorrelation and, cord length distributions) are commonly utilized to characterize the spatial occurrence of features such as c-axis orientation [90] and microtextured zones [91]. However, it is noted that these functions capture the average behavior and thus they should be utilized with additional characterization methods for improved accuracy of the RVE construction.

3. EXPERIMENTAL METHODS AND CHARACTERIZATION TECHNIQUES

3.1 Mechanical loading conditions

3.1.1 Monotonic

Material behavior examined in Chapter 4 was conducted under the following loading conditions. Four tension-torsion experiments were conducted in an MTS Model 809 servo hydraulic test system with a MTS biaxial extensometer, model 632, to monitor the applied tensile and shear strains. Each specimen was loaded in stress control to the same target least squares strain, E_{Total}, of 0.6% as defined by Eq. 3.1, wherein $E_{Applied}^{Tension}$ and $\Gamma_{Applied}^{Shear}$ are the applied tensile strain and shear strain applied to the specimen, respectively.

$$E_{Total} = \sqrt{E_{Applied}^{Tension^2} + \Gamma_{Applied}^{Shear^2}} \qquad \text{Eq. 3.1}$$

Specimens were returned to 0% shear strain, to ensure a near planar surface for the DIC technique, and zero tensile load, before being removed from the load frame. Therefore, the residual macroscopic strain, $E_{Total}^{residual}$ for each specimen is different, where the $E_{Total}^{residual}$ is proportional to the applied shear strain. Tension-torsion experiments of varying ratios were conducted on 4 specimens, specific experimental conditions were torsion, tension, 2:1 tension and 2:1 torsion. Where the ratio 2:1, indicates the fraction of the applied strains. The applied strain conditions and residual strain for each specimen are shown in Table 3.1 within columns 1, 2 and 3. The last column displays the average maximum in-plane shear strain, $\overline{\gamma}^{max}$.

Table 3.1: The peak tensile strain ($E_{Applied}^{Tension}$) and shear strain ($\Gamma_{Applied}^{Shear}$) applied macroscopically to each specimen. The residual macroscopic strain of each specimen, $E_{Total}^{residual}$. The average maximum in-plane shear strain within each specimen's AOI, $\bar{\gamma}^{max}$.

	$E_{Applied}^{Tension}$	$\Gamma_{Applied}^{Shear}$	$E_{Total}^{residual}$	$\bar{\gamma}^{max}$
Torsion	0 %	0.60 %	0.20 %	0.26 %
2:1 Torsion	0.27 %	0.54 %	0.078 %	0.34 %
2:1 Tension	0.54 %	0.27 %	0.075 %	0.36 %
Tension	0.60 %	0 %	0.051 %	0.58 %

3.1.2   Fatigue

Room temperature fatigue

Material behavior examined in Chapter 5 was conducted under the following loading conditions. Specimens were loaded ex-situ using a servo-hydraulic MTS load frame with an Epsilon-3442 extensometer attached to monitor the macroscopic applied strain. The first cycle of deformation consisted of monotonic loading to 1% total strain and was conducted in displacement control in accordance with the ASTM E8 standard. From 1% total strain, the specimens were unloaded to a near-zero value of stress in load control and removed from the load frame. The maximum stress to achieve 1% total strain was recorded and used as the target stress for cycles 2 through 1000, tested in load control at 0.50 Hz, using a sine wave loading profile at an R equal to 0.1. Cyclic loading was interrupted following 1, 10, 100, and 1000 cycles to capture scanning electron microscope (SEM) images used for the DIC measurements.

Elevated temperature dwell-fatigue

Material behavior examined in Chapter 6 were conducted under the following loading conditions. Experiments were conducted inside of a JOEL 5300 SEM) under vacuum, using a modified MTI load frame with a resistive heater; further details regarding the experimental setup are discussed by Mello et al.[92] The target temperature, 700 °C, was monitored via a thermocouple

placed at the center of the gauge length, with a maximum variation of ± 10 °C. Prior to conducting the dwell-fatigue experiments, the stress-strain response of each variant microstructure was obtained through interrupted tensile testing and DIC measurements. The elastic portion of the stress-strain response was determined using the Young's modulus of the material at 700 °C and Hooke's law, while the plastic portion of strain was measured by conducting ex-situ optical DIC, over a region of 3 mm by 1 mm.

The material's tensile response informed the two stress ranges utilized during the dwell-fatigue experiments, which are referred to as a low stress amplitude (LSA) and a high stress amplitude (HSA). The LSA was macroscopically elastic, which is expected to result in concentrated strain accumulation or microplasticity within the microstructure. The maximum stress applied (385 MPa) was 75% of the proportional limit in the LSA specimen. The HSA was selected to ensure significant plasticity accumulated within the microstructure to increase the likelihood of activating the high temperature deformation mechanisms. Hence, the stress corresponding to 1% plastic axial strain was selected for each HSA condition. As expected, the specimens tested in the HSA condition experienced cyclic ratcheting. Dwell-fatigue experiments consisted of three total specimens, two with a serrated microstructure under LSA and HSA conditions, and one planar microstructure under HSA conditions. Specimens were subjected to a dwell time of 10 minutes at maximum load, with a stress ratio equal to 0.1. It should be noted that the yield stress was lower in the serrated samples as compared to the planar sample, due to the larger grain size and greater spacing between the γ' precipitates. The 0.2% offset yield was measured at 700 °C via the ex-situ DIC experiments to be 695 ± 75 MPa for the planar sample (14 $\frac{°C}{s}$ cooling rate corresponding to an average grain size of 49 μm) and 585 MPa ± 50 MPa for the serrated sample (0.7 $\frac{°C}{s}$ cooling rate corresponding to an average grain size of 60 μm). These values were in agreement with models from Rolls-Royce plc that predicted a 0.2% offset yield at 700 °C of 1082 and 889 MPa for similar cooling rates 14 and 0.7 $\frac{°C}{s}$, respectively, for coarse grain RR1000 with an average grain size of 30 μm. Correspondingly, a ~13% lower stress was required for the HSA serrated specimen (705 MPa) to achieve an equivalent axial strain compared to the HSA planar specimen (800 MPa). Table 3.2 summarizes the specimen designations and loading parameters.

Table 3.2: Specimen designations, applied stress state, and loading parameters for each of the three specimens.

Specimen designation	Applied stress condition	Other relevant testing conditions
Low stress amplitude (LSA) serrated	385 MPa	• Test temperature: 700 °C
High stress amplitude (HSA) serrated	705 MPa	• Environment: vacuum • Dwell time: 10 minutes • R = 0.1
High stress amplitude (HSA) Planar	800 MPa	

3.2   Material pedigree

3.2.1   Titanium 7 Aluminum

The material system studied within Chapter 4 was a near alpha phase titanium alloy, Ti7Al, with a hexagonal closed packed crystal structure. The Ti7Al material was cast into ingot form, hot isostatic pressed, extruded and annealed at 955 °C for 24 hours, followed by an air cool [93]. The resulting material consisted of equiaxed grains with an average grain size of 86 µm.

3.2.2   Ni-based superalloy RR1000

Tailoring microstructural feature content

The material of interest in Chapters 5 and 6 is RR1000, a powder processed, γ' strengthened, Ni-based superalloy. The development of the microstructure, especially grain size and twin fraction are sensitive to the forging temperature and strain rate [94,95]. In Chapter 5, the material was forged by ATI Forged Products Cudahy: (i) condition 1 (C1) and (ii) condition 2 (C2). The processing conditions and relevant characterization information is shown in Table 3.3.

Table 3.3: RR1000 variant, C1 and C2, processing conditions and characterized microstructural attributes.

Microstructure	Forging Temperature	Forging strain rate	Annealing conditions	Cooling rate	Grain size	Twin boundary length fraction	Low angle boundary length fraction	$\gamma'_{secondary}$ size	$\gamma'_{tertiary}$ size
C1	1100 °C	0.003 s^{-1}	1115 °C for 4 hours followed by1170 °C for 4 hours	$1\frac{°C}{s}$	57 μm	0.43	0.04	234 nm ± 78 nm	33 nm ± 14nm
C2	1020 °C	0.05 s^{-1}			38 μm	0.47	0.03	173 nm ± 77 nm	23 nm ± 4 nm

The process parameters were selected based on a process deformation map to identify pertinent microstructural features, as discussed further in [65]. The γ' precipitate structure of the RR1000 variants were revealed by etching with a modified Kallings reagent, by EOS Laboratories, which etched the γ phase. The underlying γ' structures were imaged on a FEI Quanta 3D FEG Dual-beam SEM, as shown in Figure 3.1 (a) and (b). Larger γ' precipitates were measured in C1, as shown in Figure 3.1a, in terms of the relative size of both the secondary and tertiary γ' precipitates when compared to C2, Figure 3.1b. See Table 3.3 for the quantitative sizes of the secondary and tertiary γ' precipitates in both variants.
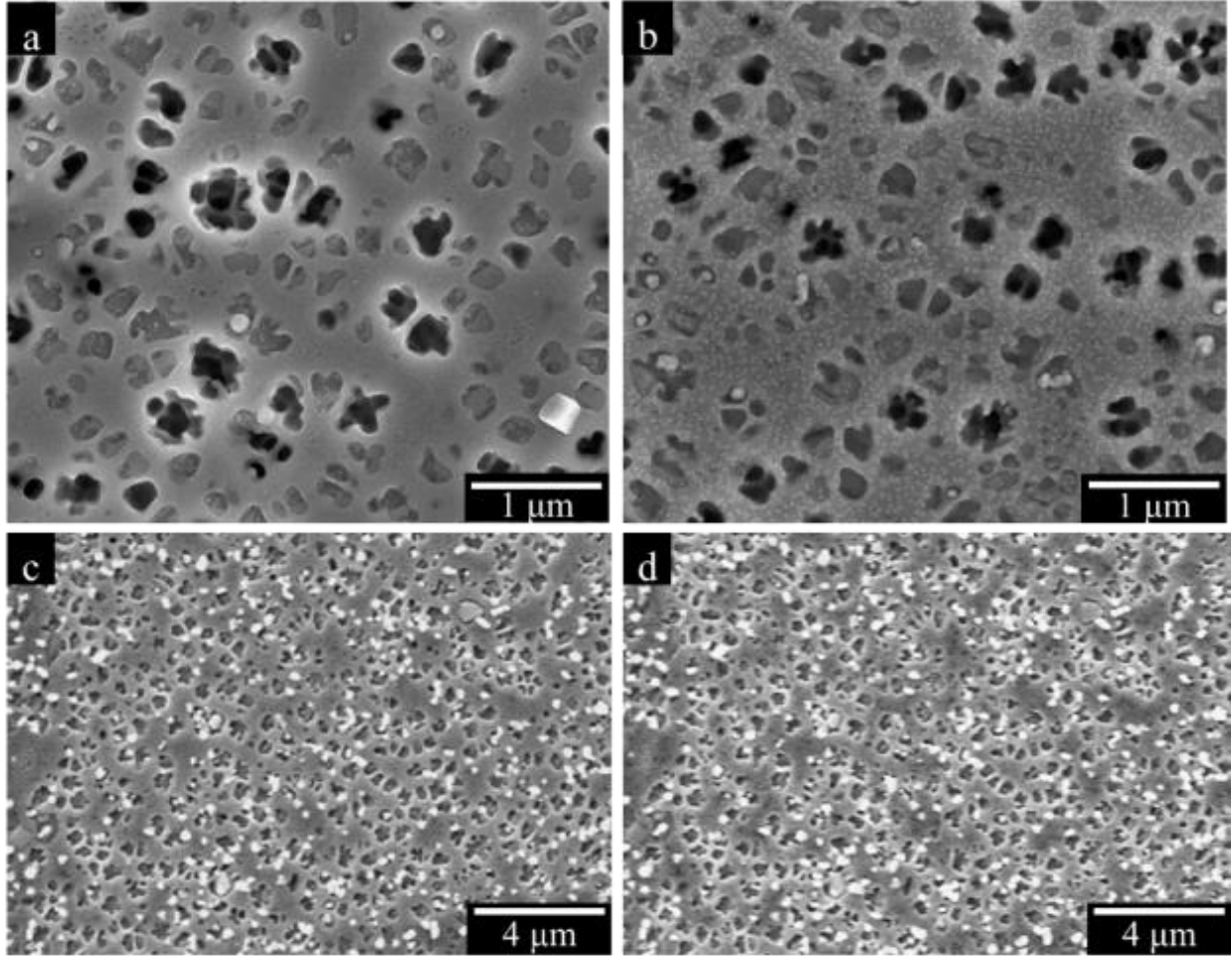
Figure 3.1: Microstructures of condition 1, C1, and condition 2, C2, are shown in (a) and (b), respectively. C1 displays larger secondary γ' with trace presence of the tertiary γ'. C2 displays secondary γ', as well as a dispersed and fine tertiary γ' structure. The gold nano-particle speckle pattern, as adhered to the reference microstructure and following 10 cycles of deformation are shown in (c) and (d), respectively.

The forged pancakes from both conditions were cross-sectioned and examined through the thickness to characterize the gradient of microstructural characteristics, such as grain size and twin boundary fraction. Micro-tensile dog bone specimens were extracted from the forging using electro discharge machining and were at least 1 mm from the forged surface to obtain a uniform microstructure [65]. The specimens had gauge sections measuring 10 mm by 3 mm with a thickness of 1.25 mm. Each specimen was ground with successively finer sandpaper grades. Final mechanical polishing was performed using 0.3 μm and 0.05 μm alumina and silica colloids for 40 minutes and 25 minutes, respectively. Fiducial markers were then placed within the gauge section to outline the area of interest (AOI) to be investigated via electron backscatter diffraction (EBSD) and to provide reference points to consolidate the measured strain data from DIC with the spatial locations of the GBs and crystal orientations. EBSD was performed utilizing a step size of 1.25 μm.

Tailoring GB morphology

The material system studied in this experiment was RR1000, a γ' strengthened, powder processed, Ni-based superalloy with an average grain size of 30 μm [96] following an initial supersolvus heat treatment as detailed by Parr et al.[97] Micro-tensile, dog bone specimens were machined with rectangular gauge dimensions of 10 mm by 3 mm by 1.5 mm thick. A solution heat treatment performed on individual specimen at 1130 °C for 2 hours, followed by controlled cooling at rates of 14 $\frac{°C}{s}$ or 0.7 $\frac{°C}{s}$, tailored the HAGB morphologies, producing planar or serrated GBs, as shown in Fig. 2(a,b), respectively. The heat treatment was performed below the solvus temperature to limit grain growth within the material. Afterwards, the material variants did not experience any further aging process to modify the γ' precipitates. A HAGB is defined between two adjacent grains having a misorientation value of ≥15°, relative to one another. Skeletonized representations of thirty HAGBs were extracted from each variant using a MATLAB plug-in code, grabit.m,[98] in order to characterize the average amplitude and wavelength. A MATLAB algorithm, developed in-house, analyzed each skeletonized GB. A second order polynomial fit established a reference line between triple points. A fast Fourier transform graphed the frequency spectrum of each skeletonized GB, the largest amplitude was identified as the amplitude for each GB. A peak-to-peak measurement of each perturbation along a GB was used to determine the wavelength. A

description of the material pedigree and resulting microstructural characteristics, including GB amplitude and wavelength are shown in Table 3.4.

Table 3.4 summarizes the heat treatment and characterized microstructural attributes in the planar and serrated RR1000 variants.

Microstructure	Annealing conditions	Cooling rate	Grain size	Twin boundary length fraction	High angle GB	
					Amplitude	Wavelength
Planar	1130 °C for 2 hours	$14\,\dfrac{°C}{s}$	49 µm	0.42	0.08 µm	11.4 µm
Serrated		$0.72\,\dfrac{°C}{s}$	60 µm	0.43	0.79 µm	1.58 µm

3.3   Electron microscopy and characterization

3.3.1   Secondary electron imaging

Secondary election imaging was primary utilized for high resolution DIC measurements. The procedures will be covered in a following Section titled "Digital image correlation".

3.3.2   Backscatter electron imaging for γ′ precipitate characterization

Backscatter electron (BSE) imaging was utilized to characterize secondary phases such as γ′ within Ni-based superalloy. First, metallographic specimens were prepared utilizing the standard mechanical grinding steps. The final polishing was achieved utilizing a two-step process, 0.04 µm colloidal silica for 15 minutes followed by electro-chemical etching in 10% phosphoric acid at 2-2.5 V. This procedure dissolves the γ matrix to reveal the γ′ precipitates. The characterization of the γ′ precipitates were conducted on a Zeiss Sigma FEG-SEM utilizing a through-the-lens backscatter electron detector, at 10 keV with a 3-4 mm working distances. The use of back-scatter electron imaging maximizes the contrast variation between the two phases and allowed for automated image thresholding methods to be more readily used to improve accuracy.

The equivalent circular diameter and aspect ratio of the γ′ precipitates were characterized for each variant microstructure through an automated segmentation of SEM micrographs using open source software ImageJ [99]. The precipitate segmentation process consisted of four steps. First the precipitates are separated from the matrix via an automated grayscale threshold. Next, the image is binarized resulting in precipitates displayed as black and the matrix displayed as white. Any holes created within the segmented precipitates from thresholding are then filled to allow for more accurate particle area calculation. It should be noted that particle splitting processes were not used in the current investigation due to the likelihood of erroneous separation and inaccurate precipitate area of the non-spherical morphologies. Lastly, the analyze particle function within ImageJ was used to generate values for area, from which equivalent circle diameter was calculated, and aspect ratio from a minimum of three images acquired from three independent locations in each sample.[99]. A lower bound in the equivalent circular diameter was set at 30 nm, due to the limitations in reliable particle segmentation.

Lastly, back scatter imaging was also utilized to examine GB amplitudes and wavelengths. This GB measurement procedure is described in Chapter 6. Note, the visibility of a GB utilizing this technique is highly dependent on two factors, (i) misorientation between neighboring grains, where grains of similar orientation will not display good contrast and (ii) current of electron beam used for analysis. For best contrast, utilize a high current (Amps) setting on the SEM. This was best achieved by utilizing a large aperture setting on the SEM of 100 µm or 1000 µm.

3.3.3   Electron backscatter diffraction

Electron backscatter diffraction was utilized to gather spatial crystal orientation data within an AOI. Fiducial markers measuring 10 µm across were placed at the corners of the AOI. The reasons for the use of fiducial markers are two-fold; (i) they specify an AOI measuring 300 µm by 200 µm within the center of the gauge section of each specimen and (ii) they provide reference points to spatially consolidate strain data from DIC with the spatial locations of the GBs as collected via EBSD. The characterized surface of each specimen was ground using successively finer sandpaper steps, to a final grit of 1200P. Mechanical polishing was then performed using 0.3 µm and 0.05 µm alumina colloids for 20 minutes and 25 minutes, respectively. The final polish was achieved using a 0.05 µm silica colloid for 5 minutes. EBSD was performed within a Phillips XL-40 at a magnification of 650x with a step size of 1 µm.

3.4   Digital image correlation

Digital image correlation has been a rapidly evolving technique that allows for non-contact strain measurements based on a reference state. The technique calculates the relative displacement fields between a reference and deformed image. These displacement fields are measured by tracking a small subset of pixels within each image and then measuring feature displacements relative to the reference image after a deformation process [12]. Higher resolution is obtained with this measurement technique by tracking a set of features on the specimen with a pattern that is fine, dense, and random. Historically many different methods exist for applying a random speckle pattern at various length scales for DIC strain measurements and have been summarized by Dong and Pan [100]. By coupling the DIC technique with spatial information regarding the microstructural features, researchers have revealed the in-plane strain partitioning around GBs in Ni-based superalloys [14], constituent particles in Al alloys [101], and along slip bands [102]. Additionally Mello et al. [92] quantified a meso-scale cubic slip mechanism in a Ni-based superalloy, which is dependent on temperature as well as the amount of applied strain.

The theory of how digital correlation works is detailed by Peters et al. here[12,103,104]. The resolution of the comparison is determined by the features of which it is tracking. For example, if a 1 and 10 micron pattern are applied to separate specimens and then subsequently deformed, the 1 micron pattern will produce a resolution wherein slip traces are visible, whereby contrast the 10 micron pattern may only illuminate general locations of plastic strain accumulation. Early work was summarized by Rosenfeld between 1955-1979 [105]. Early stages of DIC were done by quantizing data into discrete number sets on punch cards or tape. Advances in technology led eventually to more direct means of comparison such as the one proposed in 1982 by Peters and Ranson. Their method, pictured in Figure 3.2, brought all the modern technology of the day together in a single configuration. The camera read-in the speckle intensity of the light from the surface, the data was then digitized and both stored and displayed[103]. Patterns have evolved greatly from early patterns being as simple as white paint or black ink to more complex methods such as electron beam lithography, gold nanoparticles or vapor deposition[106]. It is noteworthy to mention that this technique is fully scalable, meaning it could be used on something as large as a bridge and as small as a grain, all depending on the pattern or points being tracked. That being said when dealing with a capture method such as an optical microscope where all the pixels of a given image are captured at the same time there is no time dependency between points so that picture is directly

comparable to another image taken on that same microscope. However, if taking images on an electron microscope care must be taken in interpreting the results. Sutton et al. [107,108]discuss and examine the variations that come from combining electron microscopy, and DIC. These distortions manifest themselves as both temporal and spatial. Since electron microscopy uses a rastering method to capture images there can exist a drift from when the image capture begins to when it finishes. Since DIC compares positions of pixels to their neighbors a drift of one or two pixels when measuring intragranular strain could cause a large fictitious strain. The second distortion comes from the lens curvature and can be account for by understanding how your specific lens affects the image.

To compensate for these distortions, Kammers and Daly [109–111] utilized a compensation method which involves taking images at different known locations over a known time and averaging them to correct for both spatial and temporal distortion. Drift distortions are also discussed, this results in smaller distortions at the top of an image and larger distortions at the base[109]. An image correction procedure for ex-situ loading has been developed by Mello et al. [112]. First, the signal to noise ratio of the micrograph is maximized and drift minimized by selecting the optimal combination of SEM conditions, accelerating voltage and spot size. The drift of each set of microscope conditions can be checked utilizing VIC2D and two images taken one after the other of the same location. Second, a certified grid with known dimensions is imaged during each SEM session, this allow for the magnification error, hysteresis effect, drift distortions to be corrected, based on a reference measurement. A full description of this correction protocol is available within Mello et al. [112]. The aforementioned correction protocol was utilized on all electron micrographs used in DIC measurements.
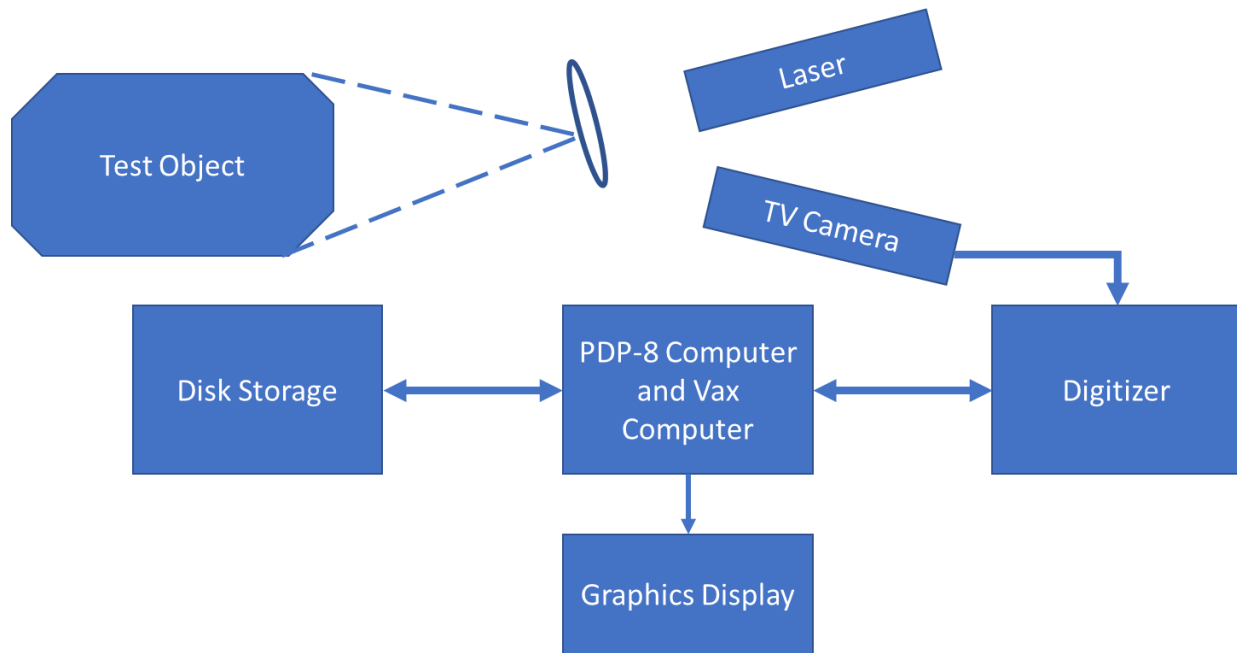
Figure 3.2: The setup used by Peters and Ranson in source, recreated from [103].

3.4.1 Specimen preparation for digital image correlation analysis

Following EBSD characterization, the specimen surface was now ready for the application of a speckle pattern. The size and density of the speckle pattern can be tailored to accommodate both optical (lower resolution) and SEM (higher resolution) analysis. Optical DIC was utilized to capture the average deformation within a grain. For more detail, SEM analysis was utilized wherein individual slip bands could be distinguished. Correlations were carried out using commercial software VIC-2D^{TM} Version 6.

Optical imaging for deformation band identification

For DB characterization in Chapter 4, titanium nanoparticles, with a mean size of 80 nm, were applied to each specimen. The nano-particle solution was prepared and applied in accordance with Tracy et al. [113]. A Zeiss Axio Imager with a total magnification of 50x was utilized to capture images at a resolution of 1960 x 1460 pixels or $0.9 \frac{\mu m}{pixel}$. In total, four images with 15% overlap were needed to capture each AOI. Note: greater magnification does not equal better resolution DIC analysis. Greater magnification and a larger numerical aperture rating for the final lens translate

into DIC datasets with greater resolution. The dimensions of each AOI were 2 mm x 2 mm. A subset of 28 µm and a step size of 1.8 µm were utilized to perform the correlations.

Scanning electron microscopy for intergranular slip band identification

Gold nano-particles, with an average size of 0.03 μm, were applied to each specimen to provide a random surface pattern that could be used for DIC analysis and provide slip band level resolution for the strain measurements. No degradation of the gold nano-particle pattern was observed during cyclic deformation, as shown in Figure 3.1 (c) and (d). Further details on the application technique of the gold nano-particles are discussed by Kammers and Daly [109]. Images for DIC were captured using a Phillips XL-40 FEG SEM, with image resolution of 3872 x 2904 pixels and working distance of 10 mm. The spatial resolution of each image is $0.0327 \frac{\mu m}{pixel}$. An area of 200 μm x 200 μm was imaged and consisted of 6 stitched images, two images wide by three images long. Each image was correlated using a subset of 1.34 μm x 1.34 μm and a step size of 0.06 μm. Each image was corrected for spatial and drift distortions that are inherent to electron microscopy as described by Sutton et al. [114]. These distortions were removed by following a procedure developed by Mello et al. [112]. This method uses a certified grid with known feature locations and dimensions. The certified grid served as a reference image for each microscopy session and ensures a constant magnification between sessions; the full procedure is discussed in detail in the following reference [112].

4. BRIDGING MACROSCOPIC AND MICROSCOPIC MECHANICAL RESPONSE VIA DEFORMATION BAND FEATURES

The content in this chapter has been published and is available at the following citation: John Rotella, Adam L. Pilchak and Michael D. Sangid, Examining the pathways for deformation band formation at the mesoscale, Materials Characterization 182 (2021) 111552. DOI 10.1016/j.matchar.2021.111552. [115]

4.1 Introduction

The development of the deformation pathways within polycrystalline materials is a multi-scale process, wherein the macroscopic loading conditions and local microstructure dictate the mechanical response [1,20]. The specific features addressed in this section of the thesis are, the grain size, crystallographic orientation, and GBs. Chapter 4 aims to reveal the impact of strain magnitude, grain size, crystallographic orientation, and GBs on the development of the macroscopic strain pathways. Four separate stress states, torsion, tension, 2:1 tension and 2:1 torsion, were characterized via DIC and EBSD. The orientation of the DBs were characterized via two-point statistics and compared against the plane of MSS. The trends reported here are consistent for each of the global stress states. Finally, the characterized deformation pathway measurements, macroscopic residual strain, $E_{Total}^{residual}$, and micromechanical fields are utilized to inform a RVE size, which are compared against prior RVE instantiations on similar and engineering variations of the material.

4.2 Materials and Methods

4.2.1 Specimen preparation

The material system studied in this experiment was a near alpha phase titanium alloy, Ti7Al, with a hexagonal closed packed crystal structure. The Ti7Al material was cast into ingot form, hot isostatic pressed, extruded and annealed at 955 °C for 24 hours, followed by an air cool [93]. The resulting material contained equiaxed grains with an average grain size of 86 µm. Gauge sections of Ti7Al were extracted and friction stir welded to circular gripping end pieces of Ti-6V-4Al. A 10 mm, square-cross section, gauge length was machined from the Ti7Al portion to complete the

specimen geometry, as shown in Figure 4.1a. Each specimen was machined and electro-polished to create a mirror finish, enabling spatial orientation characterization via EBSD.

An AOI measuring 2150 μm by 2250 μm was marked within the gauge section using Vickers indents as fiducial markers, which were placed using a LECO Microhardness Tester, model LM247AT. The fiducial marker pattern is shown in Figure 4.1b. The fiducial markers served a two-fold purpose; (i) establish an AOI and (ii) provide spatial reference markings to consolidate the DIC and EBSD datasets. Crystallographic orientation data was collected via EBSD utilizing an Oxford symmetry detector, with a step size of 2 µm. The GBs were defined by a 5° misorientation tolerance. The normal-direction inverse pole figure maps for each specimen are shown in Figure 4.2.
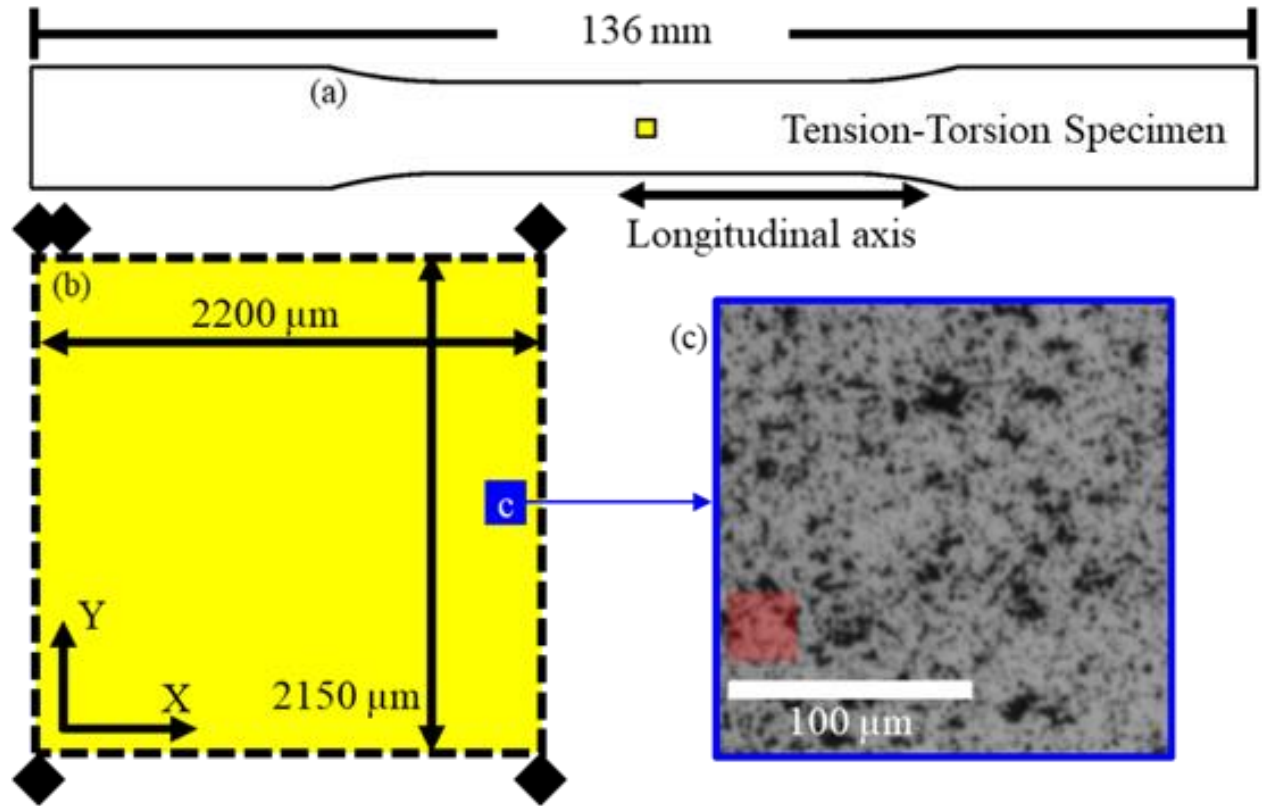
Figure 4.1: (a) A scale representation of the tension-torsion specimen displaying the position and size of the AOI. (b) The dimensions of the AOI for each specimen, with specified subregion of interest. (c) Subregion of interest, displaying titanium nanoparticle speckle pattern. The translucent red box represents the subset size utilized for the DIC analysis, 28 µm.
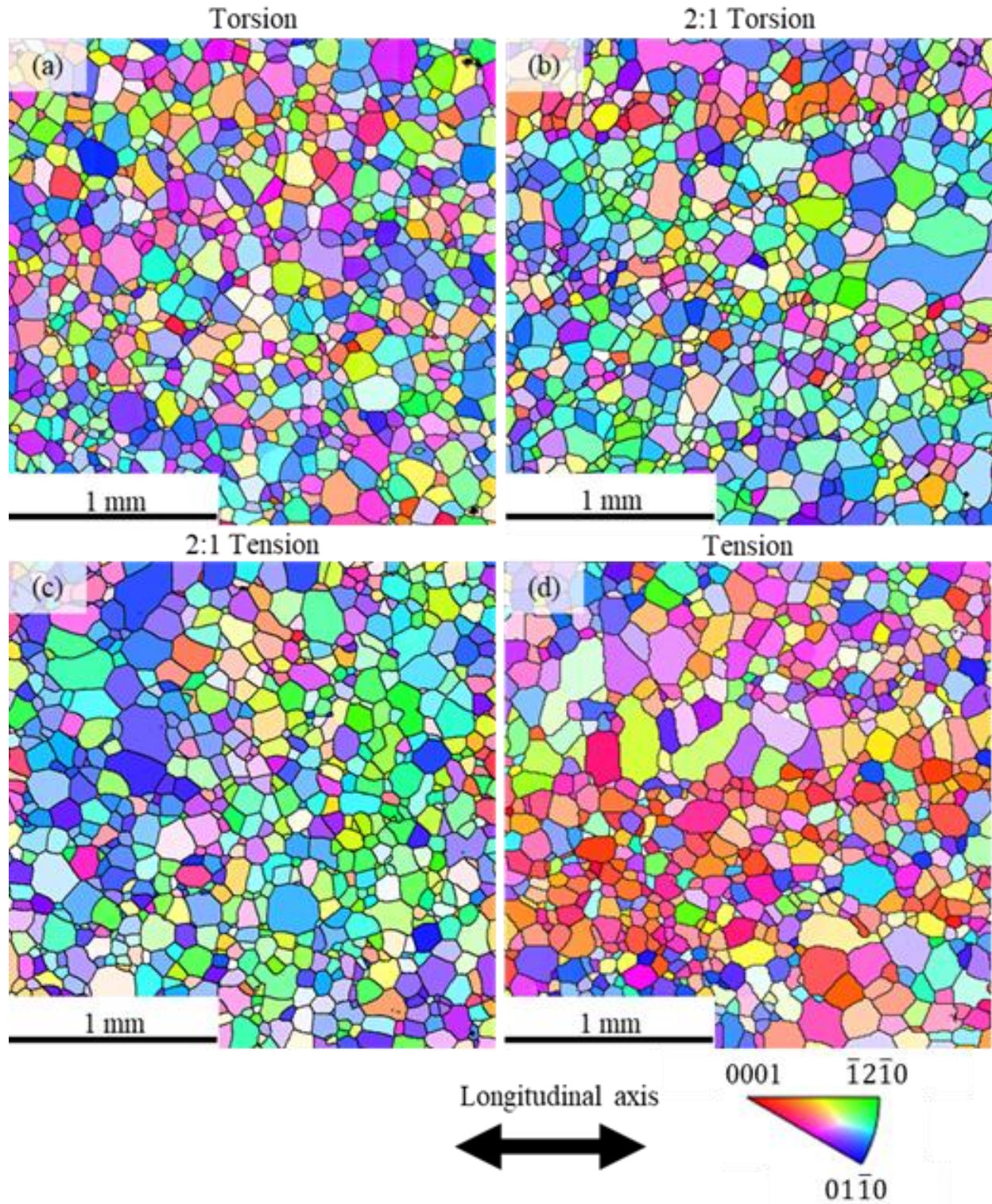
Figure 4.2: The normal-direction inverse pole figure representations for each of the analyzed AOIs are shown for the macroscopic loading states; (a) torsion, (b) 2:1 torsion, (c) 2:1 tension and (d) tension specimens. The longitudinal axis is denoted for all specimens.

4.2.2 Experimental details

Four tension-torsion experiments were conducted in an MTS Model 809 servo hydraulic test system with a MTS biaxial extensometer, model 632, to monitor the applied tensile and shear strains. Each specimen was loaded in stress control to the same target least squares strain, E_{Total}, of 0.6% as defined by Eq. 3.1. The E_{Total}, 0.006, value was chosen such that the applied load would be just beyond the yield stress of the material. The choice in the E_{Total} ensured sufficient deformation was imparted to make DB identification possible and avoided difficulties that may have resulted by large deformations, such as uniquely distinguishing DBs or damage to the DIC speckle pattern. Specimens were returned to 0% shear strain, to ensure a near planar surface for the DIC technique, and zero tensile load, before being removed from the load frame. Therefore, the residual macroscopic strain, $E_{Total}^{residual}$ for each specimen is different, where the $E_{Total}^{residual}$ is proportional to the applied shear strain. Tension-torsion experiments of varying ratios were conducted on 4 specimens, the specific experimental conditions were torsion, tension, 2:1 tension and 2:1 torsion. Where the ratio 2:1, indicates the fraction of the applied strains. The applied strain conditions and residual strain for each specimen are shown in Table 4.1 within columns 1, 2 and 3.

Table 4.1: The peak tensile strain ($E_{Applied}^{Tension}$) and shear strain ($\Gamma_{Applied}^{Shear}$) applied macroscopically to each specimen. The residual macroscopic strain of each specimen, $E_{Total}^{residual}$. The average maximum in-plane shear strain within each specimen's AOI, $\overline{\gamma}^{max}$.

	$E_{Applied}^{Tension}$	$\Gamma_{Applied}^{Shear}$	$E_{Total}^{residual}$	$\overline{\gamma}^{max}$
Torsion	0 %	0.60 %	0.20 %	0.26 %
2:1 Torsion	0.27 %	0.54 %	0.078 %	0.34 %
2:1 Tension	0.54 %	0.27 %	0.075 %	0.36 %
Tension	0.60 %	0 %	0.051 %	0.58 %

The tensile strain rate ($\dot{\varepsilon}_{Tensile}$), shear strain rate ($\dot{\varepsilon}_{Shear}$) and combined strain rate ($\dot{\varepsilon}_{Combined}$) for each specimen were on the order of 1E^{-5} s^{-1} and are listed within Table 4.2 for each loading

condition. The combined strain rate was determined by substituting strain rate for strain within Eq. 3.1.

Table 4.2: The tensile ($\dot{\varepsilon}_{Tensile}$), shear ($\dot{\varepsilon}_{Shear}$), and combined ($\dot{\varepsilon}_{Combined}$) strain rates ($s^{-1}$) for each loading condition.

Loading Condition	$\dot{\varepsilon}_{Tensile}$ (s^{-1})	$\dot{\varepsilon}_{Shear}$ (s^{-1})	$\dot{\varepsilon}_{Combined}$ (s^{-1})
Torsion	-	6.80E-05	6.80E-05
2:1 Tension	3.40E-05	1.75E-05	3.81E-05
2:1Torsion	1.67E-05	3.17E-05	3.58E-05
Tension	3.35E-05	-	3.35E-05

Full field deformation was captured utilizing the DIC technique and overlaid with the microstructure as captured via EBSD. DIC was performed with the Correlated Solutions VIC2D software package utilizing a subset of 28 µm and a step size of 1.8 µm, as shown in Figure 4.1c. To account for all in-plane strains captured within the dataset, the maximum in-plane shear strain, γ^{max}, was calculated for each spatial point utilizing Eq. 4.1 [116], wherein ε_{xx}, ε_{yy}, and ε_{xy} are the axial, transverse, and in-plane shear strains at each pixel location, respectively.

$$\gamma^{max} = \sqrt{\left(\frac{\varepsilon_{xx} - \varepsilon_{yy}}{2}\right)^2 + \left(\frac{\varepsilon_{xy}}{2}\right)^2}$$

Eq. 4.1

The resulting γ^{max} maps for each specimen are shown in Figure 4.3. Regions of localized plastic strain present as discrete bands within the microstructure and are observed to form at varying angles based on the imposed stress state. The plane of MSS for each loading case is superimposed. The average maximum in-plane shear strain, $\bar{\gamma}^{max}$, for each specimen's AOI is shown in column 4 of Table 4.1.
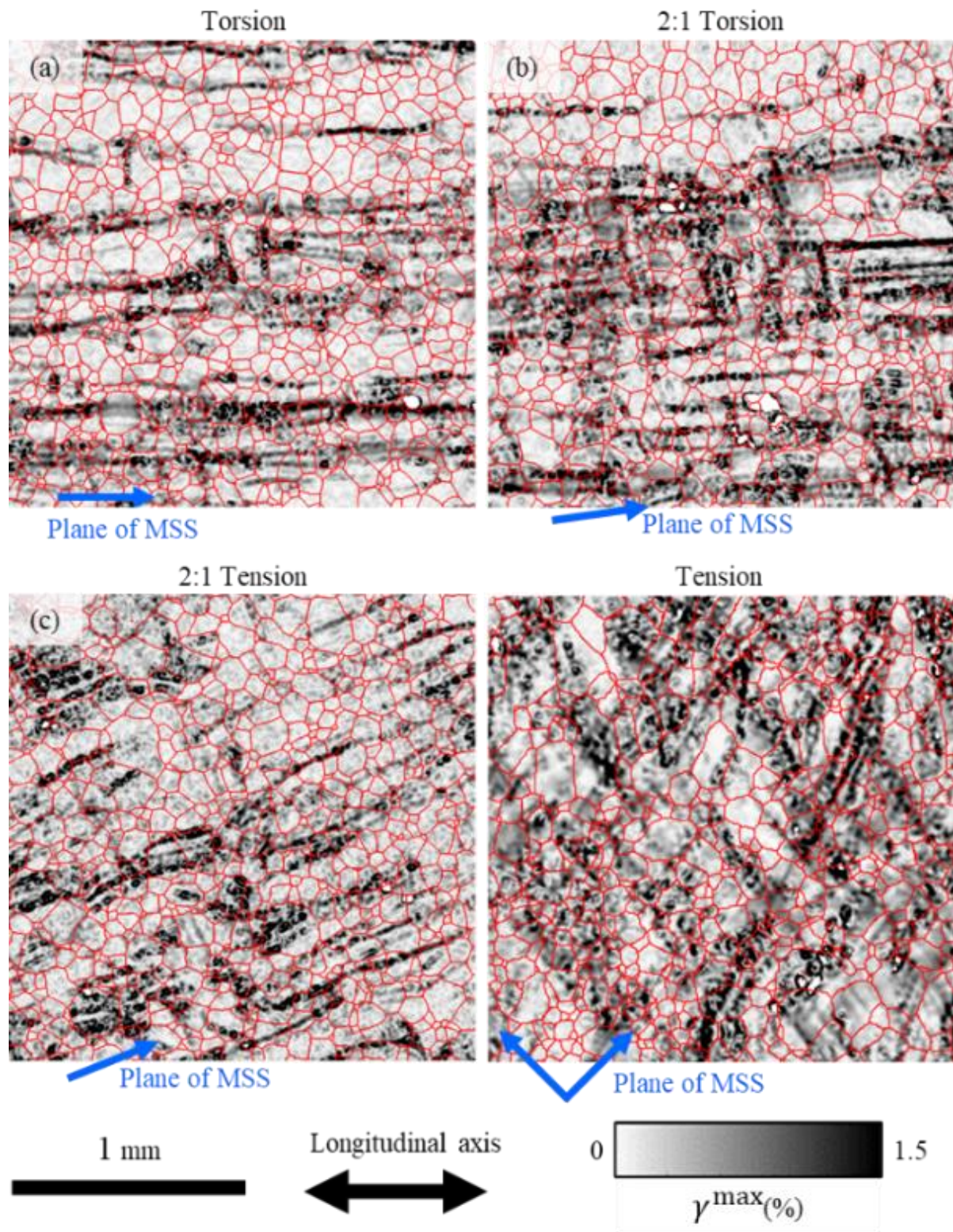
Figure 4.3: Strain maps displaying the γ^{max}, for the (a) torsion, (b) 2:1 torsion, (c) 2:1 tension and (d) tension specimens. The plane of MSS is delineated by an arrow for each specimen.

4.2.3   Deformation band identification and orientation analysis

DBs were identified by utilizing a series of applied strain thresholds and applying percolation theory as series of a fill-flood actions. By utilizing this method of segmentation, a DB can be described as the inter-connectivity of the plastic deformation resulting from the imposed macroscopic deformation [117]. The results of this analysis will be referred to as the percolation strain throughout the article. First a strain threshold and MATLAB based percolation algorithm [118] are applied to the original γ^{max} maps, as shown in Figure 4.4a. The percolation algorithm utilized strain thresholds as high pass filters and subsequently fill-flood commands to identify and cluster 8-connected pixels [118] with γ^{max} magnitudes above 0.3%, 0.6% and 0.9%. Each cluster is defined as a DB and is shown as a unique color for the torsion specimen in Figure 4.4b. Each DB was skeletonized, allowing for each spatial point within the DB to be referenced to other microstructural features such as GBs, as shown in Figure 4.4c.

An autocorrelation [119,120] was utilized to establish the mean orientation of the DBs within each specimen. The autocorrelation utilized binarized data, where the DBs are represented by white and the surrounding matrix is black, as shown in Figure 4.5a. The autocorrelation produced a spatial probability map which corresponds to the likelihood of the DBs overlapping one another, as shown for the torsion specimen in Figure 4.5b. Iso-probabilities were represented by ellipses fit to the autocorrelation probability map as shown schematically in Figure 4.5c, wherein the greatest and lowest iso-probability contour correspond to P1 and P3, respectively. The mean orientation of DBs or inclination angle within each specimen was defined as the angle between the major axis of the fit ellipse and the longitudinal axis. The range of iso-probability values were consistent for each percolation strain and were selected via inspection to allow ellipse fitting over the largest range of probability values.
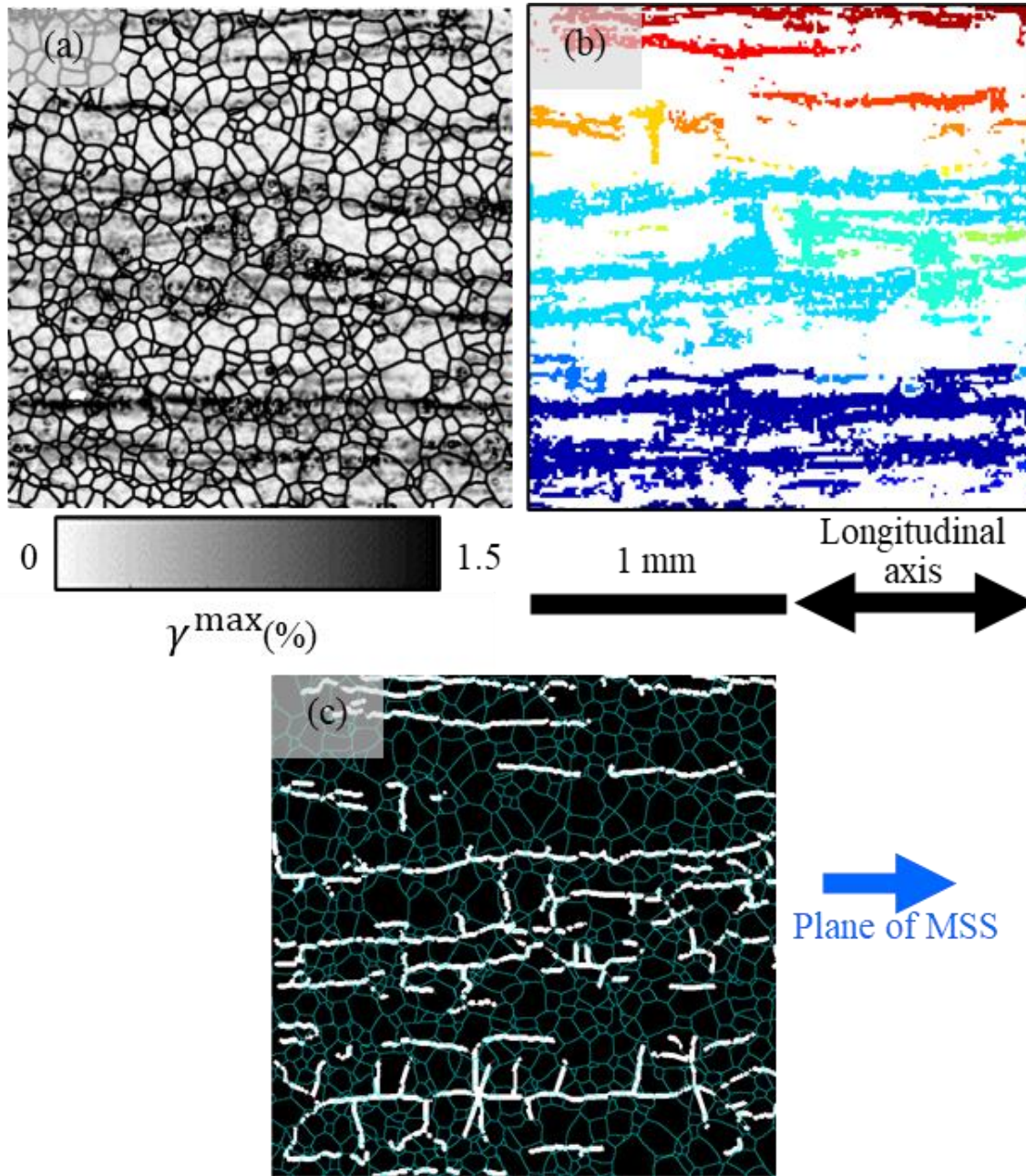
Figure 4.4: (a) Strain map displaying the γ^{max} of the torsion specimen. (b) DBs are identified by unique colors following the percolation strain at 0.3%. (c) A skeletonized representation of each DB represented in (b). GBs are represented by black and teal lines in (a) and (c), respectively. The longitudinal axis and plane of MSS are delineated by arrows.
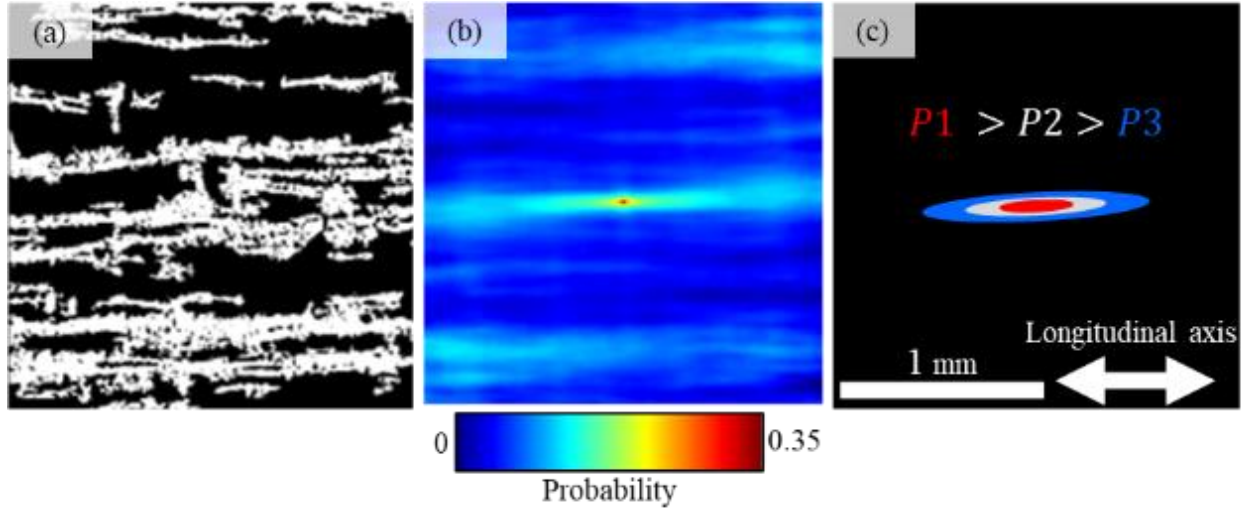
Figure 4.5: (a) Binary DB map for the torsion specimen. (b) Self-correlation of image (a). (c) Iso-probability contours as traced by ellipsoid fitting, wherein each ellipse represents a different probability contour. Note that a larger probability value such as P1 corresponds to a fit ellipse with smaller area.

4.2.4 RVE construction via a combination of the macroscopic and micromechanical deformation response

The following procedure establishes a mesoscale RVE edge length that satisfies the macroscopic and micromechanical strain state of the material. The following methodology has been modified to utilize plastic strain data from the original methodology presented by Balzani et al. [89], who utilized stresses obtained through finite element simulations. The procedure first establishes an area which minimizes the error between the $E_{Total}^{residual}$ and the $\bar{\gamma}^{max}$ of potential RVE window, which varies in size. The edge length of the window with be referred to as the RVE edge length. The micromechanical analysis informs the number of DBs features which will fit within the established mesoscale RVE by matching feature statistics throughout the AOI. The RVE model established by these methods will be referred to as the mesoscale plastic strain sizing (MPSS) model.

Macroscopic RVE sizing approach

The macroscopic approach utilizes a minimization of a least squares functional to determine the RVE edge length which minimizes the overall deformation response error, relative to the $E_{Total}^{residual}$. First, the reasonable deviation, r, is computed for each specimen and for each RVE

47

edge length that fits within the AOI. The value r is derived by normalizing the difference between the $E_{Total}^{residual}$ and the average maximum in-plane shear strain within that specific RVE, $\bar{\gamma}_{RVE}^{max}$, as described by Eq. 4.2.

$$r = \frac{E_{Total}^{residual} - \bar{\gamma}_{RVE}^{max}}{E_{Total}^{residual}}$$

Eq. 4.2

The average macroscopic error, $\tilde{r}$, is then computed separately for each specimen utilizing the list of r values for each RVE edge length and is defined as

$$\tilde{r} = \sqrt{\frac{1}{n_{ep}} \sum_{j=1}^{n_{ep}} (r_j^2)}$$

Eq. 4.3

where n_{ep} is the number of RVE edge lengths over which r was calculated. The overall mechanical error, $\tilde{r}_{\emptyset}$, incorporates $\tilde{r}$ of all specimens into a single value per RVE edge length and is defined as

$$\tilde{r}_{\emptyset} = \sqrt{\frac{1}{n_{exp}} \sum_{j=1}^{n_{exp}} \tilde{r}^2}$$

Eq. 4.4

where n_{exp} is the number of experiments (i.e., specimens). The $\tilde{r}_{\emptyset}$ is determined for all RVE edge lengths and decreases exponentially with increasing RVE edge length. Therefore, the RVE edge length which minimizes the $\tilde{r}_{\emptyset}$ over all loading cases can be determined.

Micromechanical RVE sizing approach

The micromechanical methodology quantifies the number of microstructural features that should statistically occur within the RVE previously sized by the macroscopic approach. The DB area fraction, DB_{AF}, was utilized to approximate the micromechanical variability throughout the AOIs and is defined as

$$DB_{AF} = \frac{Pixel_{DB}}{Pixel_{AOI}}$$

Eq. 4.5

where the number of pixels occupied by DBs and the total number of pixels within the AOI are defined as $Pixel_{DB}$ and $Pixel_{AOI}$, respectively. The average DB area fraction, $\overline{DB}_{AF}$, was utilized to compute the number of DBs, n_{DB}, per RVE edge length as shown in Eq. 4.6.

$$RVE \text{ edge length} = \sqrt{\frac{n_{DB}\bar{A}_{DB}}{\overline{DB}_{AF}}}$$

Eq. 4.6

Where the $\bar{A}_{DB}$ is the average area of a DB for each specimen and was calculated by utilizing the mean thickness and mean length of the DBs at each percolation strain. The n_{DB} is the only

unknown and is solved for by utilizing the RVE edge length previously established in the above subsection "Macroscopic RVE sizing approach".

4.3   Results

In principle results of this study are three-fold, (i) the DB descriptors of orientation, length and width are characterized at three percolation strains, (ii) the preference for DB formation and perturbation throughout the microstructure are investigated relative to three percolation strains and microstructural features, and (iii) a mesoscopic RVE size that satisfies both the macroscopic deformation state as well as matches the micromechanical variability along microstructural features is identified utilizing aforementioned methodologies.

4.3.1   The macroscopic orientation and morphology of deformation bands

The degree of strain accumulation within the deformation pathways were examined for each loading case. The plastic strain was binned utilizing percolation strains of 0.3%, 0.6% and 0.9%, as shown for all specimens in Figure 4.6. For each loading configuration, the plane of MSS is superimposed on each γ^{max} map. In general, the greatest strain accumulations occur parallel to the plane of MSS and begin to deviate from the plane of MSS as the percolation strain is decreased. A region in Figure 4.6b has been boxed for subsequent interpretation.
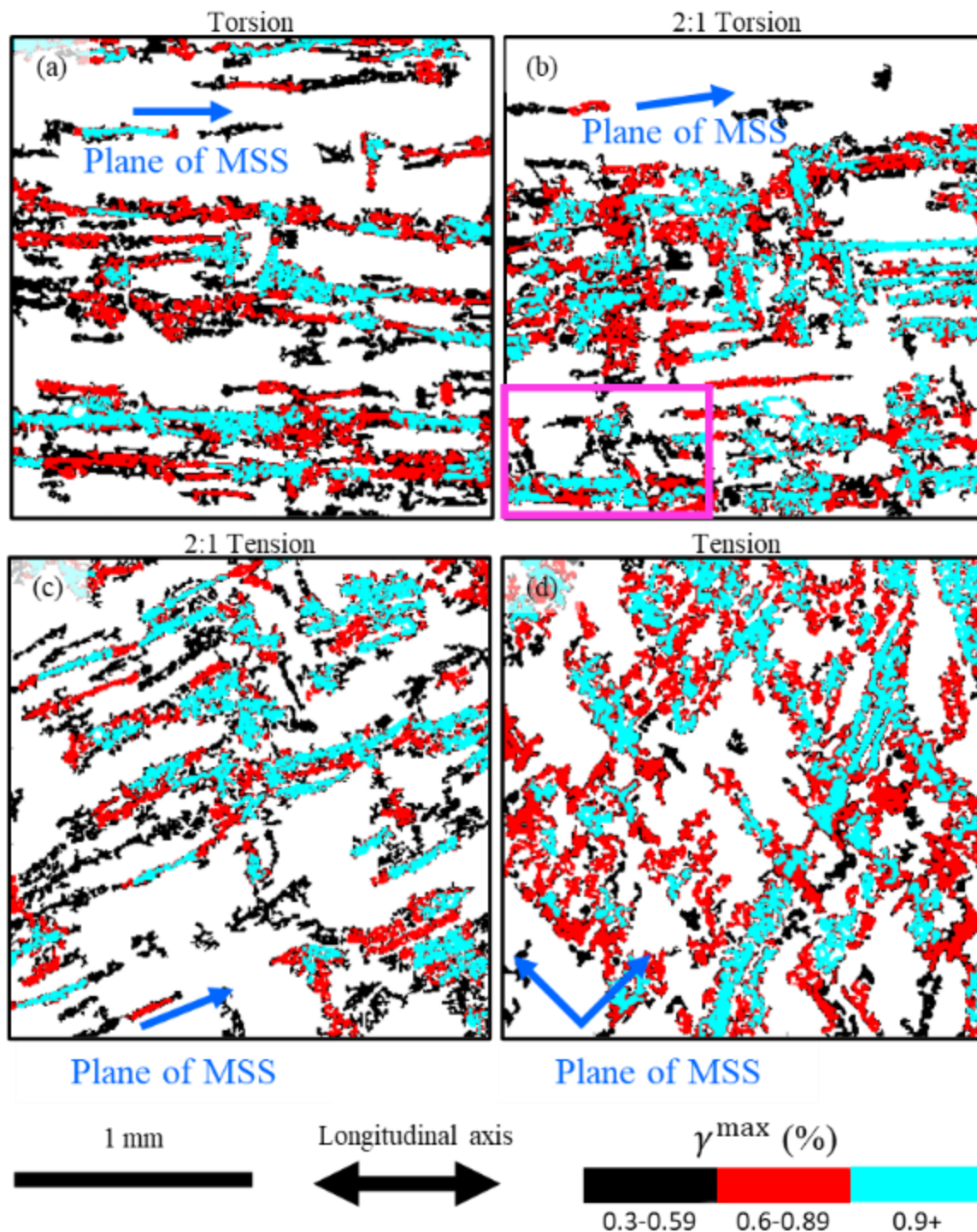
Figure 4.6: DBs are shown at multiple percolation strains, 0.3%, 0.6% and 0.9%, for the loading conditions: (a) torsion, (b) 2:1 torsion, (c) 2:1 tension and (d) tension specimens. The theoretical angle of the deformation, the plane of MSS, is annotated for each loading condition. The box region in (b) will be discussed in Figure 4.8.

The mean orientation of all DBs within each specimen were examined utilizing the autocorrelation method previously described in Section 4.2.3. The range of DB inclination angles and the plane of MSS for each loading case, relative to the longitudinal axis, are shown in Table 4.3. The DB inclination angles from the autocorrelation technique were near the expected deformation angles. DBs were observed to form within 5° of the planes of MSS.

Table 4.3: The range of DB inclination angles from autocorrelation and the angle of the plane of MSS, relative to the longitudinal axis of the specimen.

	Inclination Angle	
	Range from autocorrelation	Plane of MSS
Torsion	0° - 5°	0°
2:1 Torsion	3° - 10°	7.88°
2:1 Tension	19° - 27°	22.5°
Tension	41° - 44°	45°

The length and thickness of each DB was quantified utilizing ImageJ [99] for all percolation strains. The length of a DB was defined as the Euclidean distance from end-to-end. Along each DB, the width was measured approximately every 100 µm. The DB measurements for all percolation strains are shown in Figure 4.7. All presented statistical descriptors of the length and width of the DBs were inversely proportional to the percolation stain. A few DBs spanned the entire AOI, thus the mean lengths may be larger than classified. The maximum width of a DB was approximately 3 grain diameter or 250 µm.
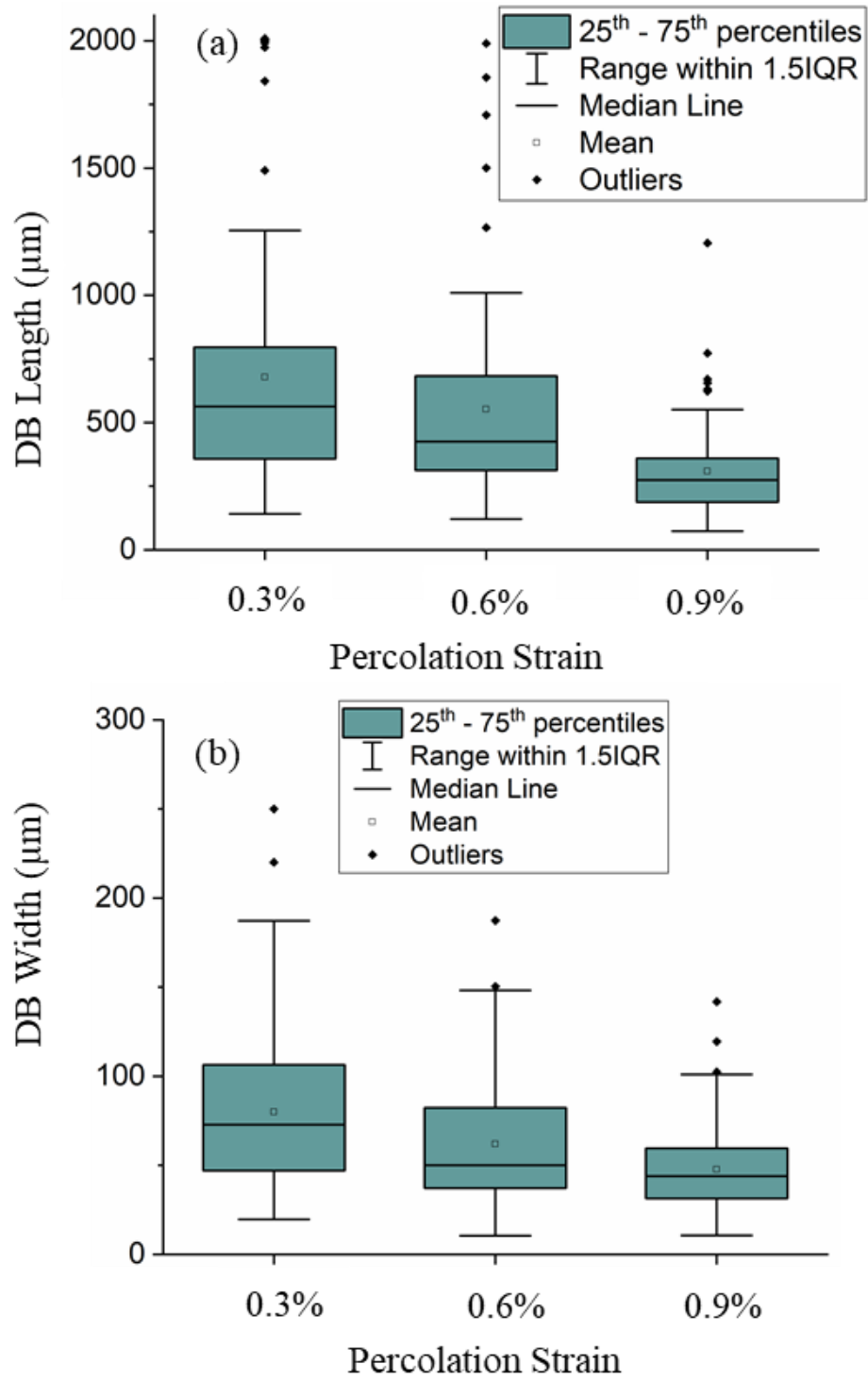
Figure 4.7: Deformation band measurements of the (a) length and (b) thickness at percolation strains 0.3%, 0.6% and 0.9%.

4.3.2 The macroscopic orientation and morphology of deformation bands

The pathways of deformation were examined relative to GBs and based on the degree of accommodated strain. A visual inspection of the DBs relative to GBs, was conducted, a representative region is shown in Figure 4.8. Figure 4.8 was created by superimposing the GBs onto the DBs previously shown in the boxed region of Figure 4.6b. As expected, the plastic deformation accumulated parallel to the plane of MSS. However, several encircled regions show deformation which deviated from the plane of MSS near GBs. These deviations appeared more common at lower percolation strains and are investigated further in the following analysis.

The ability of a GB to influence the pathway of DBs was examined by characterizing the angular deviation of each DB relative to the nearest GB at each percolation strain. First, a skeletonized DB was divided into segments measuring 16 µm in length, as shown in Figure 4.9a. Note, this analysis has been repeated with DB segments ranging between 8 µm and 20 µm in length with no effect on the reported trends. Next, the angle between adjacent DB segments was determined. This quantity is defined as the deformation band deviation (DBD), as shown within Figure 4.9b. Once a DBD was determined for a DB segment, all pixels within that DB segment would be assigned that DBD. The distance between DB segments and the nearest GB was determined by measuring the distance between each DB pixel and every surrounding GB pixel, the minimum distance was identified for each corresponding DB pixel. If the DB was coincident with the GB, the distance reported is zero. For the lowest percolation strain, 0.3%, the DBD spans from $0° – 90°$, as shown in Figure 4.10 (a), (d), (g) and (j). As the percolation strain increases to 0.6% and 0.9% the DBD trends toward $0°$, as shown in Figure 4.10 (b-c), (e-f), (h-i) and (k-l). These results demonstrate that DBs have a greater effect on the pathways of DBs at relatively low strain magnitudes, while DBs with larger degrees of strain are more directly influenced by the plane of MSS. For validity, the method utilized to determine the DB pathways should validate previous literature, wherein GBs are observed to accumulate the largest degree of deformation. The γ^{max} magnitudes were binned by distance to the nearest GB and are shown for each specimen within Figure 4.11. As expected, DB locations near GBs localized the greatest degree of deformation and serve as a confirmation that the method utilized to define DBs is reasonable.
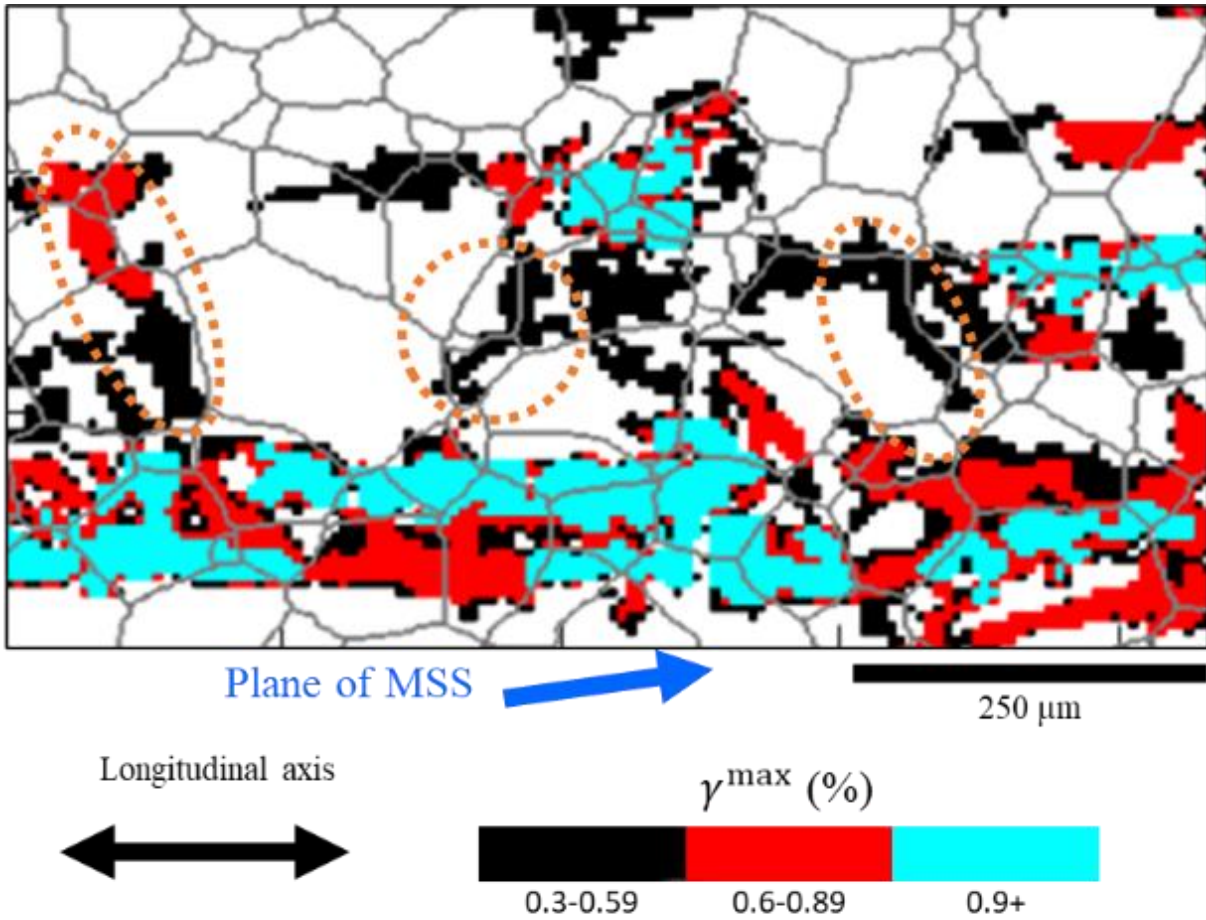
Figure 4.8: DBs with superimposed GBs of a subsection of the 2:1 torsion AOI, at three percolation strains, 0.3%, 0.6% and 0.9%. Specific instances of deformation deviations near GBs at a percolation strain of 0.3% are encircled. DBs with magnitudes of 0.9% or larger are observed to form nearly parallel to the plane of MSS.

(a)

3

2

Line segments
defined between
points 1-2 and 2-3.

1

Deformation band

(b)

DBD

2

3

1
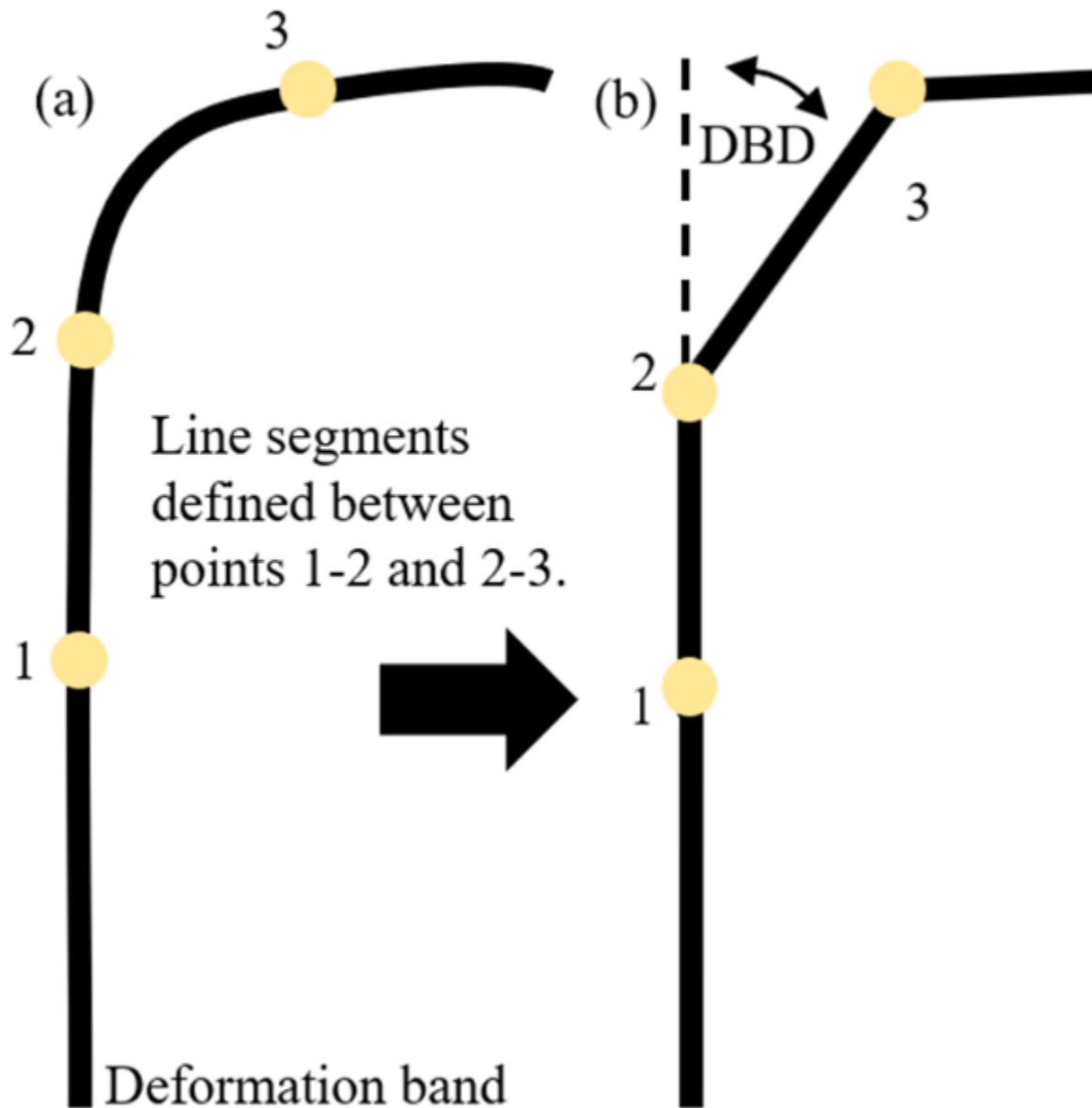
Figure 4.9: A deformation band is shown in segments, where each segment begins or terminates at a circle. (b) The deformation band deflection, DBD, is shown schematically between points 1-2 and points 2-3.
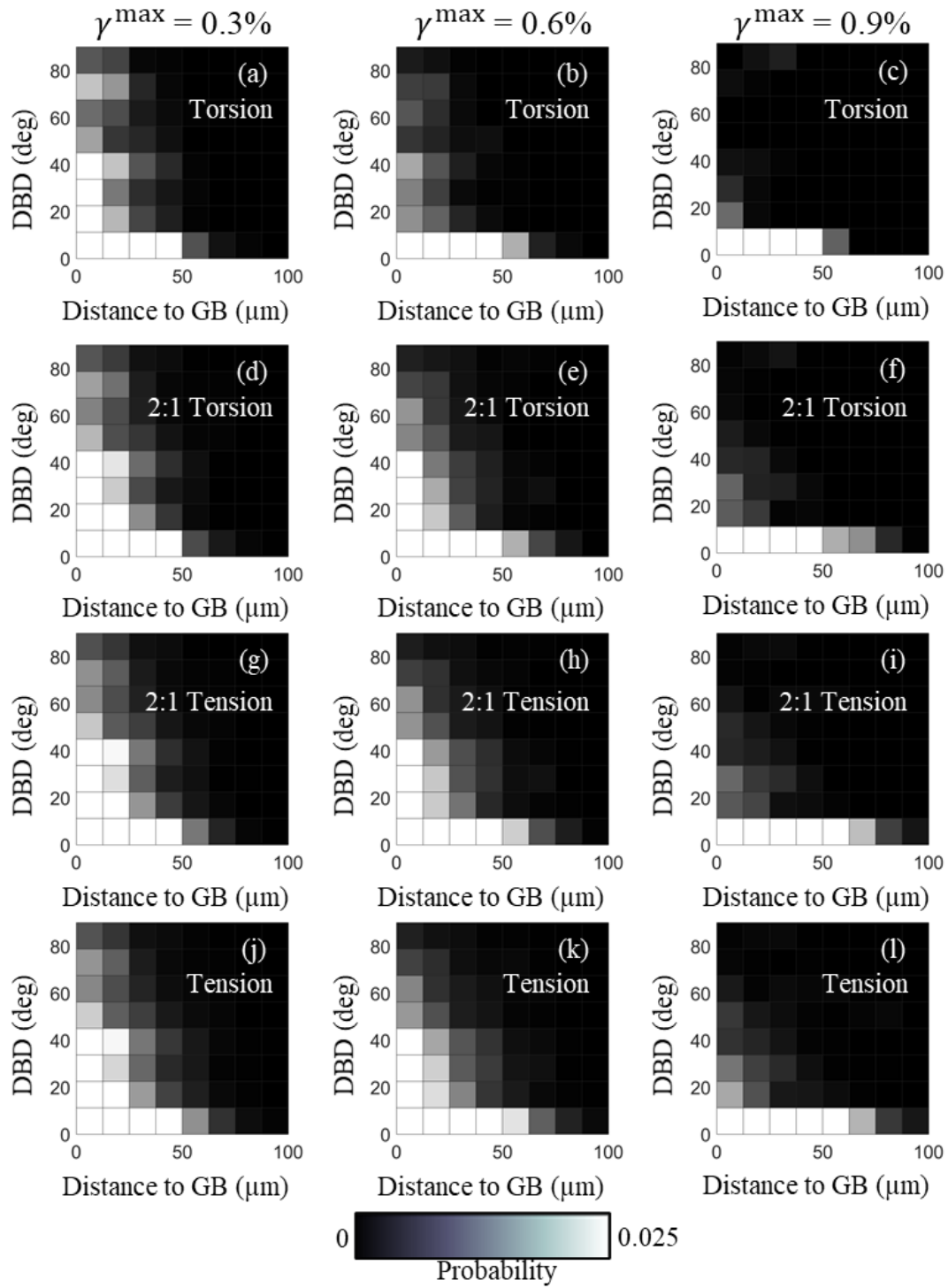
Figure 4.10: The deformation band deviation, DBD, as a function of distance to the nearest GB, and percolation strain values. γ^{max} of 0.3% (left column), 0.6% (center column) and 0.9% (right column) are shown for loading states (a – c) torsion, (d – f) 2:1 torsion, (g – i) 2:1 tension, and (j – l) tension.
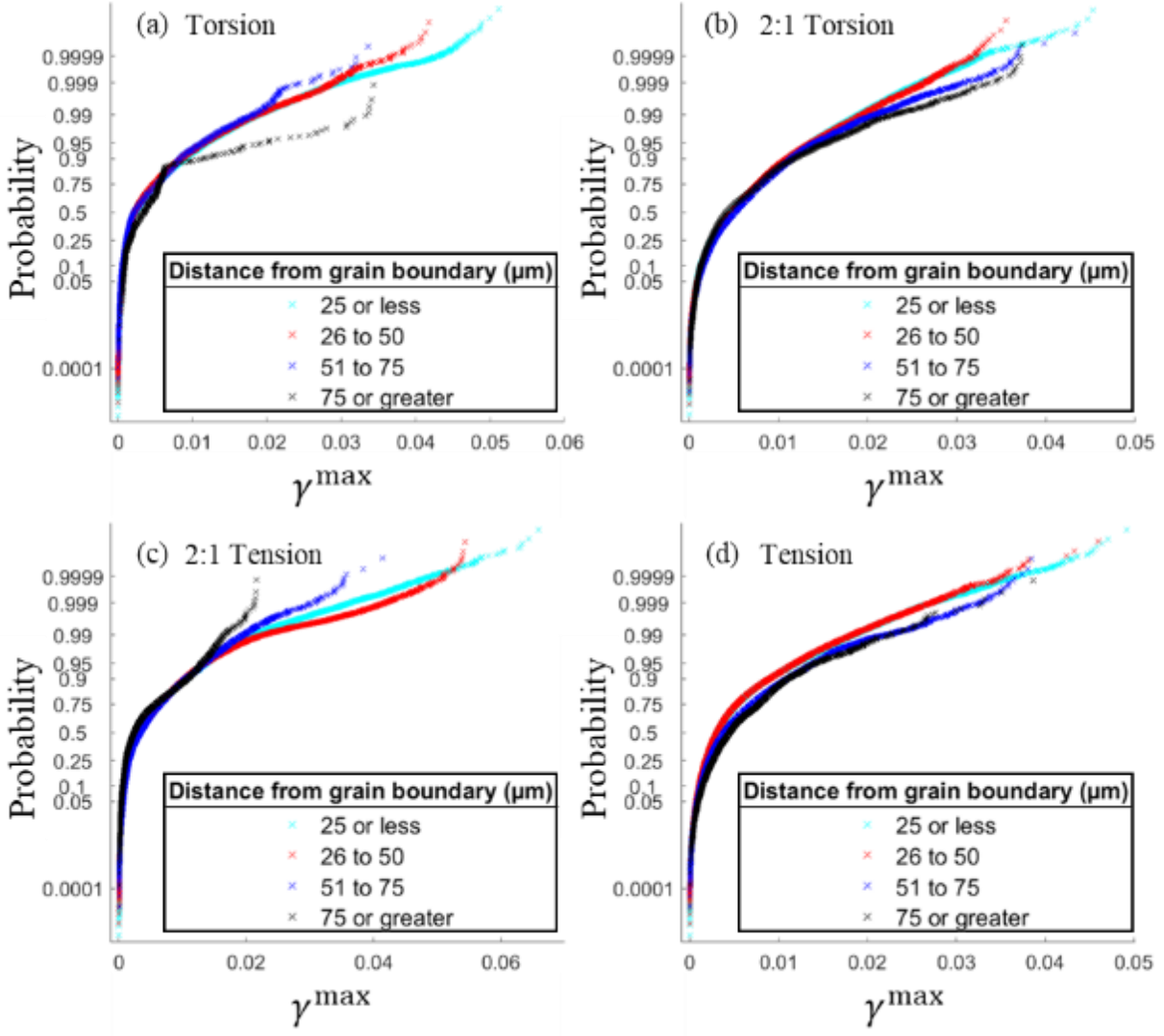
Figure 4.11: The distribution of γ^{max} as a function of the distance to the nearest GB, as shown for the (a) torsion, (b) 2:1 torsion, (c) 2:1 tension and (d) tension specimens.

4.3.3 The role of grain size and texture on the pathway of deformation bands

The probability of a DB interacting with a grain based on the grain size (diameter) is examined for all loading cases. Utilizing the skeletonized DBs and a percolation strain of 0.3%, grains with and without DBs were partitioned into two categories. For all specimens, the largest grains had the highest probability of containing a DB, as shown in Figure 4.12. On average, DBs formed in grains whose diameter were 1.6 times larger, than grains without DBs.

The preference for DBs to form in a specific crystallographic orientation, relative to the plane of MSS, was examined for all grains within each specimen. For each specimen, the grain orientations were rotated by the angular difference between the specimen's longitudinal axis and the specimen's plane of MSS (about an axis normal to the plane of polish). An inverse pole figure projected onto the plane of MSS was created for each specimen, where grains with and without DBs are represented for a percolation strain of 0.3%, as shown in Figure 4.13. No clustering toward a given crystallographic orientation was observed within the inverse pole figures, indicating no strong preference for DBs to form within a specific grain orientation, relative to the plane of MSS. The same analysis was repeated for the larger percolation strains, 0.6% and 0.9%, and for all percolation strains utilizing an inverse pole figure projection along the specimen's longitudinal axis, no preferred crystallographic orientation was observed for DB formation. The absence of a preferred grain orientation for DB formation is not surprising due to the weak fiber texture of the material.
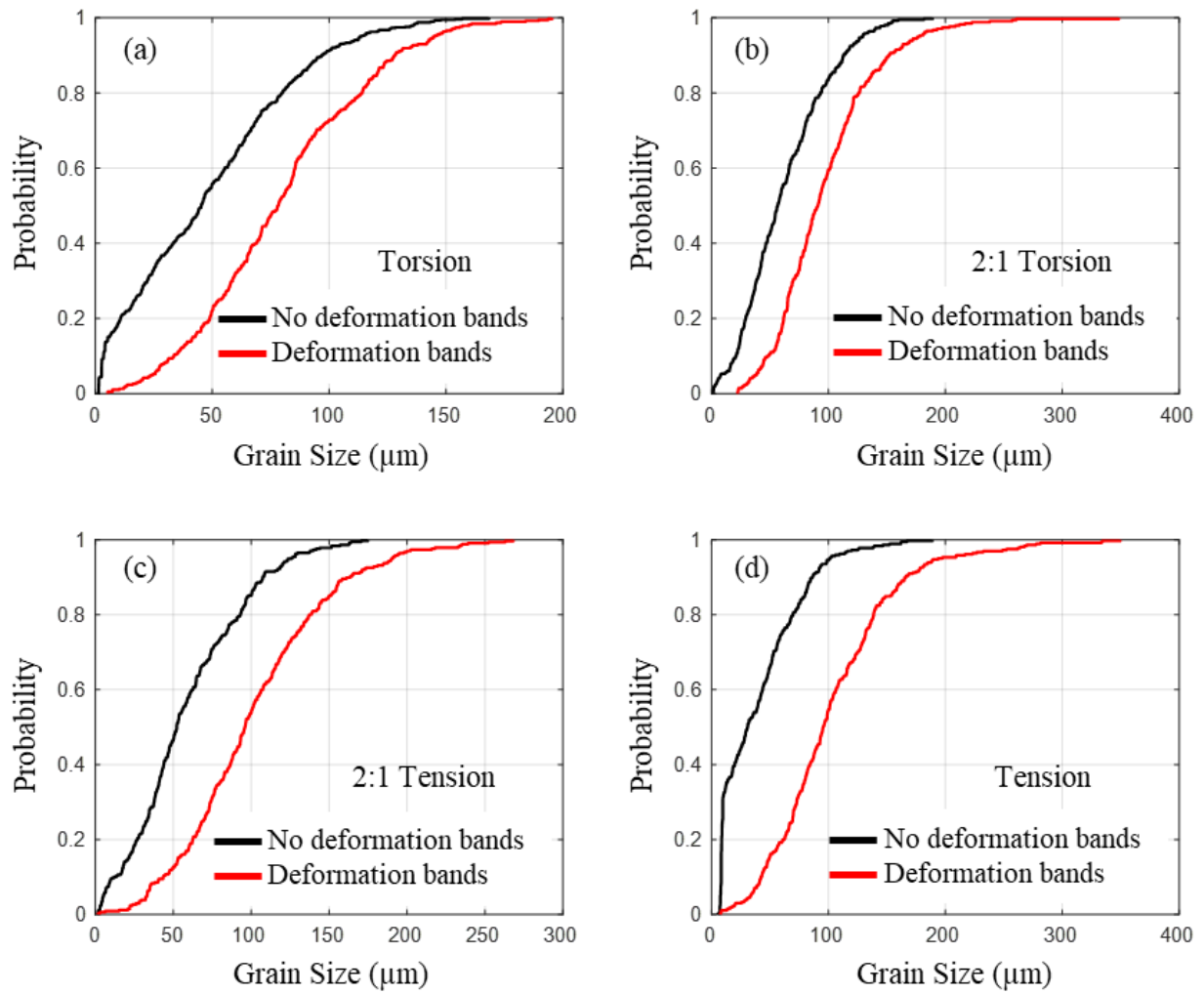
Figure 4.12: The cumulative probability that DBs exist within grains as a function of size, as shown for the (a) torsion, (b) 2:1 torsion, (c) 2:1 tension and (d) tension specimens.
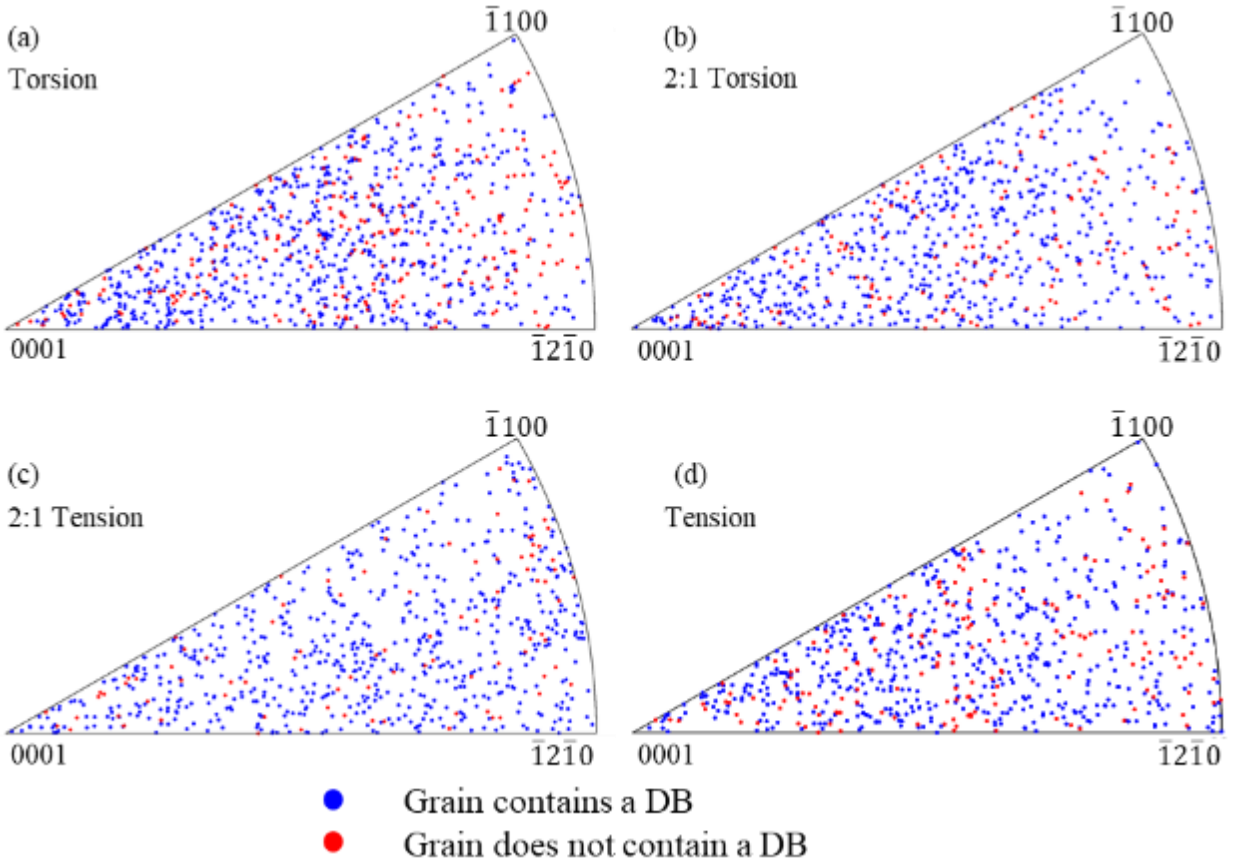
Figure 4.13: Inverse pole figure projection of every grain with respect to the plane of MSS within the (a) torsion, (b) 2:1 torsion, (c) 2:1 tension and (d) tension specimens. Grains that contain a DB are shown in blue, while grains that do not contain DBs are shown in red.

4.3.4 RVE sizing considering the residual deformation state and deformation band features

The methodologies presented in Section 4.2.4 established a relationship between the macroscopic strain state of the material, the macroscopic approach, and the number of DBs required to achieve an equivalent deformation state within a RVE, the micromechanical approach. The $\tilde{r}$ for each specimen is shown within Figure 4.14a. At RVE edge lengths above 1000 µm the $\tilde{r}$ for all specimens are observed to converge, and above 1500 µm, the difference between individual specimens becomes negligible. The $\tilde{r}_{\emptyset}$ of all specimens is shown in Figure 4.14b. At RVE edge lengths above 1000 µm the $\tilde{r}$ for all specimens are observed to converge, and above 1500 µm, the difference between individual specimens becomes negligible. A RVE edge length of 1610 µm minimizes $\tilde{r}_{\emptyset}$ and would encompass 446 grains of average diameter, 86 µm. The number of DBs that would appear in a RVE with an edge length of 1610 µm is calculated utilizing the mean DB measurements from Figure 4.7 and Eq. 4.6. Approximately 18 DBs are required for the full range of percolation strains investigated as notated in Figure 4.14b.
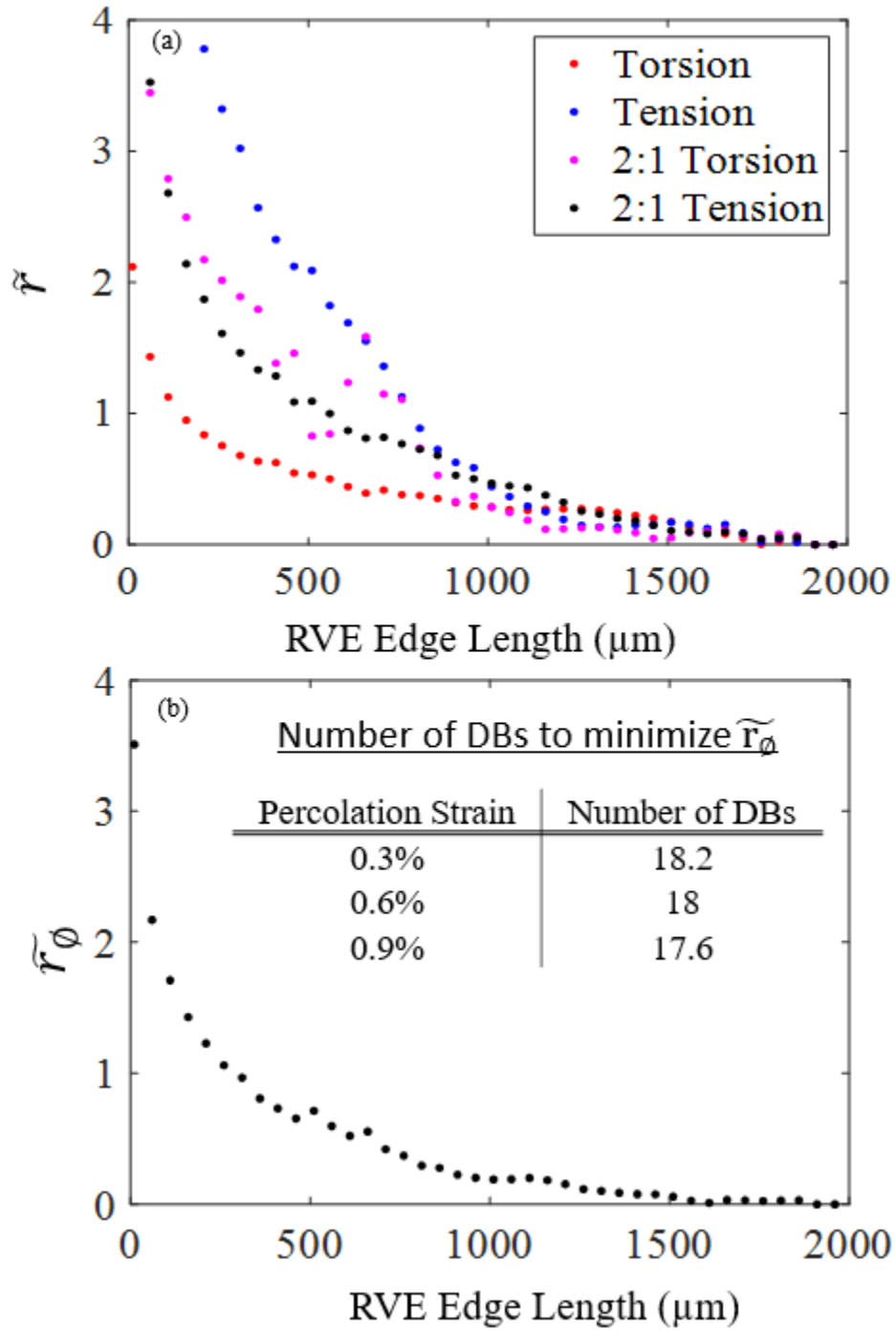
Figure 4.14: (a) The average macroscopic error, $\tilde{r}$, and (b) the overall mechanical error, $\widetilde{r_\emptyset}$, are shown as a function of the RVE edge length. The number of DBs, which minimize $\widetilde{r_\emptyset}$ are noted for each percolation strain.

4.4   Discussion

The macroscopic tension torsion stress states resulted in plastic flow that formed DBs, which spanned multiple grains, as shown in Figure 4.3 and Figure 4.4. The presence of distinct deformation pathways through the microstructure were explicitly shown by Abuzaid et al. [14]. From such studies of uniaxial loading utilizing DIC, deformation bands are well aligned with the plane of MSS, yet from this single condition, the role of the microstructure was not able to be distinguished from the overall applied loading condition. In this study, the development of the DBs was assessed in relation to (i) the plane of MSS and (ii) microstructural features. Additionally, a mesoscale RVE edge length was determined which captured the variability in the mechanical response of the experiments as well as the DB features.

The DBs with the longest lengths and having the largest strains were found to be nearly coincident with the plane of MSS as determined by a Mohr's circle analysis for each loading condition. The distinct orientation and magnitude of DBs within the microstructure has been referred to as strain patterning. Utilizing DIC with slip band resolution, Lunt et al. [121] quantified the spatial strain variation based strain patterning features, but did not address how the strain pattern was affected by the presence of GBs. In addition to agreeing with the continuum solution, the DBs identified utilizing the largest percolation strain, 0.9%, were found to be the least perturbed by GBs, as shown in Figure 4.10. In a way these DBs act as a conduit though which the largest deformations are accommodated. Past studies have shown that deformation which is inter-connected over two or more grains results in higher slip intensities along slip bands [122], promotes crack initiation [9], and are ultimately locations of material failure [16,80]. These results are consistent with the previous literature regarding slip inter-connectivity.

In tandem with DBs parallel to the plane of MSS, DBs of smaller length and having lower amounts of strain formed at orientations that differed from the plane of MSS to maintain compatibility within each specimen. This behavior is shown in Figure 4.8, where portions of DBs can be seen deviating nearly perpendicular to the plane of MSS. Previous studies discuss the importance of compatibility between grains, wherein deformation of one grain requires the neighboring grains to also accommodate deformation such that the interface between the grains remains intact [123–125]. This constraint creates stresses within the neighboring grain [28,126] and may cause deformation to occur in a direction that does not coincide with the plane of MSS. Further, high energy x-ray diffraction microscopy (HEDM) experiments show that in the presence of a

macroscopic uniaxial stress the grain level stresses produced are often similar in magnitude but occur in the all directions, including the directions normal to the applied load [127]. Utilizing HEDM, Chatterjee et al. [128] observed large variations in stress triaxiality within neighboring grains in Ti7Al, positioning GBs as preferred sites for deformation deviation.

The largest deviation of DBs from the plane of MSS were found to coincide with GBs, wherein a DB would deviate along a GB. The stress near GBs is greater due to the obstruction of dislocation motion [29] and the aforementioned compatibility related stresses. In this study, the DBs with the lowest percolation strain, 0.3%, experienced the largest deviations near GBs as compared to the larger percolation strain DBs, as shown in Figure 4.10. This is in agreement with the theory of multi-slip [129,130] wherein the number of slip systems activated is governed by the amount of deformation accommodated, therefore larger percolation strain DBs have less deflection because of the increased slip system actively near the GB region. This finding is in concurrence with Ashby [39], wherein the effect of internal grain level stresses on deformation were most impactful before the onset of larger strain events such as multi-slip, which relieve the internal stresses near the GBs.

RVE sizing for Ti7Al has been approached through a variety of characterization-based and simulation-based methodologies, which has in turn produced a range of effective RVE sizes, as shown in Table 3. The methodology of Balzani et al. [89] was modified in this study to apply the residual plastic strain to establish a RVE edge length. The novel aspects of the presented method are that the plastic strains measured through DIC are coupled to the global residual strain and that the required number of DBs for the RVE are determined. The reported RVE encompasses 446 grains and contain 18 DBs. The number of grains required in the presented RVE fall in the middle of Ti7Al RVE investigations from the literature, which required between 200 grains and 750 grains, as shown in Table 3. The number of grains within the RVE presented in this study (446 grains) is 10% and 15% lower than the mean (493 grains) and median (515 grains) number of grain presented in literature-based Ti7Al RVEs [85,88,131,132], respectively. A subset of the RVEs from the Ti7Al literature are presented in Table 3. The presented RVE required fewer grains than many of the past Ti7Al RVE investigations, this could be partially due to image resolution. As image magnification is increased, greater degrees of strain heterogeneities become visible [87]. This added variability will increase the number of grains needed within the RVE. Ti7Al is a model material for more complex α/β titanium alloys, such as Ti-6242S (Ti-6Al-2Sn-4Zr-2Mo-0.1S by wt. %) and Ti-6242 (Ti-6Al-2Sn-4Zr-2Mo by wt. %). RVEs which have been utilized to instantiate CPFE simulations were

selected from literature to compare with the current study [133–136], a subset of which is shown in Table 3. The number of grains within the RVE presented in this study (446 grains) is 9% and 5% higher than the mean (408 grains) and median (423 grains) number of grains presented in the Ti-6242S and Ti-6242 RVEs from literature [133–136], respectively. The number of grains required to capture the DB statistics and macroscopic deformation behavior is also in agreement with stereological observations which found the number of grains required to capture the mean grain size of a material is 500 grains [137]. Although the number of grains is similar when comparing the presented RVE and literature based RVEs the DB features tracked in this study are not readily visible in the literature RVEs. This difference is due to the surface area disparities which can be represented as a number of grains per edge length of the RVE. Comparatively, the RVE presented in this study requires, on average, between 1.6 and 2.5 times more grains per edge length, 18.7 grains per edge length, as compared to the Ti-6242(S) (11.9 grains per edge length) and Ti7Al (7.3 grains per edge length) literature values, respectively. Increasing the number of grains per edge length of future simulations may increase the likelihood of capturing these interconnected DBs. Overall, the presented RVE methodology requires that the number of grains per edge length be increased to capture the mesoscale DB features investigated in this study. The meso-scale RVE methodology or MPSS model described within this study is widely applicable and can be utilized with any feature of interest and the resulting in-plane strain information.

The limitations of single camera DIC and optical image resolution are acknowledged as potential sources of uncertainty in the current study. More specifically, a single camera approach does not capture any out-of-plane displacement data. While every effort was made to keep the specimen surface planar, some deformation details could have been unmeasured due to this constraint. It should be noted that the crystallographic slip events were not captured as discrete events as shown in many high-resolution DIC studies, instead they were homogenized due to the resolution limitations of optical microscopy. The presented RVE edge length was 80% of the AOI edge length in each specimen. Each AOI contained 690 grains of average size. Future studies should consider imaging larger AOI's, containing 1000+ grains of average size to ensure sufficient area available for analysis. Lastly, the size of the DBs described here were measured under quasi-static loading conditions at room temperature. It should be noted that previous work by Follansbee and Gray [138] demonstrated higher strain rates or temperatures increase the number of active

deformation mechanisms, such as twinning and cross-slip, within the alpha phase of titanium alloys. This may cause the DBs and the corresponding RVE edge length to vary in size.

Table 4.4: List of previous RVE investigations of Ti7Al, Ti-6242 and Ti-6242S. Ti7Al studies are ordered from largest to smallest number of grains per edge length. The method for determination and notes from each experiment are listed. The current study is highlighted.

Author	Material	Method for determination	Number of grains within RVE	Average grain size (µm)	Grains per edge length	Notes
Rotella, 2021	Ti7Al	See Sections 4.2.4 and 4.3.4	446	86	18.7	Current study
Ghosh, 2016 [132]	Ti7Al	2D EBSD characterization match of grain size and misorientation distributions	515, 529	40, 70	7.5, 13.7	Error metric minimized below 2% for RVEs containing more than 480 grains
Sangid, 2020 [88]	Ti7Al	Utilizing 3D HEDM measurements. Average or standard deviation of the sampled grains within 5% of the expected value.	200, 750	86	4.7, 7.3	The variability in the assessed quantities increases as a function of load. RVEs were evaluated at maximum load.
Ozturk, 2019 [85]	Ti7Al	2D EBSD characterization match of grain size and misorientation distributions	541	100	6.6	Micro-model used to evaluate regions of high stress in the macroscopic model.
Anahid, 2013 [133]	Ti-6242	2D EBSD characterization match of grain size and misorientation distributions	343	7.5, 15, 30	11.3	Stress fields from macroscopic FE models, micro-model informs trends in crack initiation
Zhang, 2020 [134]	Ti-6242S	2D EBSD characterization match of grain size and misorientation distributions	145	10.21	8.5	94% α-phase, small micro-model used to inform eigen deformation-based reduced-order model.

4.5   Conclusions

The following conclusions regarding the formation of DBs under various tension torsion loading conditions within Ti7Al were deduced from this work.

1. The DBs which formed parallel to the plane of maximum shear stress, as determined by the Mohr's circle approach, were observed to be the longest and carried the largest degree of deformation. The spatial distribution of DBs is influenced by grain size, as they form in grains that are, on average 1.6 times larger than the average grain size. The DBs did not prefer to form in grains with any specific crystallographic orientation.

2. In tandem with the DBs formed parallel to the plane of maximum shear stress, smaller DBs, in both length and degree of deformation, formed an interconnected network to maintain compatibility in the specimens. These inter-connected DBs were more susceptible to deviations from the plane of maximum shear stress and were occurred near GBs. The largest strain accumulations within DBs were observed to occur near GBs.

3. The mesoscale plastic strain sizing (MPSS) model utilized DB features and in-plane plastic strain measurements to establish a RVE edge length. Both the macroscopic residual deformation and underlying DBs were used in tandem to describe a mesoscopic RVE edge length that could capture the overall deformation response as well as the population of the DBs within the RVE. The overall mechanical error is minimized when the RVE edge length is 1610 µm, which encompasses an average of 446 grains and 18 DBs for all three percolation strains. As the RVE becomes smaller the mechanical response no longer matches the global response of the specimen, due to an exponential increase in the overall mechanical error. In order to capture well defined DB features within an RVE, this 2D analysis recommends 18.7 grains per RVE edge length which is significantly more than previous studies in the literature utilizing similar material.

5. THE ROLE OF INTER-CONNECTED SLIP DURING ROOM TEMPERATURE FATIGUE

5.1   Introduction

Since strain localization is a precursor to fatigue crack initiation [1]. Identifying features at the microstructural scale contributing to strain accumulation is critical to establish a physical understanding of the microstructural configurations that may promote cracking. As discussed in Chapter 2, grain clusters or supergrains have been observed to be nucleation site for material failure, however, to date there has been no experimental quantification of the enhanced strain accumulation due to these features. This research aims to quantify the accelerated strain accumulation along slip bands and grains which contain inter-connected slip bands as compared to those that do not. This chapter will address plastic strain accumulation with respect to slip bands, individual grains, and grain clusters using a Ni-based superalloy, RR1000. The specific analyses look to understand the plastic strain accumulation at varying length scales; investigating the intensity of slip within each slip band, progressing to the effect that slip transmission has on slip intensity, and finally analyzing the strain accumulation within groups of grains based on inter-connected slip bands. the alignment of slip systems in inter-connected slip bands, the role of grain neighborhoods, and the alignment of the micromechanical strains with the macroscopic deformation direction.

5.2   Determination of active slip systems via the Taylor Bishop and Hill algorithm

The following protocol is used to determine the active slip systems based on the DIC results and EBSD characterization and calculate a metric for the incremental slip on the active slip systems. In fcc materials, the octahedral slip systems are potentially active at room temperature and consist of the {111} slip planes and the corresponding <110> directions. In this study, the tracked plastic deformation is assumed to occur by crystallographic slip manifesting on the

aforementioned slip systems. The slip that occurs between the non-deformed material and a given loading step is defined as the incremental slip, dγ, corresponding to that block of fatigue loading. Taylor [123] stated that deformation occurs via multiple slip, on the five slip systems that minimize the amount of work needed to accomplish the deformation, following the principle of minimum work. Work, W, is defined, by Eq. Eq. 5.1,

$$W = \sigma_{ij} \cdot d\varepsilon_{ij}^{p} \hspace{3cm} \text{Eq. 5.1}$$

where σ_{ij} is the stress tensor and $d\varepsilon_{ij}^{p}$ is the change in plastic strain between deformation states. There are two drawbacks to using the Taylor model. First, the stress state corresponding to the five active slip systems may not physically exist. Second, the solution of which five slip systems are active is not unique, as more than one set of five slip systems can have an equivalent work as another set of five slip systems. This ambiguity can be handled via the maximum work principle proposed by Bishop and Hill [139], in which the stress state that results in the largest amount of work being done is selected as the operative stress for a prescribed strain state within a given grain. Selection of the operative stress state is dictated by the yield locus of the material. Each vertex on the yield surface corresponds to a stress state that activates multiple slip systems, which are necessary for plastic deformation. The fcc yield locus has 56 vertices, thus for a given strain state the work must be calculated at each yield surface vertex, using Eq. Eq. 5.1. The vertex stress state that results in the maximum amount of work is chosen as the unique stress state and will dictate the active slip systems within a crystal. One ambiguity that arises as a consequence of a vertex stress state is the specific direction of the plastic deformation on the yield surface. In plasticity, the normality condition indicates that plastic deformation, at a point on the yield locus, occurs perpendicular to the yield surface. Thus, each vertex stress state has a cone of normal vectors that are possible. This ambiguity will be addressed later through an iterative method resulting in convergence.

Using the Bishop and Hill principle of maximum work, the active slip systems were determined in this study using the following data: strains measured from ex-situ DIC within an SEM, in which the elastic strain is assumed to be negligible, EBSD measured crystal orientations, and information about the crystallographic structure, including fcc slip systems and yield locus stress states. First, the DIC strain and EBSD orientation data were spatially amalgamated, utilizing the aforementioned fiducial markers, resulting in a two-dimensional matrix containing point by

point data, such that each point in the dataset could be treated as its own crystal. Each data point contained three in-plane strain tensor components measured from DIC, e.g., the ε_{xx}, ε_{xy}, and ε_{yy} components corresponding to the axial, transverse, and shear strains, respectively. Assuming plastic incompressibility, a fourth component, ε_{zz}, can be obtained at each pixel location by applying Eq. Eq. 5.2.

$$\varepsilon_{zz} = -\left(\varepsilon_{xx} + \varepsilon_{yy}\right) \qquad \text{Eq. 5.2}$$

An assumption was made that the out of plane shear components of this tensor are zero since no information in these directions is measured in a single camera DIC setup. Strain data collected via DIC represents the increment of plastic strain, $d\varepsilon_{ij}^p$, from a reference state. Due to the uniaxial loading condition, the increment of plastic strain is equated to the deformation rate tensor, $d\varepsilon_{ij}^p = D_{ij}$, which has two implications – first, the rate formulation is discretized into a single strain increment, and second, the applied deformation increment is naturally expressed as a symmetric tensor. The deformation rate tensor is rotated from sample to crystal frame for each grain within the polycrystalline aggregate. The deviatoric terms of the deformation rate tensor can be extracted and used in Eq. A1 to find the maximum work by sampling each of the 56 unique stress states. The vertex stress state corresponding to the maximum work is selected as the initial guess for Eq. Eq. 5.3, σ_{pq}.

$$D_{ij} = F_{ijpq}\sigma_{pq} = \left[\sum_{\alpha=1}^{s} \left(\frac{\dot{\gamma}_o}{\bar{\tau}} \left| \frac{\tau^\alpha}{\bar{\tau}} \right|^{n-1} (\mathcal{M}_{ij}^\alpha)(\mathcal{M}_{pq}^\alpha) \right) \right] \sigma_{pq} \qquad \text{Eq. 5.3}$$

Equation Eq. 5.3 is a summation of shear strain increments over all slip systems [140–143], where α is the slip system that is currently being evaluated. In this case, s = 12, to account for the octahedral slip systems in a fcc crystal. Here $\mathcal{M}_{ij}^\alpha$ and $\mathcal{M}_{pq}^\alpha$ are the Schmid tensors. The Schmid tensor is defined in Eq. 5.4 as,

$$\mathcal{M}_{ij} = \frac{1}{2} \sum_{\alpha=1}^{s} \left(b_i^\alpha n_j^\alpha + b_j^\alpha n_i^\alpha \right) \qquad \text{Eq. 5.4}$$

where b^α and n^α define vectors that represent the slip direction and slip plane normal, respectively. The remaining variables are defined as $\bar{\tau}$ is the reference stress; $\dot{\gamma}_o$ is the reference shear strain rate;

and n is the strain rate sensitivity. The primary objective in this analysis is to determine the active slip systems and a scaled value of the shear strain increments, thus the kinetics of plasticity are simplified by taking $\dot{\gamma}_o = \bar{\tau} = 1$, and the exact magnitude of stress is not explicitly calculated. The analysis is also simplified by assuming rate insensitivity, n = 20. By using a Newtown-Raphson solver, the deformation rate tensor, D_{ij}, is calculated by iterating the stress, σ_{pq}, multiplied by a fourth order tensor, F_{ijpq}, until the calculated deformation rate tensor is equal to the one measured during the DIC experiment. With the converged stress state, $\sigma_{pq_{Converged}}$, determined, Schmid's Law is used to calculate the resolved shear stress, τ^α, on each slip system using Eq. 5.5[11].

$$\tau^\alpha = \mathcal{M}^\alpha_{pq}\sigma_{pq_{Converged}}$$

<div align="right">Eq. 5.5</div>

The resolved shear stress is used in a power law relation, from Hutchinson [140], to calculate the shear increment, $d\gamma^\alpha$, on each slip system, as shown in Eq. 5.6.

$$d\gamma^\alpha = \frac{\dot{\gamma}_o}{\bar{\tau}}\left|\frac{\tau^\alpha}{\bar{\tau}}\right|^{n-1}\tau^\alpha$$

<div align="right">Eq. 5.6</div>

This procedure interprets each correlation point of the DIC data set as its own crystal, thus allowing the identification of slip system activity based on the fcc yield locus and prescribed strain.

 Using the aforementioned scheme, the DIC results were used to calculate the incremental slip on each slip system. Figure 5.1(a) displays the axial strain for a sub region containing two grains following 1 cycle of deformation. Slip bands are observed to have formed inside of both grains located inside this subsection. Incremental slip was calculated at each loading step, 1 and 1000 cycles are shown for the sub region in Figure 5.1 (b) and (c), respectively. Incremental slip in the bottom grain on the $(11\bar{1})$ [101] slip system increases with increased cycling, while this $(11\bar{1})$ [101] slip system is not active in the top grain. The active slip system's plane was verified by slip trace analysis, where each (111) slip plane was resolved into the crystal reference frame and matched to the slip band's normal direction observable in the DIC results. Additionally, the direction of the slip increment, in the laboratory reference frame, was verified by comparing these directions for a few selected slip bands with the relative in-plane displacement values, u and v, from DIC.
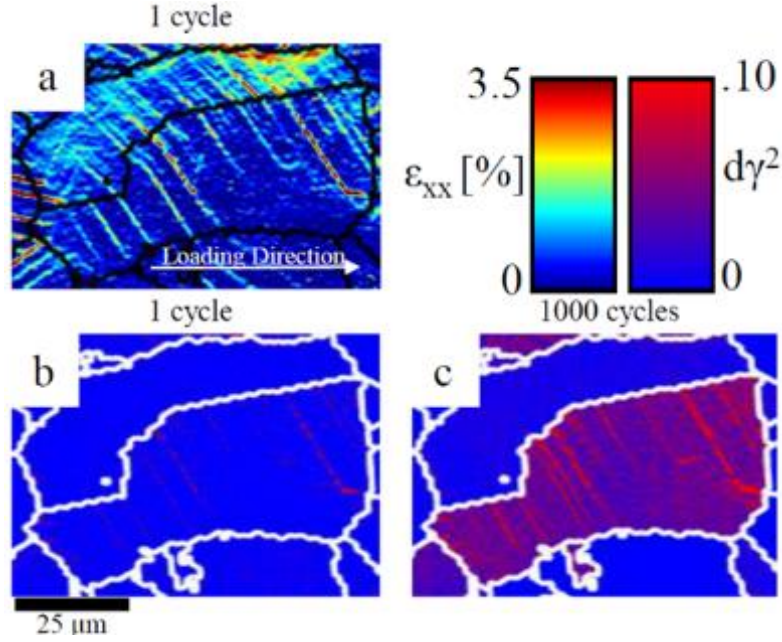
Figure 5.1: (a) A subsection of the axial strain component, ε_{xx}, map following 1 cycle of deformation. The calculated incremental slip on system $d\gamma^2$ following (b) 1 cycle and (c) 1000 cycles of deformation of the same grain. Slip system, $d\gamma^2$, is the $(11\bar{1})$ $[101]$.

5.3   Results

DIC was conducted on materials C1 and C2, of which the corresponding axial strain component maps are shown in Figure 5.2. After one cycle, the strain maps corresponding to both AOIs display the presence of discrete planar slip bands presumed to be the result of shearing γ' precipitates 37. With continued deformation, following 10 and 100 cycles, strain accumulates in the vicinity of GBs, in addition to an increased magnitude of strain accommodated within each slip band. After 1000 cycles, strain is no longer only concentrated along slip bands or at GBs, but instead relatively high levels of strain, 2% or more, are measured between slip bands within many grains. The average axial strain measured within each AOI following cycling is summarized in Table 5.1. After the first cycle, no new slip bands form via observations from the DIC strain maps; instead, the slip bands increase in their measured strain magnitude. Each strain map provides the opportunity to analyze multiple length scales of strain accumulation, starting at the slip band level. Data collection and analysis was conducted on both microstructural variants to ensure the consistency of the reported trends, for ease of communication, only the C2 variant will be discussed.

73
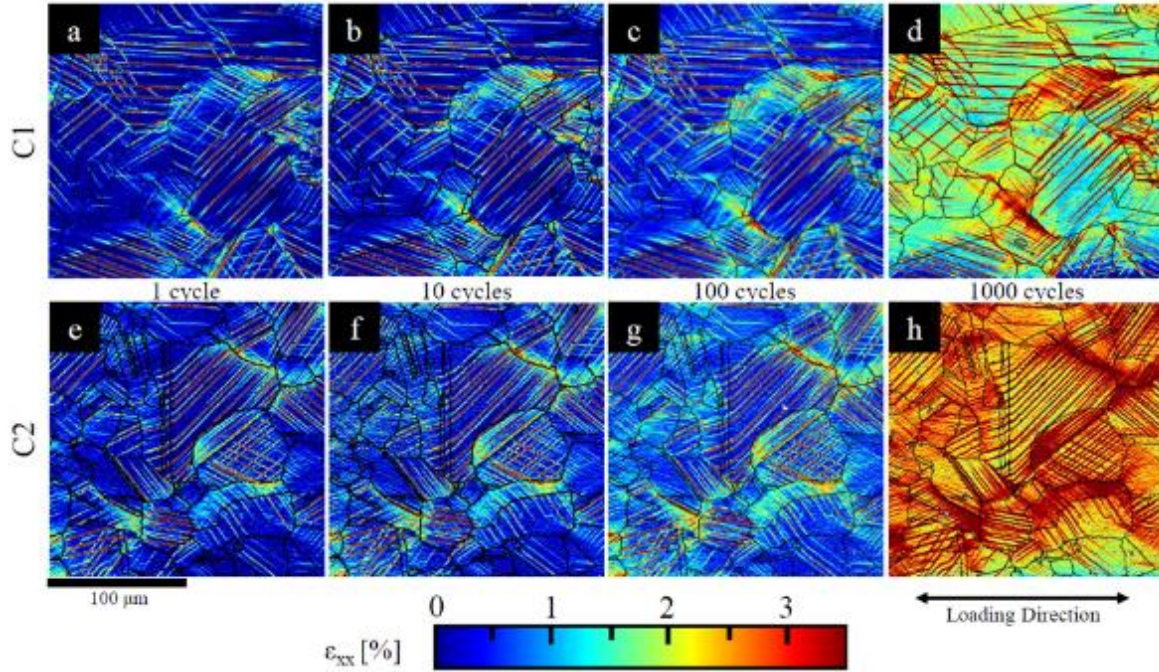
Figure 5.2: Axial strain component, ε_{xx}, strain maps of C1 (top row) and C2 (bottom row), at 1, 10, 100, and 1000 fatigue cycles. Areas colored white have a low confidence index and were removed from the analysis. Black lines represent GBs.

Table 5.1: Axial component strain, ε_{xx}, measured within the AOI after each block of fatigue deformation.

Deformation State	1 Cycle	10 Cycles	100 Cycles	1000 Cycles
C1	0.54%	0.73%	1.02%	2.13%
C2	0.66%	0.87%	1.13%	2.95%

5.3.1 Incremental slip intensity related to GB type

The active slip systems were determined, and the value of the incremental strain accommodated within an active slip band was calculated following the procedure described in the above paragraphs. The incremental slip was summed along each slip band utilizing a manually placed line profile that was 1 pixel thick, prescribed along the array of maximum incremental slip. The summed incremental slip was normalized with respect to the length of each unique slip band, this value will be denoted as the incremental slip intensity (ISI) throughout the remainder of the article. These ISI values are plotted against the length of the corresponding slip band and

categorized based on the type of boundary with which the slip band interacts, as seen in Figure 5.3a. HAGB are defined as boundaries between neighboring grains that have a misorientation value of $\geq 15°$ between adjacent grains. Coherent twin boundaries were defined according to the algorithm described in reference [144].
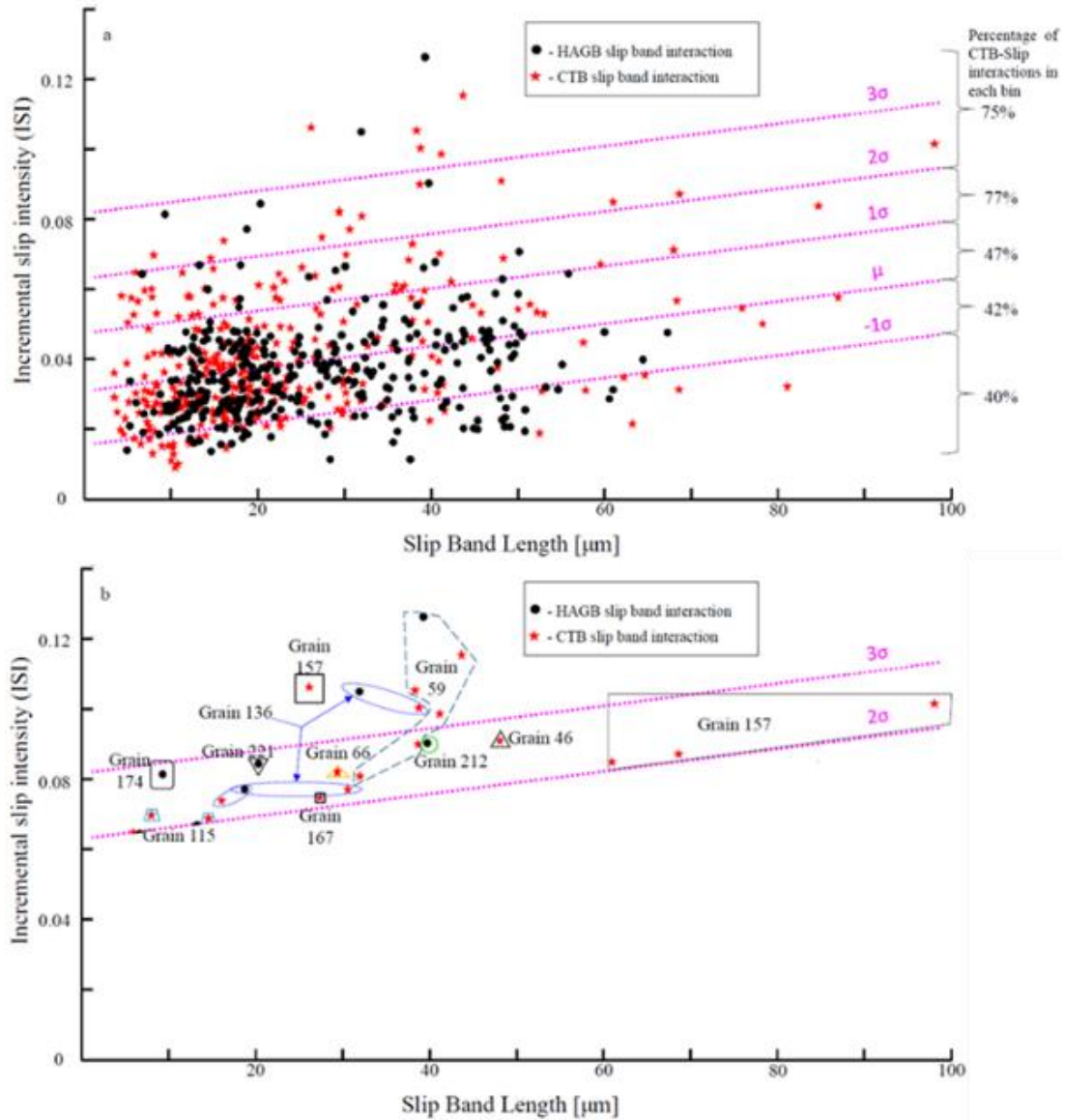
Figure 5.3: (a) Summary of all slip band interactions with HAGB and CTB shown in black and red, respectively. (b) Grains displaying incremental slip intensity values above two standard deviations have been outlined and labeled with grain ID number for later discussion.

Two low angle GBs, misorientation of <15° from a neighboring grain, were observed in the AOI, but neither boundary interacted with a slip band, thus they are not represented in this analysis. Active slip systems were chosen for analysis based on the highest magnitude of the slip increment calculated using Eq. 5.6. If two slip directions on the same plane had comparable values of the incremental slip metric, the system that minimized the residual Burgers vector ($\mathbf{b_r}$) was chosen for analysis in accordance with the third criterion proposed by Lee et al. [145]. A mean behavior line was fit to all ISI values with respect to the slip band length, denoted by μ within Figure 5.3a. The standard deviation is superimposed between -1σ and 3σ to further bin the ISI values, shown by the dashed lines. It was observed that the CTB-slip interactions account for over 75% of the plotted slip interactions above 1σ for the distribution of the ISI values, and CTB-slip interactions are less likely when inspecting lower binned ISI below the μ+1σ line. This result could mean that the CTB-slip interactions result in more strain localization compared to general HAGB-slip interactions, or these ISI values could be influenced to a greater extent by the grain neighborhood, as will be discussed next.

5.3.2 The role of grain neighborhoods

To investigate the effect that neighboring grains may have on one another, the grains displaying the largest ISI values are first studied. Inspection of Figure 5.3b shows ten grains, which have ISI values greater than two standard deviations from that of the mean behavior including grains with ID numbers: 46, 59, 66, 115, 136, 157, 167, 174, 212, and 221. These slip-boundary interactions have been encircled and labeled with the corresponding grain identifier in Figure 5.3b and Figure 5.4a. It is important to note that these grains have slip-boundary interactions with both CTB and HAGB, thus ruling out the presented GB character metric as the sole reason for their relatively large ISI values. Figure 4a shows the AOI in C2 with the axial strain component overlaid.
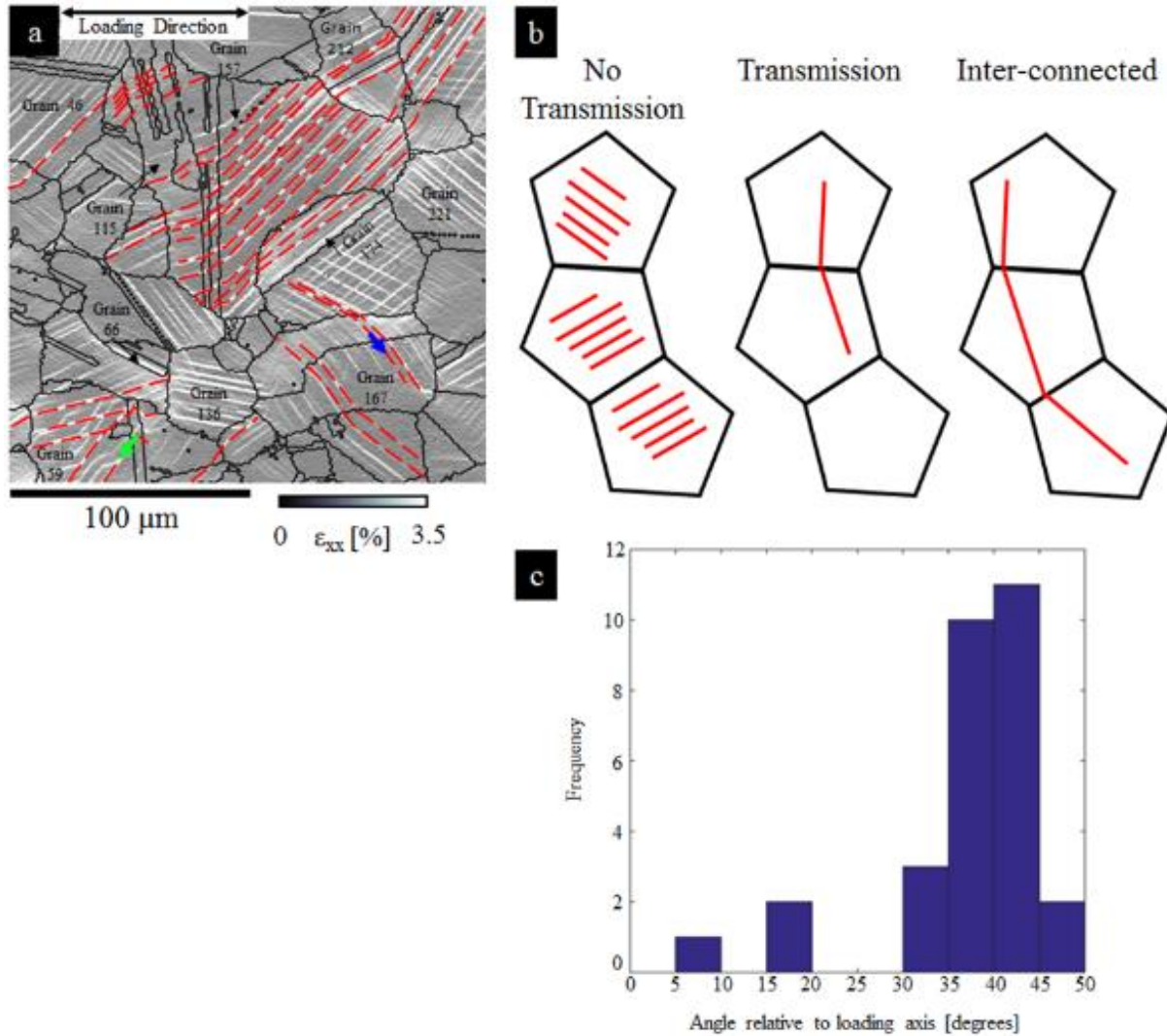
Figure 5.4: (a) The area of interest from microstructure C2, with grains labeled that were measured to have an incremental slip intensity above 2σ in Figure 3. The identified inter-connected slip bands in C2 are highlighted by red dotted lines in (a). The green and blue arrows serve as spatial identifying markers. These markers correlate with the highlighted alignment parameters and incremental slip traces shown in Figures 5 and 6, respectively. Shown in diagram (b) are three unique definitions of slip band configurations, based on slip transmission between neighboring grains. (c) The measured angle between each inter-connected band, as identified in Figure 5.4a, and the applied loading axis.

Red dashed lines trace out slip bands that have small deflections between these aforementioned grains resulting from slip transmission. These seemingly continuous bands of slip will be referred to as inter-connected bands. A representative schematic is presented in Figure 5.4b to categorize the inter-connectivity of slip within the microstructure. The first category, no transmission, is characterized by the lack of slip transfer between neighboring grains. The second category, transmission, consists of slip traversing through a single GB. The third category, an inter-connected band, consists of slip transmitting through two or more GBs. The average angle that each inter-connected band made relative to the applied loading axis was measured and the distribution of angles are shown in Figure 5.4c. Twenty-three of the twenty-nine inter-connected bands were measured between 35° - 50° from the tensile loading axis. This agrees well with the macroscopic plane of maximum shear stress located at 45° from the applied tensile loading axis of the specimen.

The average grain size of variant C2 is 33 μm ± 3 μm, while each inter-connected band measures between 40 and 130 μm. It should be noted that many bands ran outside of the AOI, and the actual length of the inter-connected bands is likely longer than reported. Furthermore, the inter-connected bands contained 7 of the 10 aforementioned grains with ISI values above 2σ in Figure 5.3b. This would suggest that there is a possible connection between these inter-connected bands and the associated high values of the calculated strain increments in these grains.

The alignment of the slip systems involved in the slip transmission events is investigated, in an effort to determine the effect neighboring grains have on one another's deformation behavior. To determine the alignment between slip systems in neighboring grains, a geometric scalar value, m′, and the $\mathbf{b_r}$ were calculated for each neighboring grain pair within an inter-connected band. Luster and Morris [146] designated the factor m′ to describe how well two slip systems are aligned based on their crystallographic orientation, as described in Eq. 5.7,

Eq. 5.7

$$m' = \cos(\theta) * \cos(\Phi)$$

where Φ is the angle between the incident and outgoing slip directions, and θ is the angle between the slip plane normals. Values of m′ range between 0 and 1. In the case of collinear slip systems, m′ will be equal to one. For a value of m′ approaching one, slip transmission between the two bordering slip systems is likely. In a case where either the slip planes or directions are nearly

orthogonal to one another, m′ will have a near zero value, and slip transmission is less likely on those specific slip systems.

In the general case of slip transmission considered here, an incident dislocation with a Burgers vector, $\mathbf{b_{in}}$, reacts with a GB to create both an outgoing dislocation in the adjacent grain with a Burgers vector, $\mathbf{b_{out}}$, and a residual Burgers vector, $\mathbf{b_r}$, that remains in the GB. The magnitude of the $\mathbf{b_r}$ is defined by conserving the original magnitude of the incident Burgers vector, as shown in Eq. 5.8. [147]

$$\mathbf{b_r} = \mathbf{b_{in}} - \mathbf{b_{out}} \qquad \text{Eq. 5.8}$$

For the case of slip transmission, necessary to form inter-connected slip bands, the alignment of the incoming and out-going slip bands was quantified, using the m′ and $\mathbf{b_r}$ metrics, as shown in Figure 5.5. Other slip metrics can also be considered when analyzing slip transmission between adjacent grains, the slip metrics m′ and $\mathbf{b_r}$ considered here are deemed sufficient based on prior studies [145,146,148,149] and review of slip transmission criteria [150,151]. The effect of slip system alignment on the incremental slip accumulation at a GB was evaluated for each neighboring grain pair. Two extreme cases of slip system alignment were identified, representing slip bands interacting with GBs of relatively high and low m′ values, as shown in Figure 5.6. The slip direction is highlighted via colored arrows. These colors also correspond to Figure 5.4 and Figure 5.5 which show the spatial location of these GBs and active slip system alignment values, respectively. In the case of slip transmission through a GB, with a geometric alignment value of m′ = 0.9997, the incremental slip values along the slip band were observed to remain nearly constant across the GB, between active slip systems, as shown in Figure 5.6a. In the second case, as shown in Figure 5.6b, representing slip transmission across a GB with a relatively low value of m′, the incremental slip values increased along the incident slip band as the GB was approached, such that the incremental slip was significantly higher in the incoming slip band as opposed to the outgoing slip band. This observation would suggest that the geometric alignment of the slip systems aids in the accumulation of strain along the slip band and therefore plays a role in the ease of slip through the intermediary GB.
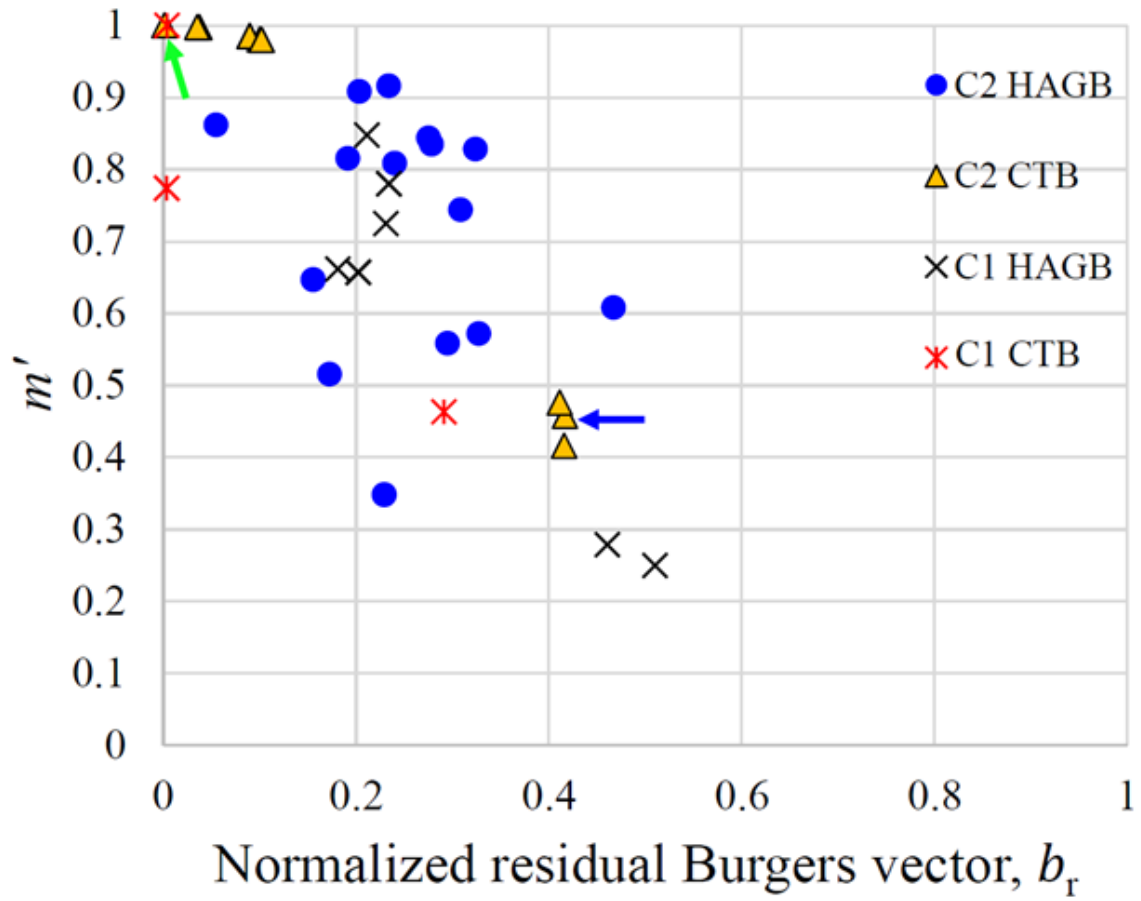
Figure 5.5: Displays residual Burgers vector plotted against m′ for C1 and C2. Interactions for HAGB and CTB are differentiated for each microstructure. Blue and green arrows highlight the interaction values for the previously shown slip traces in Figure 5.4 and incremental slip profiles shown in Figure 5.6. The residual Burgers vector was normalized by the magnitude of the full Burgers vector in this material.
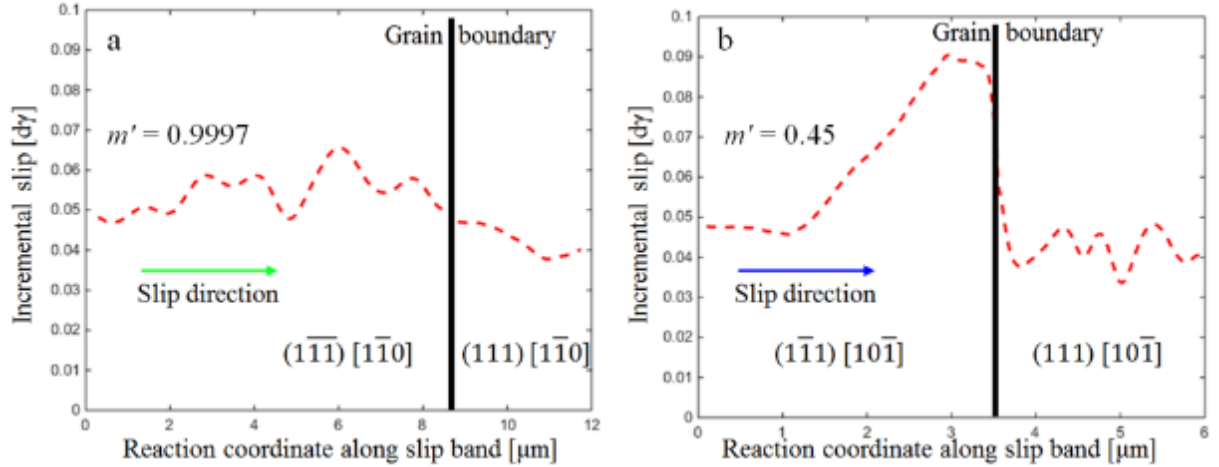
Figure 5.6: Incremental slip data extracted along slip bands that are part of an inter-connected slip band with a relatively, (a) high $m' = 0.9997$ and (b) low $m' = 0.45$. The colored arrows indicate slip direction and serve as color coded markers to identify these locations in previous Figures 4 and 5. The vertical black lines represent the GB locations. The in-going and out-going slip system information is superimposed within each grain and consists of the slip plane normal and slip direction.

The effect of inter-connected bands on the microstructural evolution of plastic strain was assessed at both the slip band scale, using the ISI, and grain scale, using the grain average strain, as shown in Figure 5.7 and Figure 5.8, respectively. In Figure 5.7 and Figure 5.8, each of the three categories of slip connectivity (i.e. no transmission, slip transmission, and inter-connected bands, as defined in Figure 5.4(b) are shown. It was found that inter-connected bands were more likely to accumulate larger values of ISI throughout cyclic deformation, as compared to both the no transmission and transmission cases, up to 1000 cycles. All datasets, excluding the cases of slip transmission and inter-connected slip following 100 cycles, were found to be statistically different from one another to a 95% confidence level. This suggests the accumulated shear on the most active slip system is dependent on the amount of inter-connectivity of each slip band between neighboring grains. When each grain is viewed holistically, using its value of grain average strain, a similar trend emerges, as shown in Figure 5.8. Here, grains that contained inter-connected slip bands experienced a larger degree of strain accumulation during cyclic deformation. However, following 1000 cycles, the average strain within grains containing inter-connected bands and slip transmission were not statistically different, to a 95% confidence level. This suggests that initially the inter-connected slip bands are preferred pathways for strain accumulation, and during cyclic

loading, these slip systems within the inter-connected slip bands may experience hardening, which would cause the deformation to be accommodated in neighboring grains.

5.4   Discussion

5.4.1   Neighboring grains and strain localization

The metrics used to quantify slip systems alignment, m′ and $\mathbf{b_r}$, of the incoming and out-going slip bands, along the inter-connected slip bands, were seen to vary inversely to one another, as shown in Figure 5.5. It has been observed, both experimentally and through atomistic simulations [21,148], that in the case of slip transfer between grains that produced residual GB dislocations, a pile-up of dislocations proceeded the transmission event. In this study, poorly aligned slip systems, in terms of the m′ value, were observed to accumulate a significantly higher value of the incremental slip on the incident slip band at GBs, as shown in Figure 5.6, resulting in possible large stress concentrations [29].

Inter-connected slip bands allowed a series of grains to deform in concert, analogous to grain clusters, previously discussed in the introduction [9]. Further, when slip was observed to transmit across one or multiple GBs, the ISI and grain average axial strain were seen to increase, as seen in Figure 5.7 and Figure 5.8. Following 1000 cycles, the mean ISI value is, on average, 22% higher for slip bands that are part of an inter-connected band as compared to slip bands contained within a single grain. Additionally, Figure 5.7d shows the ISI values in the upper tail of the distribution are as much as 50% greater within the inter-connected bands as compared to the case of no slip transmission. When each grain is considered, it was found that grains, in which inter-connected slip occurred, had on average 60% and 30% higher axial strains following 1 and 1000 fatigue cycles, respectively. This finding indicates that grains within inter-connected bands deformed more quickly and continued to accumulate more strain throughout cyclic loading. Based on these results, grain clusters exhibit a larger degree of strain localization than the other grains in the AOI and provides a rationale for the grain cluster model of crack initiation [9,65].
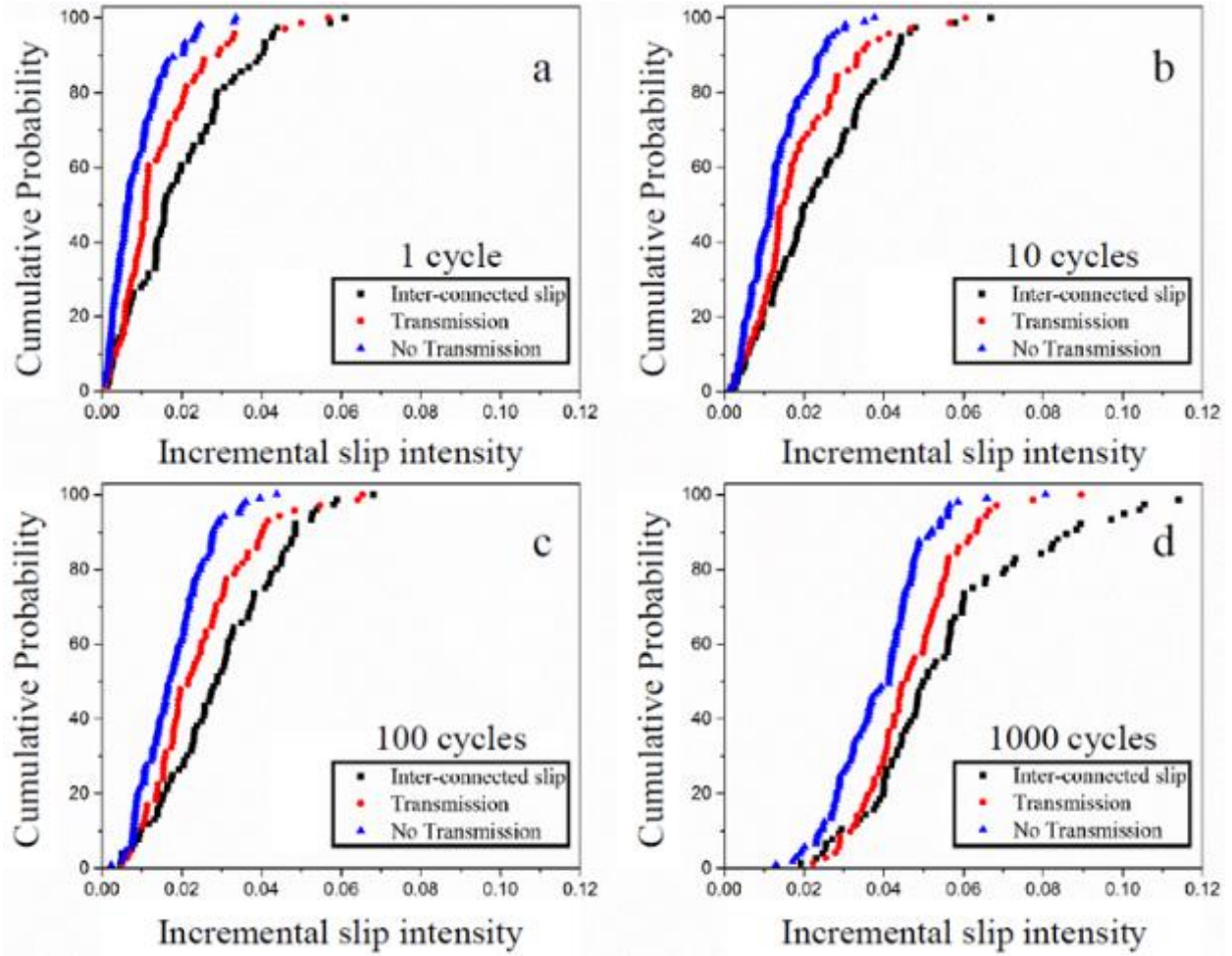
Figure 5.7: The distribution of the incremental slip intensity as a function of cyclic evolution and slip band inter-connectivity. The cyclic evolution of each slip band category is shown at 1, 10, 100, and 1000 cycles in (a), (b), (c), and (d), respectively.
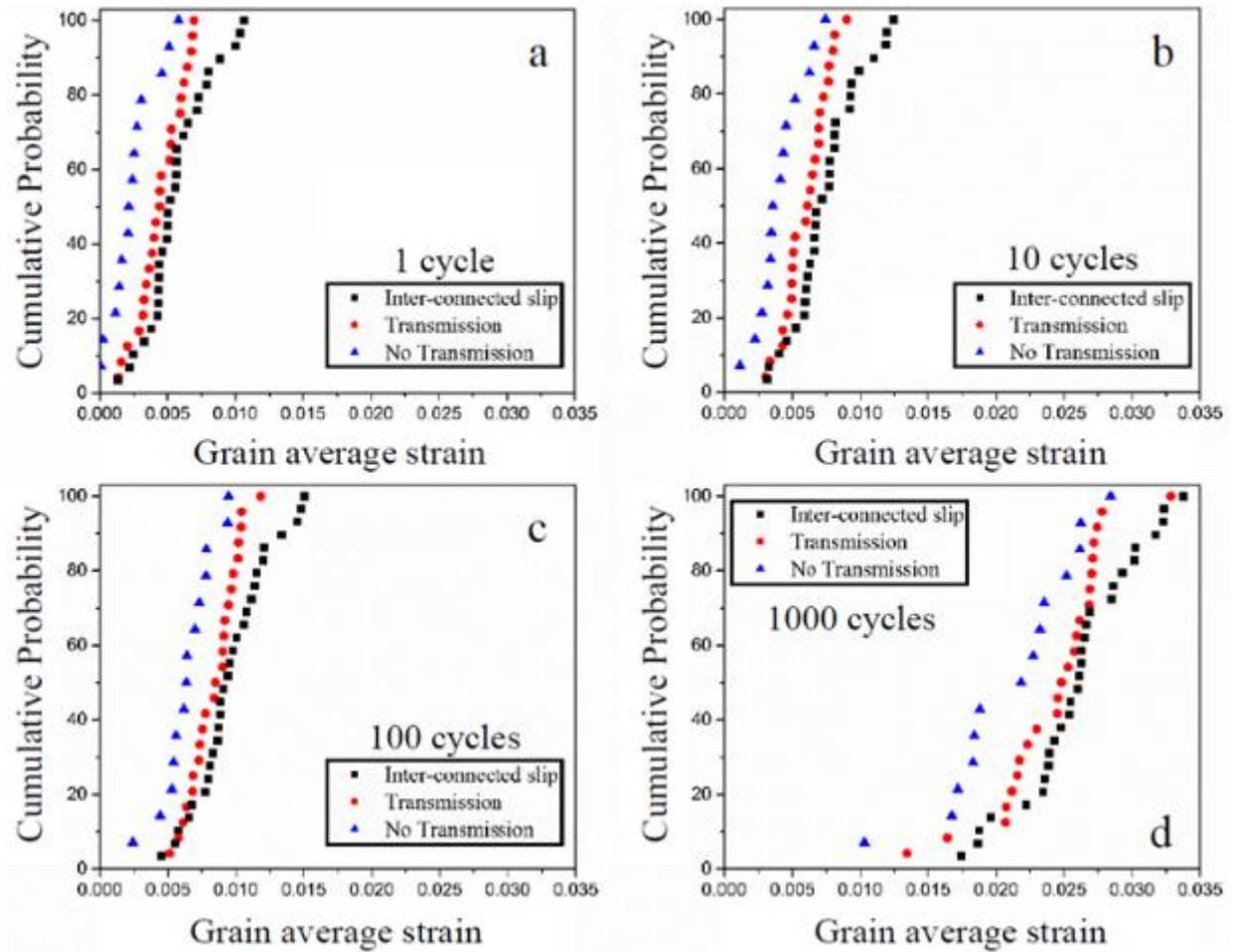
Figure 5.8: The distribution of the grain-averaged strain as a function of cyclic evolution and slip band inter-connectivity. The cyclic evolution of each grain category is shown at 1, 10, 100, and 1000 cycles in (a), (b), (c), and (d), respectively.

Within the AOI, the inter-connected slip bands were measured to be between 1 - 3.5x times larger than the average grain diameter in the material. Well aligned slip systems permitted neighboring grains to act in concert, as one large grain, resulting in the densest strain accumulations within the microstructure, as suggested by the supergrain theory [16]. The quantified stain localizations observed within the grain clusters, position these features as potential crack initiation sites, and thus limit the life of these materials.

In a practical context, microstructural variability, resulting in distributions in the microstructural features, is expected due to the numerous alloys elements, multi-tiered precipitate structure, and complicated processing routes, which are exacerbated when components are produced by various suppliers. These variabilities could manifest as a difference or mixture of grain sizes within a component, similar to the AOI investigated. The analysis performed in this work is helpful to ascertain failure at the microstructural level due to inter-connected slip and demonstrates that one large grain connected via inter-connected slip band to many small grains could be driving failure within Ni-based superalloys as seen by the previous authors.

5.4.2   Strain coaxiality

The distribution of stress and subsequently the accumulation of plastic strain within polycrystalline materials are important factors in determining their performance and lifetime. Ritz et al. [152] observed through finite element simulations, in uniaxial deformation, crystal stresses will tend toward a vertex on the single crystal yield surface (SCYS) during plastic deformation, that is most aligned to the macroscopic loading axis. The degree to which the crystal stresses can be aligned with the macroscopic loading axis is dictated by the vertices on the SCYS. Since this alignment in crystal stresses occurs in the plastic regime, the measured plastic strain data will be used to examine the resulting alignment of plastic strains with the macroscopic deformation axis using a strain coaxiality analysis.

Using the strain data from each fatigue loading sequence, presented in Figure 5.2, the strain coaxiality, Ω, was calculated in both microstructures using Eq. 5.9, and the strain coaxiality evolution, with cyclic loading, is shown in Figure 5.9.

$$\Omega = \cos^{-1}\left(\frac{\begin{bmatrix} 1 & 0 \\ 0 & 0 \end{bmatrix} : \begin{bmatrix} \varepsilon_{xx} & \varepsilon_{xy} \\ \varepsilon_{xy} & \varepsilon_{yy} \end{bmatrix}}{\mathrm{norm}\left(\begin{bmatrix} 1 & 0 \\ 0 & 0 \end{bmatrix}\right) * \mathrm{norm}\left(\begin{bmatrix} \varepsilon_{xx} & \varepsilon_{xy} \\ \varepsilon_{xy} & \varepsilon_{yy} \end{bmatrix}\right)}\right)$$

Eq. 5.9

Following 1 cycle of deformation, highly strained regions, such as slip bands and GBs, display low strain coaxiality or a high degree of alignment to the axis of macroscopic deformation, as seen in Figure 5.9 (a) and (e). Following cyclic loading, areas accumulating plastic strain continue to align with the macroscopic deformation axis, as shown in Figure 5.9 (b-c) and (f-g). The grain average strain coaxiality and grain average axial strain were compared for each grain within the AOI in C2, following each cyclic loading sequence, as shown in Figure 5.10a. For each grain within the AOI, as strain was accumulated during cyclic loading, the average strain coaxiality decreased. The strain coaxiality of grains displaying either no slip transmission or slip transmission, at 1 and 1000 cycles are shown in Figure 5.10 (b) and (c), respectively. Following 1 cycle, grains where slip transmission occurred were, on average, 10° more closely aligned with the macroscopic deformation axis as compared to grains where slip transmission did not occur. Following 1000 cycles, the heterogeneity of strain coaxiality, initially observed, is replaced by a more homogenous distribution as seen in Figure 5.9 (d) and (h). The average strain coaxiality, following 1000 cycles, is 17° and the degree of homogeneity is reflected in Figure 5.10c, where no difference in the strain coaxiality distributions is observed between grains where slip is confined to a single grain or grains experiencing slip transmission.
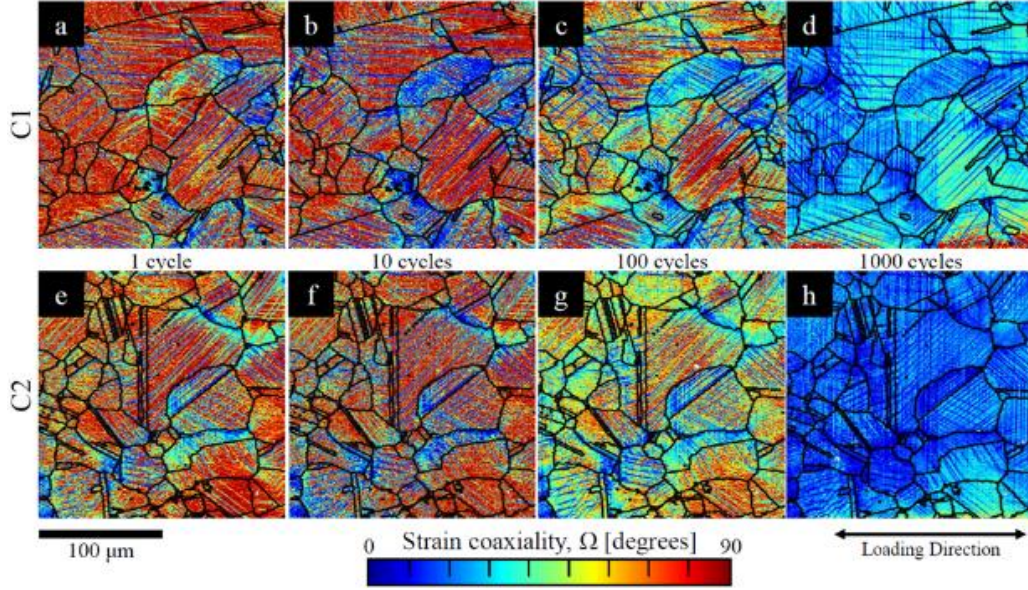
Figure 5.9: Cyclic evolution of strain coaxiality at 1, 10, 100, and 1000 cycles in microstructures C1 (a-d) and C2 (e-h).
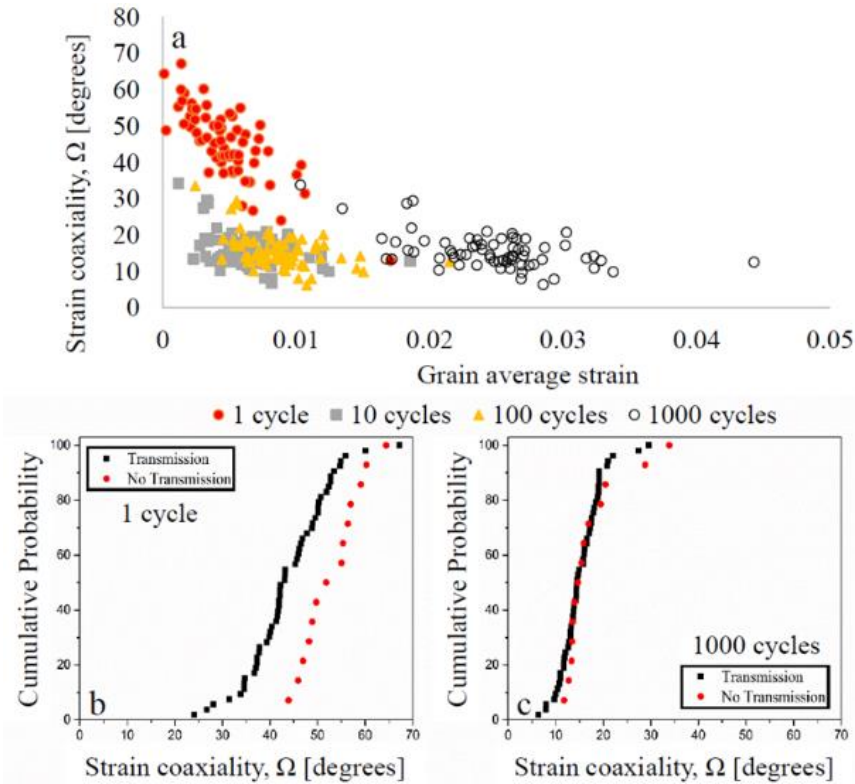
Figure 5.10: (a) The variation in the strain coaxiality angle as a function of the average strain in each grain. The cumulative probability plots display the average strain coaxiality angle of each grain based on whether slip transmission is observed in that grain following (b) 1 cycle and (c) 1000 cycles.

87

Local lattice rotations within a grain provide insight into the dislocation density and thus the amount of plasticity. Initially, the strain coaxiality is heterogeneous within each grain. Close examination of Figure 5.9 (a-b) and (e-f) show that slip bands are measured to have low strain coaxiality or are well aligned to the macroscopic deformation axis. Meanwhile, the regions between slip bands are highly misaligned relative to the macroscopic deformation axis. The early alignment of the in-plane strain along slip bands and the macroscopic applied loading axis is likely due to the dislocation motion along these slip bands to accommodate deformation. Following 10 through 1000 cycles of deformation, the area between slip bands begins to accumulate more strain and gradually become more aligned with the macroscopic deformation axis, as shown in Figure 5.2 (b-d) and (f-h) and Figure 5.9 (b-d) and (f-h), respectively. Two hypotheses exist for the gradual decrease in strain coaxiality of the regions between slip bands. First, microplasticity could develop in the regions between slip bands, in order to accommodate the additional, incompatible deformation along the slip bands during cyclic deformation. Second, grain rotation accompanies slip within a grain, as a means to satisfy the boundary conditions imposed on each grain for polycrystalline deformation. Lattice rotations have been directly measured and quantified as a consequence of large deformation, in an effort make the deformation across neighboring grains compatible [116].

To investigate the possibility of grain rotation, a comparative analysis, prior to loading and following 1000 cycles, was performed between the accumulated strain, strain coaxiality, and the change in crystal orientations, as measured by EBSD. Post-deformation EBSD, following 1000 cycles, was collected with identical resolution to the pre-deformation characterization. The change in crystal orientations between each EBSD data set were calculated spatially throughout the AOI and are referred to as the crystal misorientations. Following 1000 cycles, the axial strain component, Figure 5.11 (a) and (d), strain coaxiality, Figure 5.11 (b) and (e), and crystal misorientations, Figure 5.11 (c) and (f), are shown for each AOI, respectively. Magenta arrows highlight examples of one-to-one correlations between strain, strain coaxiality, and the change in crystal orientation during loading, where highly strained grains with low strain coaxiality values also correlated to grains with relatively large crystal misorientations. Further, white arrows highlight GB regions that display a large amount of localized misorientation, which do not always have a one-to-one correspondence with the in-plane strains and strain coaxiality values in the AOI. The observed homogeneity of the misorientation fields within each grain could indicate that

secondary slip systems may be activate, which could initiate microplasticity or subdomains of rotation between slip bands. This is still an open question and should be further investigated with coupled in-situ deformation experiments and EBSD data collection, as well as transmission electron microscopy.
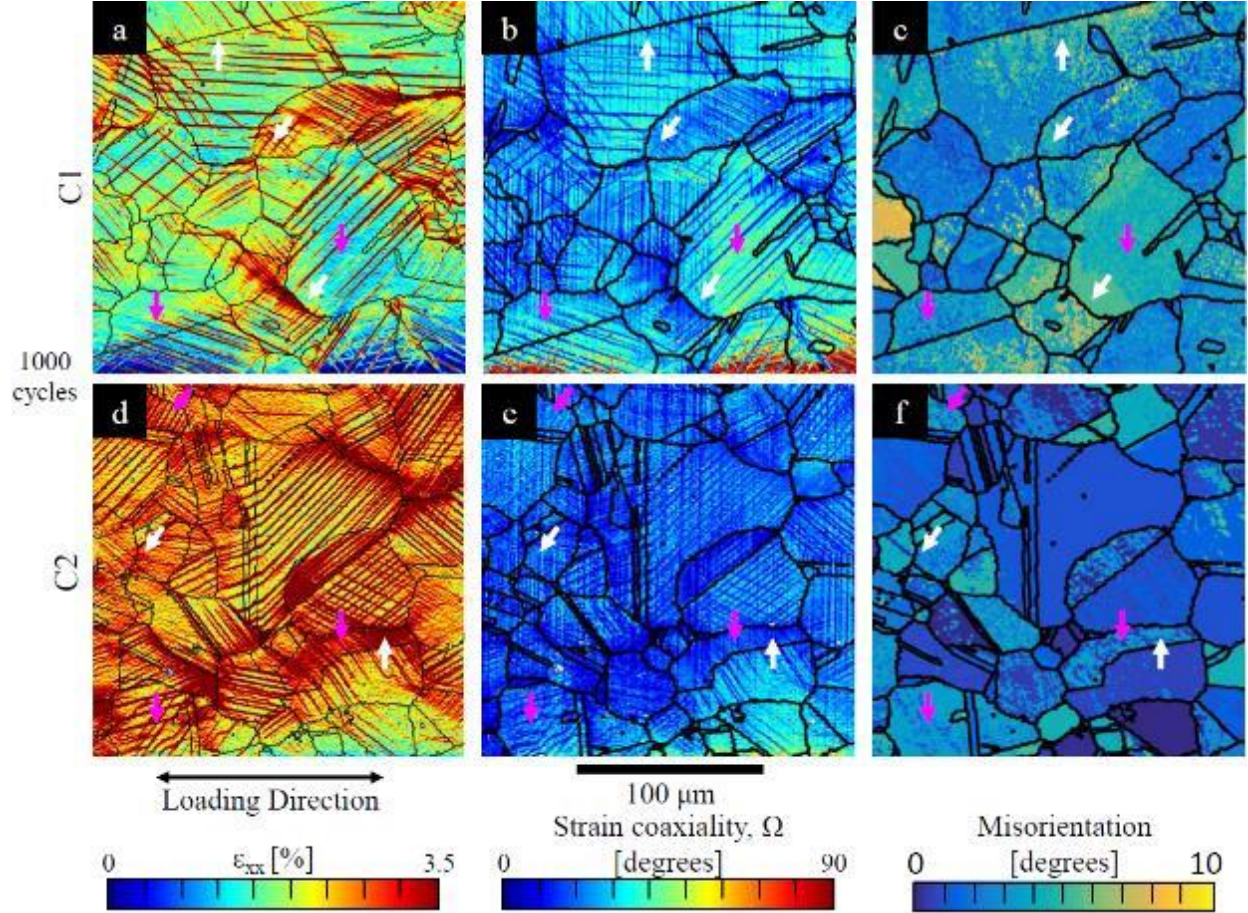
Figure 5.11: A side-by-side comparison of (a) and (d) the axial strain component, (b) and (e) strain coaxiality angle, and (c) and (f) misorientation angle between pre-deformed and post-deformed EBSD data, within microstructural variants C1 and C2, respectively. The magenta arrows indicate examples of one-to-one comparisons across data sets where large amounts of strain or low coaxiality angles correspond to regions of relatively large misorientations, while the white arrows highlight examples of large local misorientations at GBs.

5.5   Conclusions

The following conclusions regarding the effect of slip inter-connectivity between neighboring grains and strain localization were deduced from this work.

1. Slip band level resolution of strain is acquired through DIC. By incorporating the in-plane strain, local crystallographic information, and fcc yield locus, it is possible to identify the most likely active slip systems through a combination of theories originally proposed by Taylor [123] and Bishop and Hill [139]. The method to determine the active slip planes and slip direction was verified by identifying the crystallographic planes indicated by the slip bands observed via DIC and the in-plane displacement within the DIC slip bands, respectively.

2. From the identification of active slip systems, slip transmission was investigated. Geometric criteria were used to rationalize slip transmission, which compared well with existing theories. Cases of slip transmission were evaluated based on the accumulation of incremental slip within the incoming and outgoing slip bands. Two cases of slip transmission were chosen, one of high slip system alignment, $m' = 0.9997$, and one case of highly misoriented slip systems, $m' = 0.45$. High misorientation lead to a significant barrier for slip transmission, based on an accumulation of the incremental slip value along the incoming slip band, which could suggest a type of dislocation pile-up. A high amount of alignment provided a more constant value of incremental slip along the incoming and outgoing slip systems, at the GB, which could suggest a configuration that offers easier slip transmission.

3. From the slip events within the AOI, three categories of slip were identified:
   a. Slip confined to a single grain;
   b. Slip transmission, where a slip band extends between two neighboring grains; and
   c. Inter-connected bands, where slip extends through three or more adjacent grains.

   The shear strain increment along slip bands was consolidated using the incremental slip intensity, ISI, metric, and it was found that the degree of ISI increased with additional slip transmission. Accordingly, inter-connected bands, case 3 above, accumulated the highest degree of ISI and case 1, slip confined to a single grain, possessed the lowest degree of ISI. It should be noted that more disparity occurred in the ISI values, between the three aforementioned cases, with continued cycling.

4. Many inter-connected bands were oriented approximately 45° from the loading axis. The fact that these inter-connected bands produced the highest quantity of shear strain, as well as grain average strain, would suggest that multiple grains acting in concert are more prone to accumulate strain, thereby providing quantifiable evidence of the micromechanical fields that agree with existing theories and observations of crack initiation, such as the supergrain [16] or grain cluster [9] theories.

5. The strain coaxiality metric provided a comparison between the local in-plane strain state and the macroscopic applied strain. It was seen that the strain coaxiality values within slip bands were well aligned with the applied deformation axis, since the slip bands provide a plasticity mechanism to accommodate this deformation. More interesting, with increased applied loading cycles, the strain coaxiality values in regions between slip bands decreased, leading to an overall strain coaxiality decrease within each grain and the AOI. Grain rotation in polycrystalline materials is coupled with slip events and was quantified by comparing grain orientation information before and after loading cycles. One to one correlation was observed between crystal misorientations and in-plane strain values. These trends were not observed consistently throughout, which suggests that additional mechanisms may be active, such as microplasticity or subdomain rotation between the slip bands. Further, work is needed to identify potential grain reorientation relative to these slip bands.

6. THE ROLE OF GRAIN BOUNDARY MORPHOLOGY DURING ELEVATED TEMPERATURE DWELL-FATGIUE

6.1   Introduction

The need for higher temperature structural materials has driven efforts to tailor the microstructural features within Ni-based superalloys. As temperature and stress demands rise, additional deformation mechanisms, such GB sliding [60] and GB cavitation,[61] may become active. GB cavitation is a precursor to intergranular failure,[18] causing debits in elevated temperature dwell-fatigue life.[62] Since GB cavitation is recognized as a preceding mechanism to final fracture, identifying the microstructural configurations and micro-mechanical fields that promote GB cavitation are important to assess the high temperature material response of Ni-based superalloys. The research aim of Chapter 6 is to examine, the plastic strain accumulation occurring along the GBs with respect to the length fraction of GBs, which form cavities and the underlying precipitate structure. The specific analyses look to elucidate the propensity and evolution of GB cavitation within two distinct microstructures, during dwell fatigue loading at 700 °C within a vacuum environment, where HAGB morphologies have been tailored to be planar or serrated. A series of experiments utilizing DIC, EBSD, and SEM were utilized to characterize the strain localization preceding GB cavitation for serrated and planar GBs. As a consequence of their γ′ precipitate configuration, serrated GBs localized plastic strain resulting in cavity formation. Characterization of the underlying precipitate phase within each variant microstructure identified a larger distribution in the equivalent diameter and aspect ratio of the γ′ precipitates along serrated GBs or regions denuded of the γ′ phase. In the serrated GB structure, the variability in the γ′ precipitate structure created a wider distribution in local material strength and thereby was postulated to increase strain localization and subsequent GB cavitation in regions of lower local statistical strength.

6.2   Determination of active deformation mechanisms

The full field displacement data and SEM micrographs were utilized to assess GB sliding and cavitation. As a means of accounting for all in-plane plastic strain data, γ^{max} was calculated using Eq. 4.1[116]. The accumulated γ^{max} for each stress and microstructural condition are shown in Figs. 3 and 4. A majority of strain accumulation is observed to localize along slip bands and HAGBs. Table 3 summarizes the accumulated strain in each microstructural variant following loading.

Table 6.1: Average axial plastic strain and maximum shear strain within the serrated and planar specimens following 1 and 10 cycles.

	Axial Strain **(%)**			γ^{max} **(%)**		
Stress condition	LSA	HSA		LSA	HSA	
GB morphology	serrated	serrated	planar	serrated	serrated	planar
1 cycle	0. 12	0. 95	0.99	0.18	1.17	1.19
10 cycles	0. 22	1.42	3.25	0.28	1.47	3.18
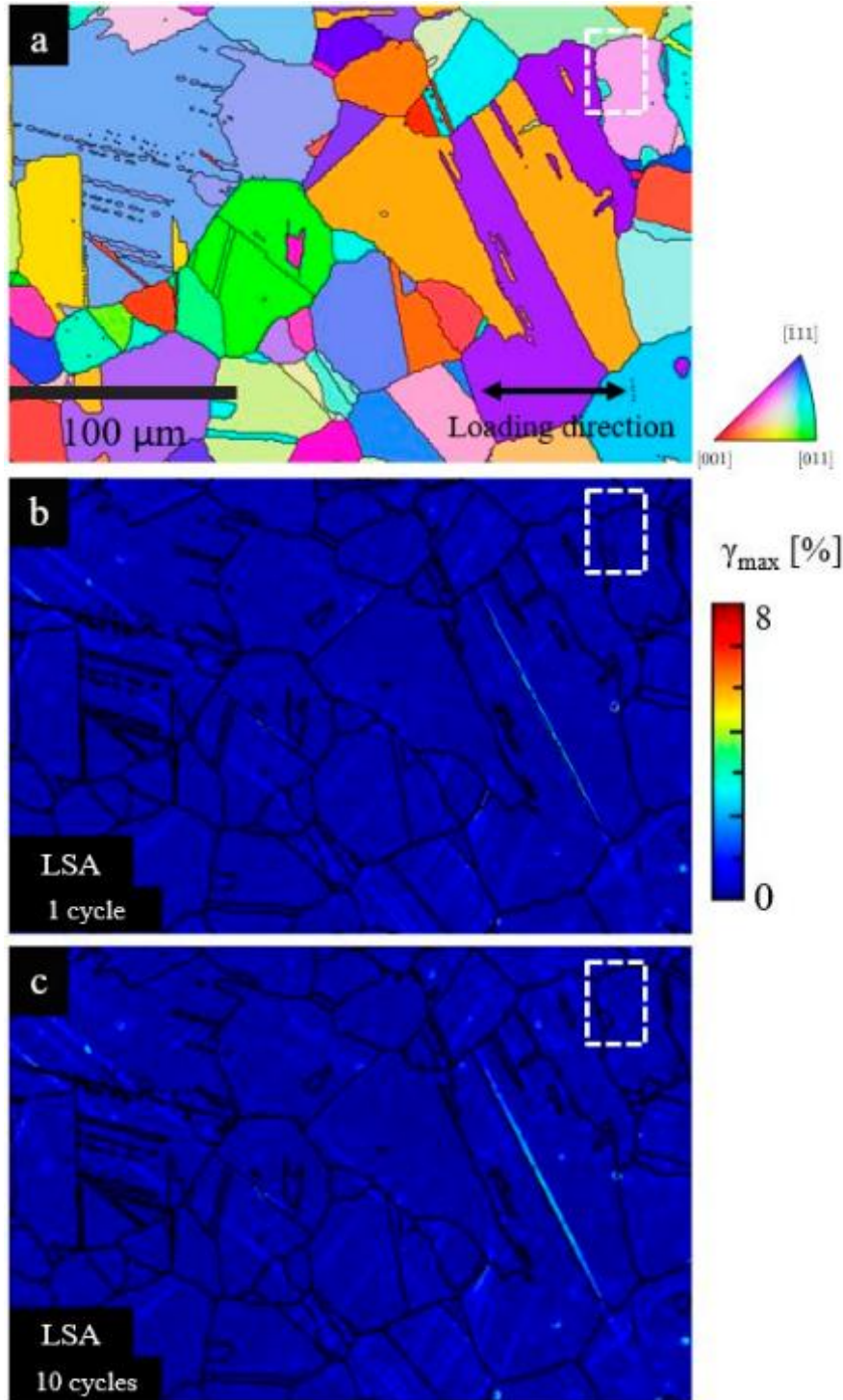
Figure 6.1: Inverse pole figure map of the region of interest (a). Maximum in-plane shear strain, γ^{max}, in the LSA serrated microstructure following (b) 1 and (c) 10 dwell-fatigue cycles. The boxed area is the region of interest of Figure 6.8.
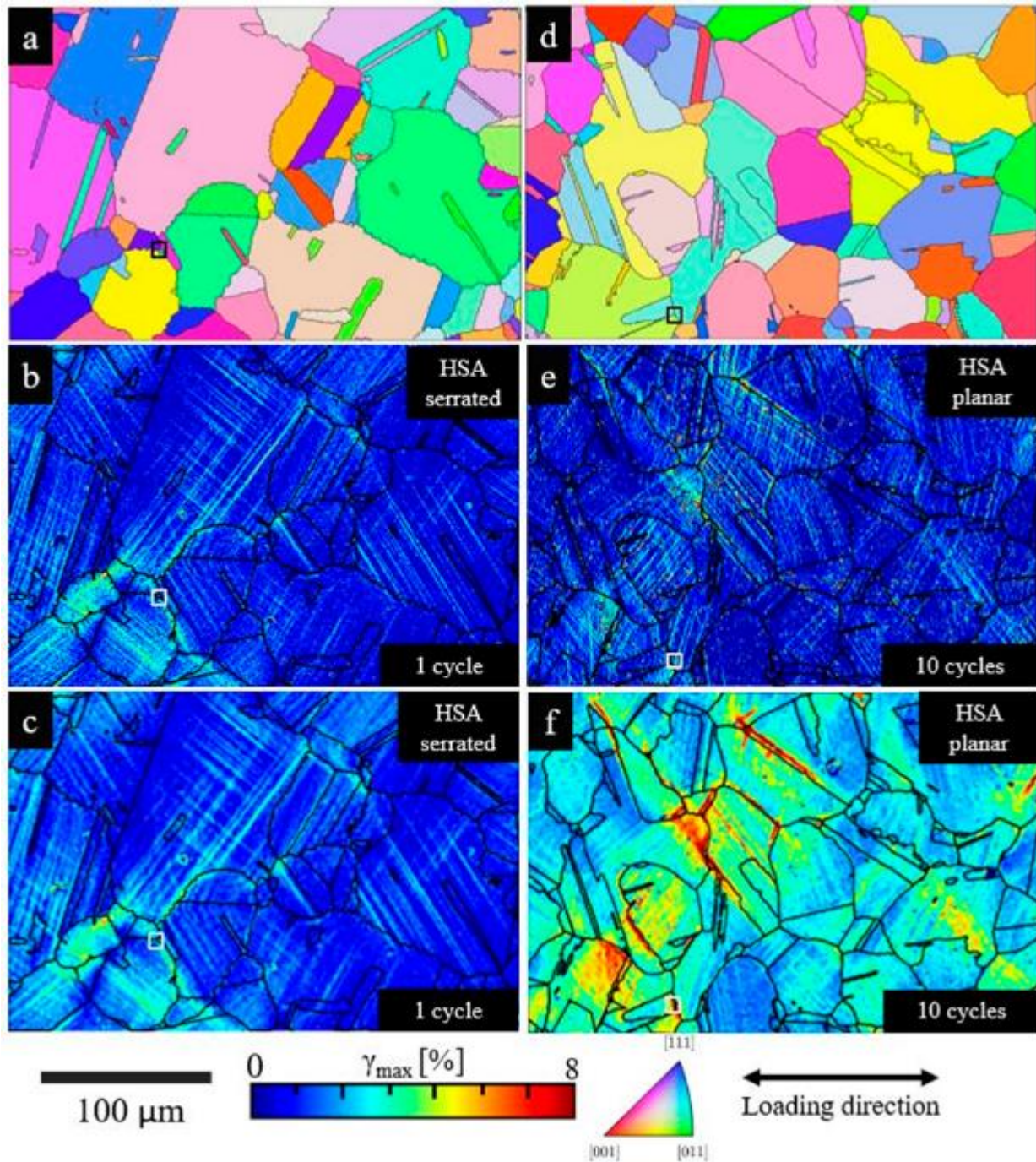
Figure 6.2: Inverse pole figure for the region of interest of the (a) serrated and (d) planar microstructures. Maximum in-plane shear strain, γ^{max}, in the (b,c) HSA serrated and (e,f) planar microstructures following 1 and 10 dwell-fatigue cycles. Boxed regions show the region of interest of Figs. 6 and 7.

95

The displacement gradients resolved parallel to the GBs were analyzed for all specimens to assess if the GB sliding mechanism was active during the experiment.[153] GB sliding was characterized by a sharp change in the displacement gradient that is confined to a small region around the GB. The magnitude of this gradient corresponds to the measured displacement within the GB plane. To compute the magnitude of the displacement at each GB, the EBSD orientation map was first segmented into grains, based on a misorientation threshold of 5°. The GB normal vector (n_x, n_y) and tangent vector (t_x, t_y) are calculated using the first order Cartesian moments of binary indicator functions, proposed in [154] and later adopted by Rovinelli et al.[155] The gradients in the resolved displacements were measured at three locations along the length of each GB. The displacements computed from high resolution DIC (u_x, u_y) were projected along the GBs using Eq. 6.1.

$$u_{resolved} = [u_x, u_y] \cdot [t_x, t_y]$$

<div align="right">Eq. 6.1</div>

The local changes in displacements must be isolated from the macroscopic displacements. For this, the mean macroscopic displacements for each GB were subtracted from the resolved displacement values, as shown in Eq. 3.

$$u'_{i_{resolved}} = u_{i_{resolved}} - mean\left(\sum_i u_{i_{resolved}}\right), \forall \text{ GB point i}$$

<div align="right">Eq. 6.2</div>

In Eq. 6.2, i ranges across all points for a given GB width. The gradient in the $u'_{resolved}$ across the GB was calculated to obtain the GB sliding magnitude. This algorithm has been verified in an earlier study to compute the GB sliding magnitudes in high temperature deformation of pure aluminum,[153] in which the calculated GB sliding magnitudes were validated by measuring discrete shifts in the deposited platinum fiducial lines at the GBs. Measured displacement magnitudes along the GBs are shown in Figure 6.3. A threshold displacement value of 0.1 μm was defined due the electron image resolution, which made confirmation of GB sliding at magnitudes lower than 0.1 μm unreliable. The GBs with the largest differences in the calculated displacements were examined via electron imaging for any visually detectable offset in the applied titanium speckle pattern. No evidence of GB sliding was detectable through inspection of the micrographs. Another methodology has previously been developed to capture the discrete nature of displacements utilizing a Heaviside function in tandem with the conventional high resolution DIC. [156]
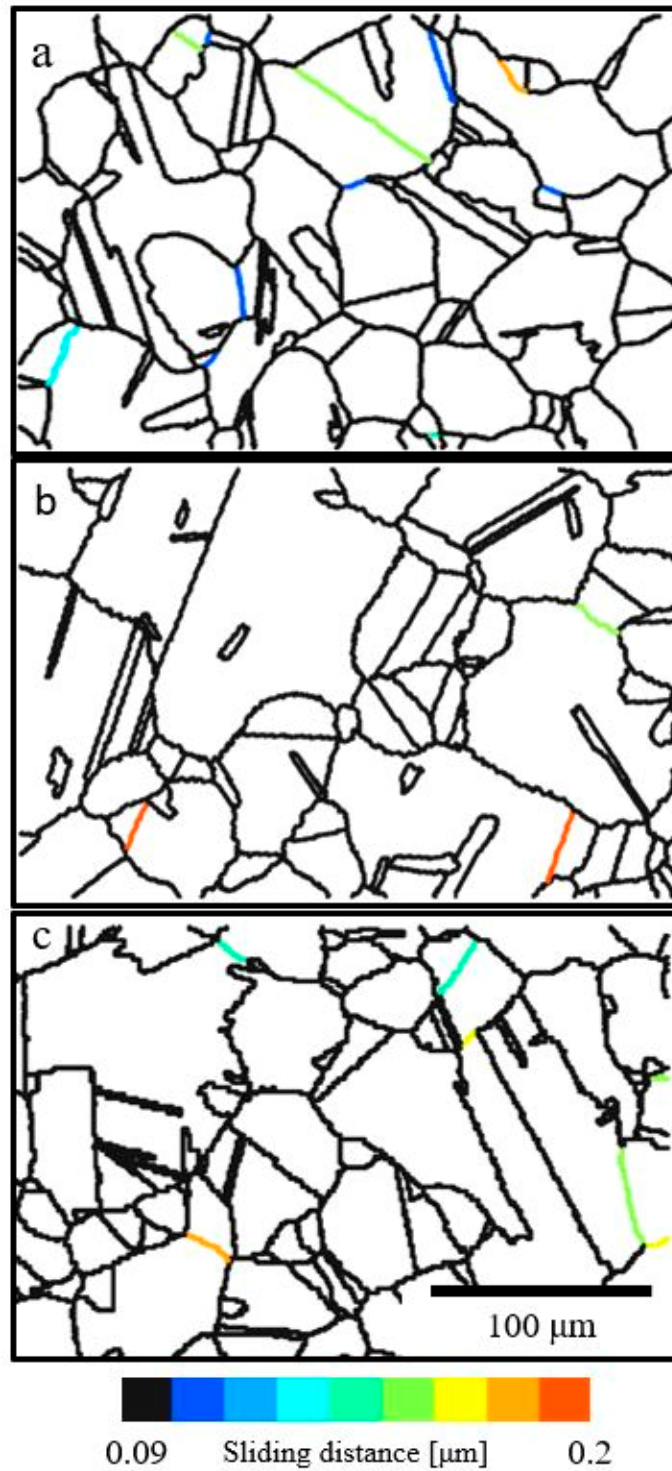
Figure 6.3: The calculated GB displacement distances are plotted for the (a) HSA planar, (b) HSA serrated, and (c) LSA serrated specimens. The GB displacement analysis was conducted by Ajey Venkataraman.

However, HAGBs in both microstructural variants experienced GB cavitation, as shown in Figure 6.4 and Figure 6.5. The evolutions of cavity formation within the planar specimen are shown within Figure 6.4(a-c), with the smaller boxed region of cavity formation examined in Figure 6.4(d-f). The inverse pole figure and high resolution DIC following 1 and 10 cycles of deformation are shown in Figure 6.4(g) and Figure 6.4(h,i), respectively. Both microstructural variants experience strain localization followed by strain accumulation at the GBs following 1 and 10 cycles of deformation, as shown in Figure 6.4(h,i) and Figure 6.5(h,i) for the planar and serrated microstructures, respectively. Following 1 cycle of deformation, no discrete cavities are observed between the arrows in Figure 6.4(b), while after 10 cycles, cavities had formed in locations of slip band impingement along the planar GB of interest, as shown between the arrows in Figure 6.4(c). An enlarged view of the cavity formation along the planar GB are shown within Figure 6.4(d-f). The planar variant explicitly shows cavity formation at the impingement of slip bands, which have been traced with dashed lines in Figure 6.4(e,f). Note the slip band impingement site is present following 1 cycle of deformation. With continued strain accumulation, a cavity forms at the slip band impingement location, as shown in Figure 6.4(f).

Within the serrated microstructure, cavities coalesced along HAGBs to form incipient cracks, as outlined by a dashed line in Figure 6.5(a-c) and enlarged in Figure 6.5(d-f). The formation and coalescence of cavities with applied deformation is captured when examining the serrated GB within Figure 6.5(d-f). Where discrete cavities become connected between 1 and 10 cycles, as shown by arrows in Figure 6.5(e,f). Qualitatively, smaller, more discrete cavities were present in the planar microstructure following deformation as compared to the serrated sample. Cavity formation was not observed along twin boundaries, thus further analysis is focused along HAGBs. The length fraction of HAGBs that formed cavities within each AOI is reported in Figure 6.6. It is seen here that compared to the planar microstructure, twice the length fraction of serrated HAGBs experienced cavitation during HSA loading. The cavity length fraction was determined by visually comparing each HAGB following 1 and 10 dwell-fatigue cycles, using electron micrographs. A GB was counted to be cavitated when the post-deformation image contained observable voids or gaps at the GB interface relative to the pre-deformed image.
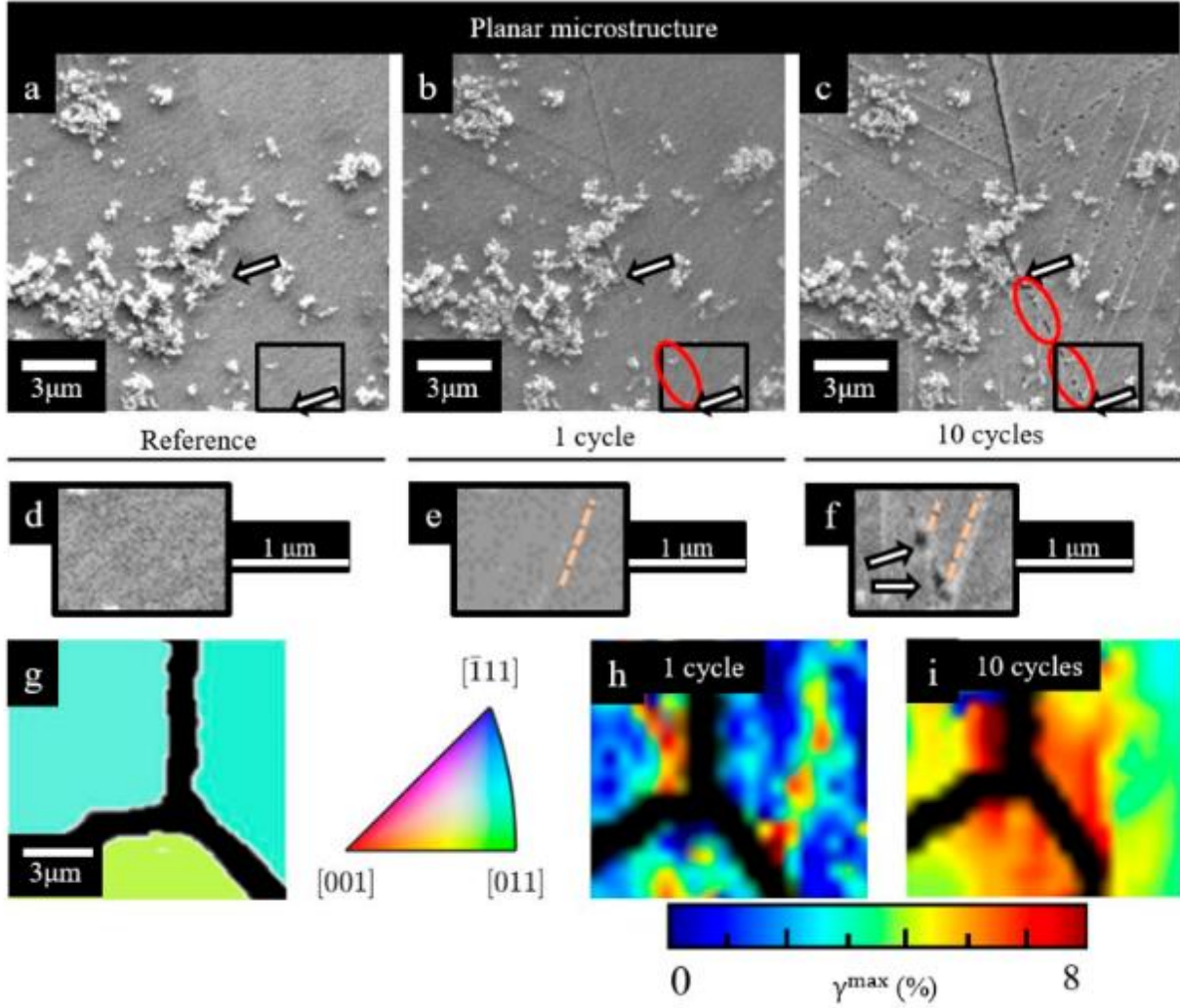
Figure 6.4: (a-c) Cavity formation evolution from the reference state and following 1 and 10 cycles in the HSA planar microstructure. Arrows are used to highlight the GB locations. Circles emphasize examples of cavity formation. A boxed region of interest is examined, where the evolution of the cavity formation with accumulated deformation is shown, corresponding to the (d) reference, (e) 1 cycle, and (f) 10 cycles of deformation. (g) An inverse pole figure map for the presented area of interest. High resolution DIC results within the AOI for (h) 1 cycle and (i) 10 cycles of deformation.
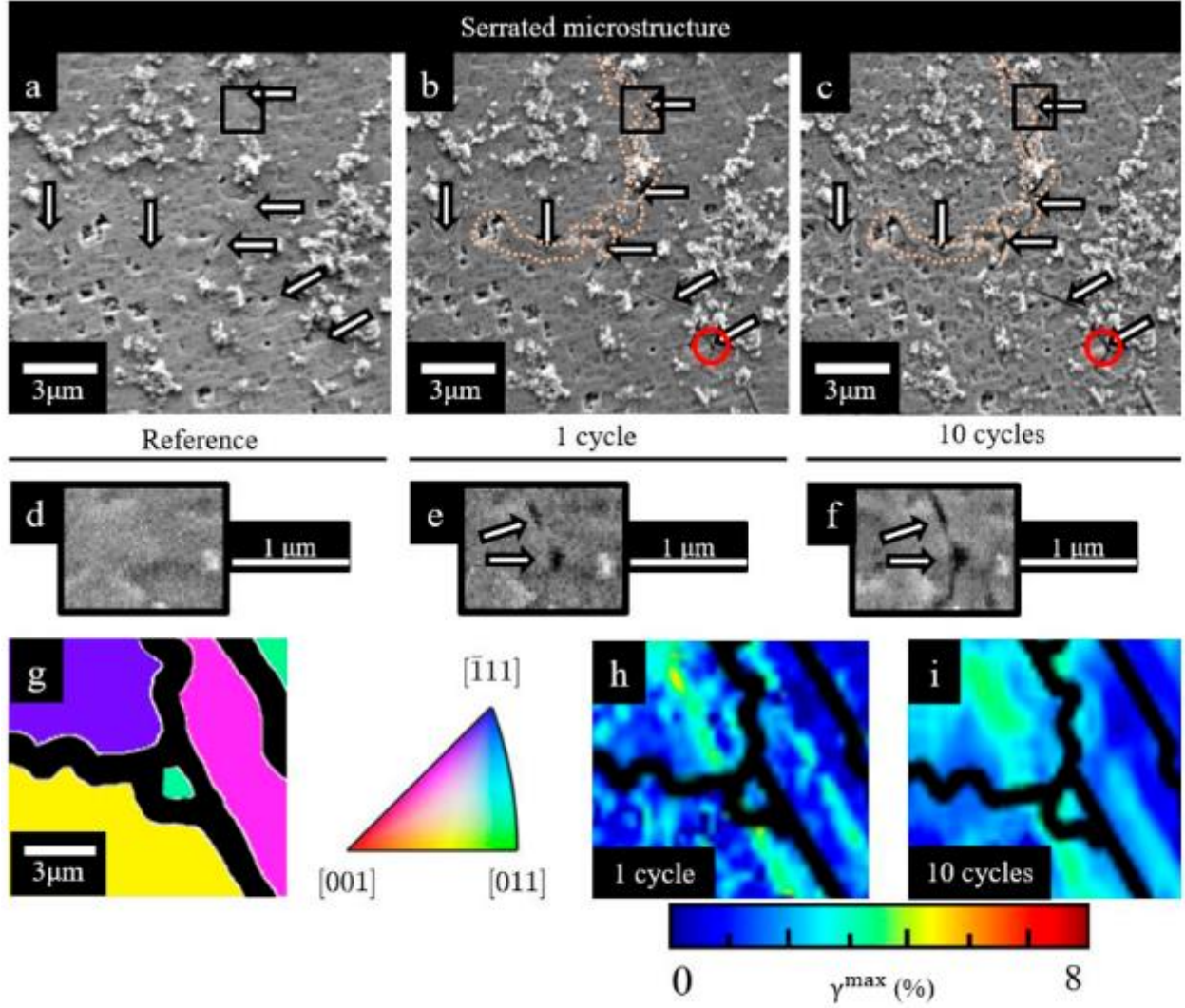
Figure 6.5: Cavity formation evolution from the reference state and following 1 and 10 cycles in the HSA (a-c) serrated microstructure. Arrows are used to highlight the GB locations. Circles emphasize examples of cavity formation. A boxed region of interest is examined, where the evolution of cavity formation with accumulated deformation is shown, corresponding to the (d) reference, (e) 1 cycle and (f) 10 cycles of deformation. Encircled are locations of cavity formation along the serrated. An (g) inverse pole figure map for the presented area of interest. High resolution DIC results within the AOI for (h) 1 cycle and (i) 10 cycles of deformation.
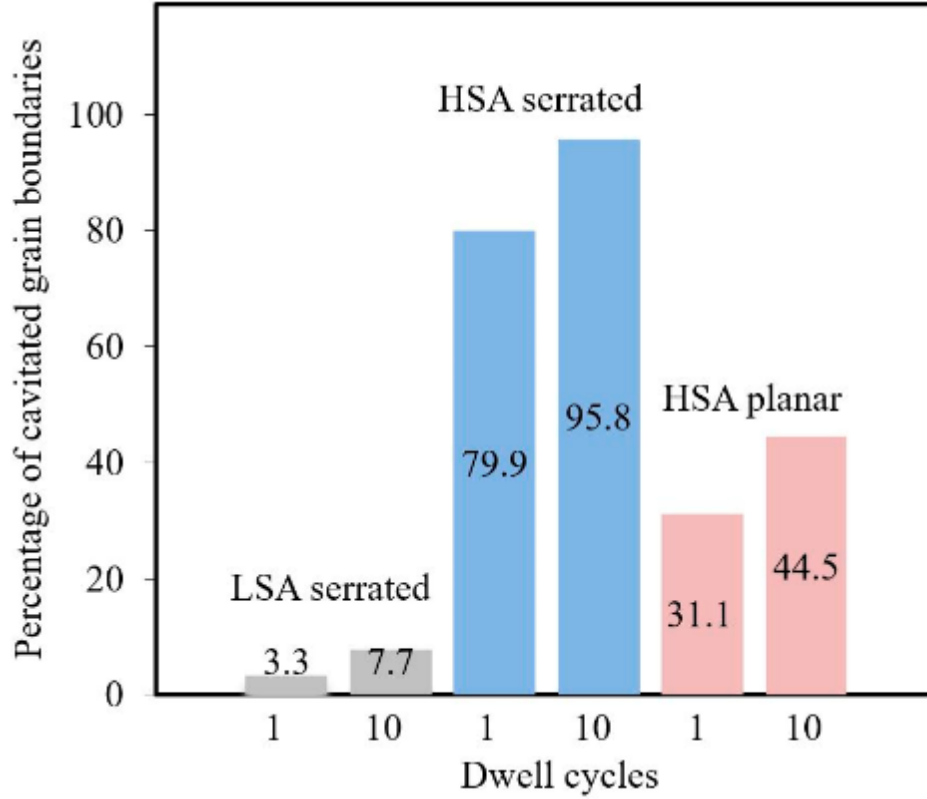
Figure 6.6: Length fraction of cavitated GBs following dwell-fatigue cycling at 1 cycle and 10 cycles.

6.3 Results

6.3.1 Strain localization and cavitation

The principal results of this study are comprised of the localization of strain relative to HAGBs that form cavities and the underlying γ′ precipitate configurations which promoted serrated-induced cavity formation. Cavity formation and coalescence were observed to occur along HAGBs in both microstructural variants, but more severely in the serrated microstructure. Cavity formation in the previously introduced model [75] was predicated by the cumulative plastic deformation causing cavity formation to occur, thus the plastic strain state along the HAGBs are analyzed utilizing the γ^{max}. The γ^{max} were extracted along the HAGBs using a width of 1.6 μm in all AOIs. The width of the extracted γ^{max} corresponded to twice the amplitude of an average serration, as measured from the serrated specimen's AOI. GBs were separated into two categories, (i) those that formed cavities following 10 cycles, and (ii) those that did not form cavities. The

extracted γ_{max} are shown for each variant and loading condition in Figure 6.7. Following 1 HSA dwell cycle, GBs which formed cavities measured, on average, larger γ^{max} values and displayed strain values at least twice as large within their upper tails as compared to the non-cavity forming GBs. Following 10 HSA dwell cycles, larger plastic strain accumulations are consistently measured along all GBs which formed cavities.
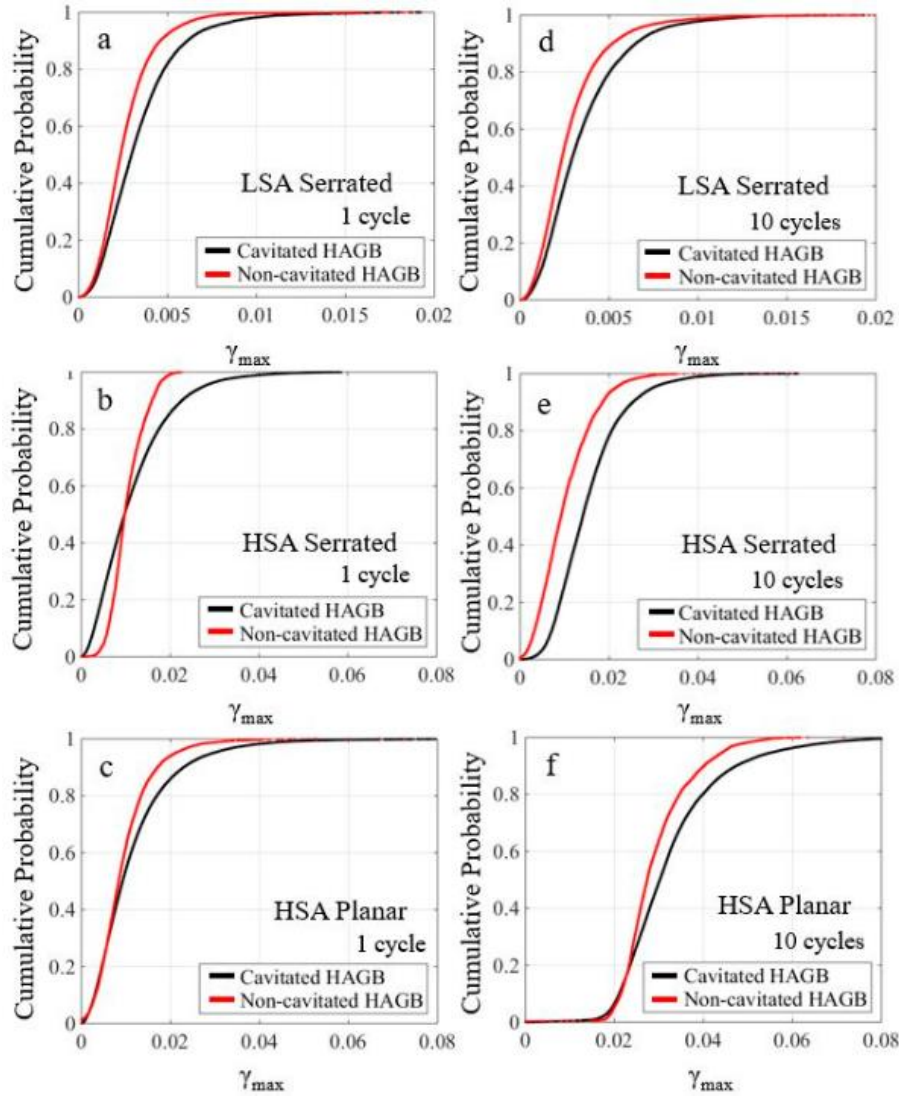
Figure 6.7: Maximum in-plane shear strain, γ_{max}, measured at high angles GBs in the (a,d) LSA serrated specimen, (b,e) HSA serrated specimen, (c,f) HSA planar specimen, at 1 and 10 cycles, respectively.

Due to the relatively lower stresses applied to the LSA serrated specimen, a small fraction of HAGBs experienced cavity formation. Initial regions of cavity formation were identified to correspond with regions that contained coarsened γ' or were denuded of the γ' phase, as shown in Figure 6.8(a-c). An evolution of the cavity formation for specific locations coinciding with coarse γ' precipitates and locations that are denuded of γ' precipitates are shown in Figure 6.8(d-f). Regions of coarse γ' and areas denuded of γ' phase were identified via BSE imaging, as shown in Figure 6.8(g). These γ' precipitate configurations localized plastic strain accumulation within the serrated microstructure, as shown in Figure 6.8(h,i), following 1 and 10 dwell cycles, respectively.
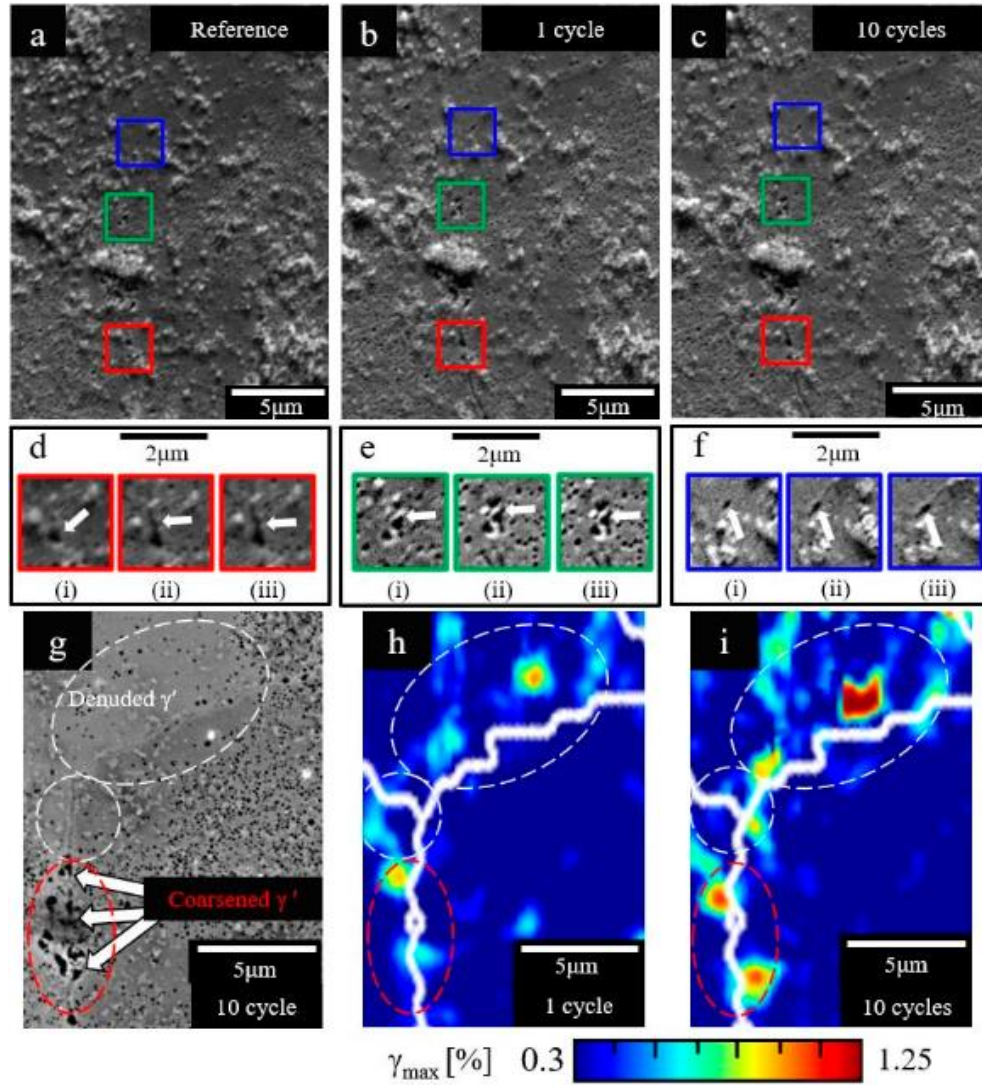
Figure 6.8: Electron images showing the cyclic evolution of cavitation in the LSA serrated specimen (a-c) at a reference state, 1 and 10 cycles. Specific regions of interest are outlined which correspond to locations along the GB where cavity formation occurred at γ' precipitates during deformation. These (d-f) regions of interest are examined following (i) reference, (ii) 1 cycle, and (iii) 10 cycles of deformation. (g) A backscattered electron image highlights regions that are denuded of γ' or contain coarse γ' precipitates. Maximum in-plane shear strain, γ_{max}, accumulation following (h) 1 and (i) 10 dwell-fatigue cycles.

6.3.2 γ′ characterization

Metallographic specimens were prepared utilizing the standard mechanical grinding steps, as described above. The final polishing was achieved utilizing a two-step process, 0.04 µm colloidal silica for 15 minutes followed by electro-chemical etching in 10% phosphoric acid at 2-2.5 V. This procedure dissolves the γ matrix to reveal the γ′ precipitates. The characterization of the γ′ precipitates were conducted on a Zeiss Sigma FEG-SEM utilizing a through-the-lens backscatter detector, at 10 keV with a 3-4 mm working distances. The use of back-scatter electron imaging maximizes the contrast variation between the two phases and allowed for automated image thresholding methods to be more readily used to improve accuracy.

The equivalent circular diameter and aspect ratio of the γ′ precipitates were characterized for each variant microstructure through an automated segmentation of SEM micrographs using open source software ImageJ [99]. The precipitate segmentation process consisted of four steps. First the precipitates are separated from the matrix via an automated grayscale threshold. Next, the image is binarized resulting in precipitates displayed as black and the matrix displayed as white. Any holes created within the segmented precipitates from thresholding are then filled to allow for more accurate particle area calculation. It should be noted that particle splitting processes were not used in the current investigation due to the likelihood of erroneous separation and inaccurate precipitate area of the non-spherical morphologies in the slower cooled samples. Lastly, the analyze particle function within ImageJ was used to generate values for area, from which equivalent circle diameter was calculated, and aspect ratio from a minimum of three images acquired from three independent locations in each sample.[99]. A lower bound in the equivalent circular diameter was set at 30 nm, due to the limitations in reliable particle segmentation.

The underlying γ′ precipitates were categorized based on their spatial relationship to the HAGBs; (i) γ′ precipitates located along the GB or (ii) γ′ precipitates located within the bulk of the grain. Only precipitates that were directly adjacent to the GB were considered to be a part of (i). The planar microstructure contained a dense and even distribution of the γ′ precipitates regardless of their spatial location relative to the GBs, as shown in Figure 6.9(a-c). Due to the sub-solvus heat treatment, periodic coarsened γ′ precipitates were observed within an otherwise homogenous field of fine γ′ precipitates, throughout the planar microstructure as shown in Figure 6.9b. The serrated microstructure contained coarse and elongated γ′ particles directly adjacent to the GBs and smaller, more homogenously shaped γ′ precipitates within the bulk of the grain, as shown in Figure 6.9(d-

f). The γ′ precipitate equivalent circular diameter and aspect ratio cumulative distribution plots (shown in Figure 6.10) were created based off 12,000+ measurements. Larger aspect ratio and equivalent diameter γ′ precipitates were measured along the HAGB within the serrated microstructure, relative to the planar microstructure. The γ′ precipitate equivalent circular diameter within the bulk of the serrated microstructure was larger as compared to the planar microstructure. Negligible differences in γ′ precipitate aspect ratio were measured within the bulk of the grain when comparing the serrated and planar microstructures. Carbide precipitates formed within both material variants. These carbides were randomly dispersed and displayed no preference to form along the GBs, thus the cavitation analysis focused solely on the γ′ precipitates.
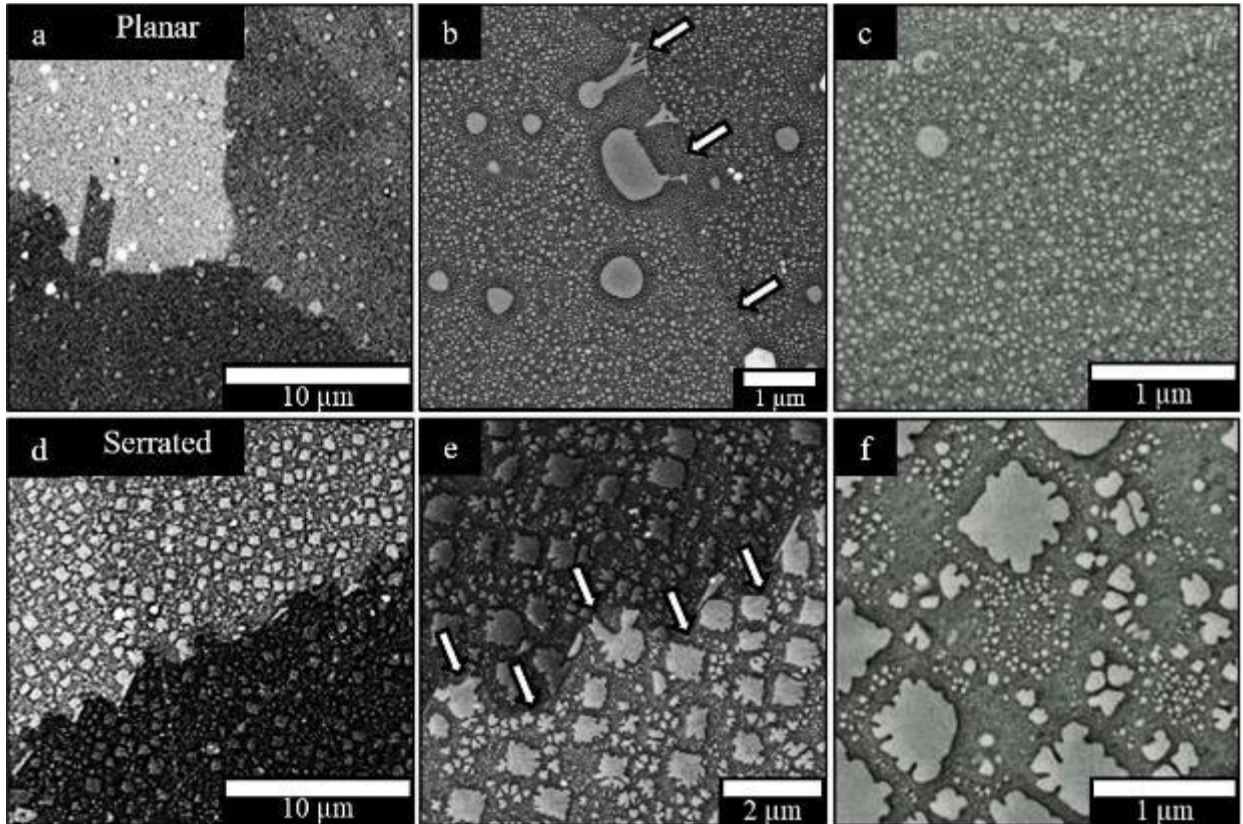
Figure 6.9: Secondary electron images of the γ′ phase in the (a-c) planar and (d-f) serrated microstructures. Low magnifications of the planar and serrated microstructures are shown in (a) and (d), respectively. White arrows highlight GB locations. High magnification of a typical HAGB in the planar and serrated microstructures are shown in (b) and (e), respectively. The precipitate structures within the bulk of a grain in the planar and serrated microstructures are shown in (c) and (f), respectively. The micrographs contained within this figure were captured by Ross Buckingham.
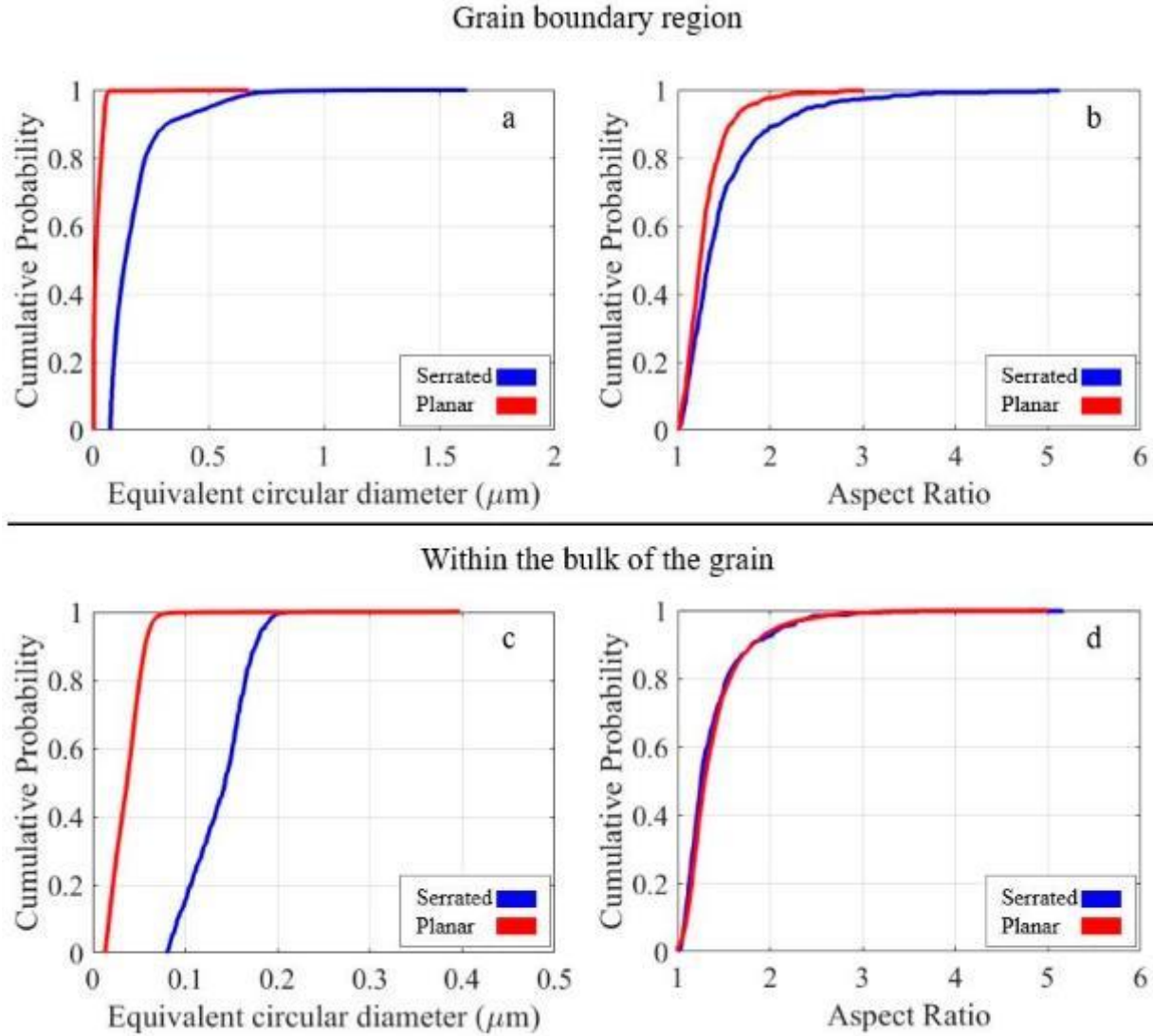
Figure 6.10: Comparison of the aspect ratio and equivalent circular diameter of the γ′ precipitates along the GB region (top), and within the bulk (bottom) within the in serrated and planar microstructures.

6.4 Discussion

The propensity of GB cavitation observed was related to the HAGB morphology, specifically the configuration of the γ′ precipitates, which dictated the degree of strain localization. Previously, Carter et al. [60] studied creep deformation of Ni-based superalloy Rene 104 with serrated and planar GBs under elevated temperature creep conditions. The strain accumulation observations in this study agree with Carter et al., wherein the planar microstructure localized strain along twin boundaries, and the serrated microstructure showed no preference to localize

deformation. Carter et al. noted the presences of cavities along planar GBs that experienced GB sliding, while similar cavity structures were observed in this study, no GB sliding was observed. Both the strain localization and γ' formation kinetics and their relation to cavity formation will be discussed.

In the LSA condition, strain localization was observed to coincide spatially with regions of coarsened γ' and regions denuded of the γ' phase, as shown in Figure 6.8(d-f). These regions localized approximately 1.25% γ^{max} or greater, compared to the full field average γ^{max} of 0.12% and 0.22%, following 1 and 10 cycles, respectively. Following the HSA dwell-fatigue loading, larger strain accumulations were consistently measured along HAGBs, which experienced cavitation. Serrated GBs measured, on average, strains which were 55% larger along HAGBs that formed cavities, as compared to those that did not. Comparatively, the cavity forming HAGBs within the planar microstructure only displayed a 10%, on average, higher accumulation of plastic strain. Li et al. [18] observed slower crack growth rates in RR1000 containing serrated GBs during elevated temperature dwell-fatigue experiments.

They proposed that more stress relaxation occurred at the crack tip of serrated GB microstructures, due to the relatively larger spacing between γ' precipitates, lowering the local driving force for crack propagation. The increased accumulated strain near the GB serrations can provide the mechanism for stress relaxation in these regions. Further, large stresses have been identified along serrated GBs [17,83] utilizing high resolution EBSD, which can be a driving force to promote the increased plastic strain localization and enhanced GB cavitation along serrated GBs, as observed in this study.

The kinetics of secondary phase formation played a key role in the development of the γ' precipitate structures examined in these microstructural variants. While cooling from a solution temperature, heterogeneous nucleation of the γ' phase occurs initially near GBs; where the energy required to nucleate a precipitate is decreased, diffusion rates are faster and strong solute atom segregation exists. The preference for a γ' phase to form and grow along a GB in RR1000 is shown in a systematic cooling study by Qiu and Andrews,[157] where γ' precipitates at the GBs reached approximately 1 µm before the interior particles grew to 100 nm in the same time period. Once nucleated, the γ' precipitates will grow if the surrounding chemical species can diffuse to the interface of the precipitate. Following the final heat treatment step, the serrated microstructure was cooled at a slower rate, relative to the planar microstructure, allowing for increased time to be

spent at elevated temperatures, where diffusion rates are greater. These conditions allowed for continual coarsening and elongation of the γ′ precipitates along the GBs. The coarsened γ′ precipitates also caused the surrounding matrix material to become devoid of the chemical species required to nucleate the γ′ precipitates, reducing the precipitate strengthening effects and thus reducing the local strength along the GB regions. Areas containing coarsened γ′ or which were denuded of γ′ phase, are observed to be areas of initial cavity formation. For this reason, a large area, 1 mm by 1 mm, was investigated with BSE imaging, such that the γ′ precipitates were visible. A typical serrated GB contained coarse γ′ precipitates and/or was denuded of the γ′ phase completely, as shown in Figure 6.11. The local distribution in strength predisposed these locations to strain accumulation.
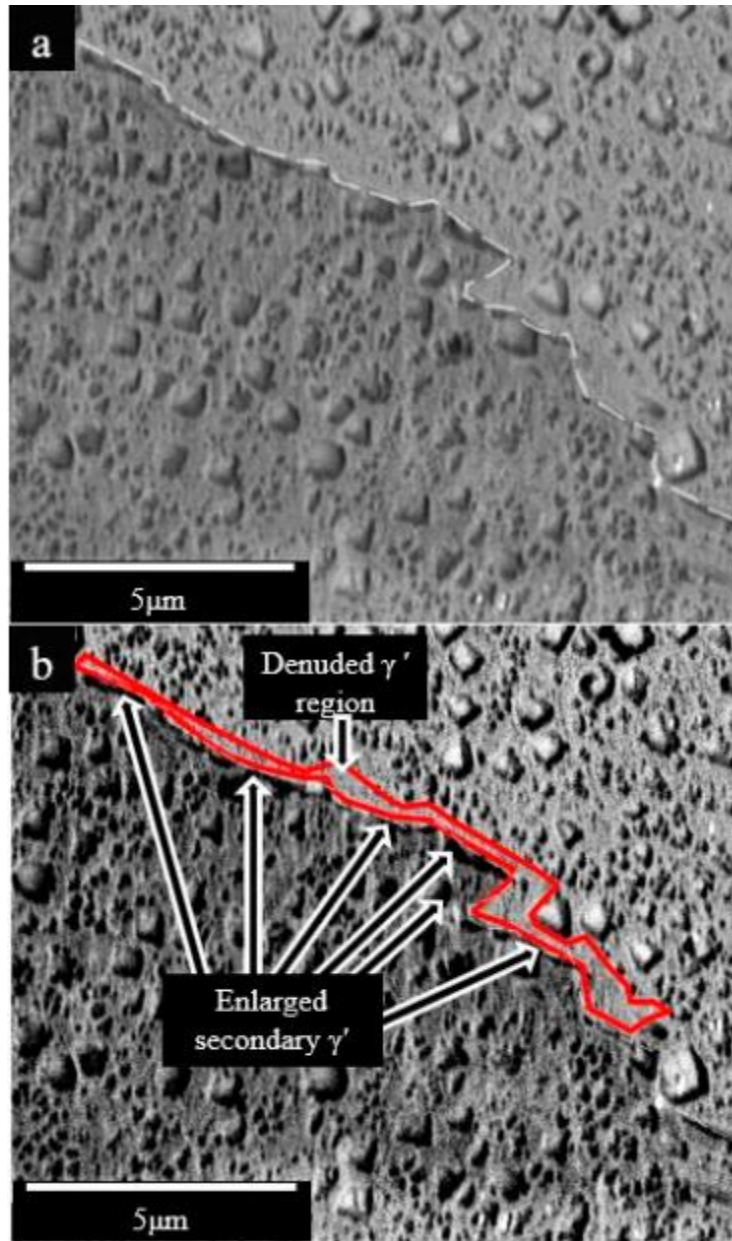
Figure 6.11: (a) Backscattered electron image of a GB in the serrated microstructure. The GB is emphasized by dashed line. (b) A modified BSE image highlighting examples of the enlarged secondary γ′ precipitates and the adjacent denuded γ′ region along the GB. Arrows highlight regions where the γ′ phase is absent along this GB.

The circumstances leading to the increased cavity formation in serrated GBs is summarized schematically in Figure 6.12. Regions which contained coarsened γ′ and/or are denuded of the γ′ phase, create locally weaker regions along serrated GBs, as shown in Figure 6.12a. The absence of the γ′ phase across regions along the GB created a distribution in local strength, which localized

deformation and plastic strain accumulation, as shown in Figure 6.12b. These local neighborhoods promoted cavity formation as a means to accommodate the plastic strain and cavities extended along the GB interface, initiating cavity coalesce, as shown in Figure 6.12c. The localization of plastic strain may increase the local stresses [29] and thereby activate secondary slip or slip activity in an adjacent grain [129,130], thus promoting further cavity formation along the GBs.
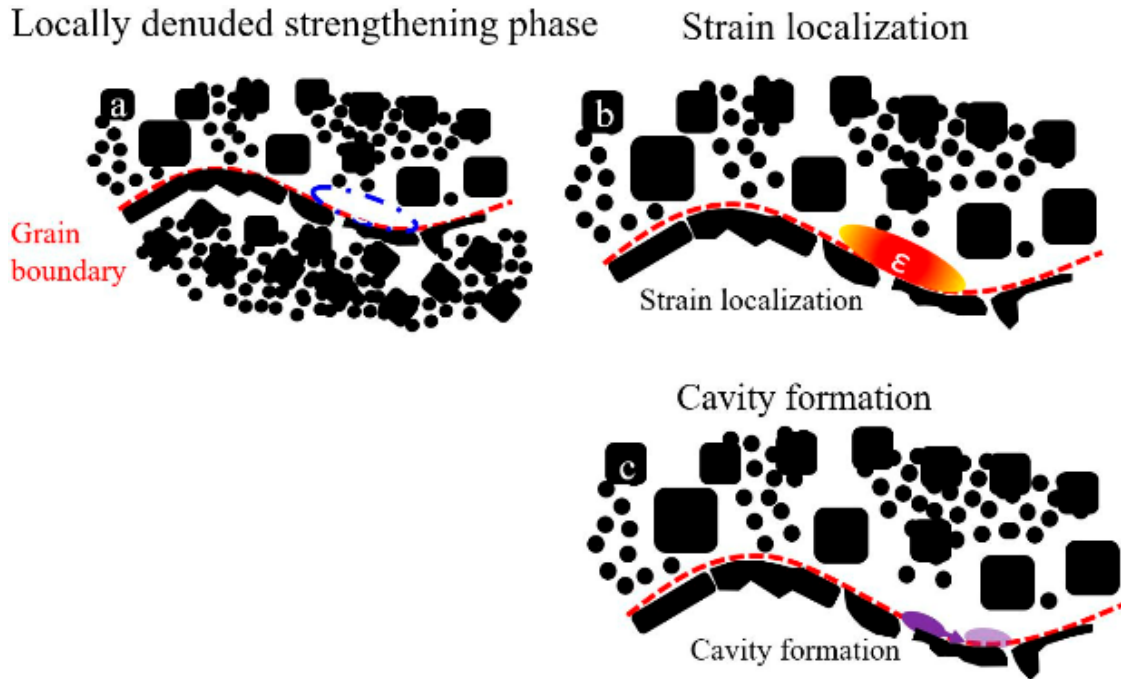
Figure 6.12: (a) γ′ precipitates along a GB, wherein an area is denuded of the γ′ phase entirely. (b) Strain localization occurs within the area denuded of the γ′ precipitates. (c) Subsequent, cavity formation and coalesce occurs.

In this study, the cooling rate is purposely lower than the values used in traditional superalloys to exacerbate the formation of the GB serrations. Due to the large GB serrations and associated differences in the γ′ distributions, the serrated GB variant sample exhibited lower strength than the variant with planar GBs and was more prone to cavity formation at lower temperatures than previously reported for RR1000. Larger GB serrations with similar periodicity have been reported in RR1000 following cooling rates of $0.7 \frac{°C}{s}$ from an initial solution temperature by Mitchell et al. [19] The larger serrations can likely be attributed to an additional 16-hour aging treatment performed at 760 °C, which caused the secondary γ′ precipitates to enlarge, increasing the magnitude of the GB serrations.

6.5   Conclusions

The following conclusions regarding cavity formation along serrated and planar GBs within a Ni-based superalloy, RR1000, were deduced from this work.

1. The predominantly active deformation mechanisms, under the current experimental loading conditions, were crystallographic slip and GB cavitation. The GB sliding magnitudes were quantified and found to be non-significant within this study.

2. Twice the length fraction of GB cavities was observed to form in the HSA serrated microstructure following each sequence of dwell-fatigue loading, as compared to the HSA planar GB specimen.

3. Plastic strain accumulations were more heterogeneous along HAGB in the serrated microstructure. Strain accumulations were, on average, 55% greater along serrated HAGBs which formed cavities versus those that did not form cavities, compared to only a 10% difference in the like comparison of planar GBs.

4. The serrated GB variant contained both higher aspect ratio and larger γ' precipitates along the GBs, while maintaining an equivalent aspect ratio of the γ' phase within the bulk of a grain, as compared to the planar GB variant. The increased coarsening observed in the γ' phase agrees with the expected precipitation kinetics, wherein the decreased energy barrier near interfaces leads to discontinuous precipitation of secondary phases and additional time at higher temperatures results in a coarser precipitate structure.

5. Initial cavity formation was observed during LSA dwell-fatigue, along serrated GBs which contained coarse γ' and was denuded of the γ' phase. This GB also experienced strain localizations 5 to 10 times larger than the average AOI strain.

6. Regions of coarsened and/or denuded γ' are expected to exhibit a lower statistical strength. These regions localize deformation, resulting in GB cavity formation. Accumulation of plastic strain intensified with continued deformation causing cavities to grow and coalesce along GBs.

7. CONCLUSIONS AND FUTURE WORK

The objective of this research was to examine the effect of microstructural features on the development of plastic strain within a model and engineering material. First, the effects of microstructural features and their ability to affect the primary direction of the deformation pathways was investigated. Second, the additional degree of plastic strain accumulation was investigated for grain clusters relative to single grains and grain pairs. Lastly, cavity formation during elevated temperature dwell-fatigue on GBs with serrated and planar morphologies was examined. Each objective was addressed in the aforementioned chapters and the contributions are presented below.

In Chapter 4, the role of microstructural features in establishing the pathways of deformation, regardless of loading condition was performed utilizing Ti7Al, a titanium alloy. A series of multiaxial deformation experiments were conducted, wherein DB formation was examined over the mesoscale. A three-step process of strain thresholding, data percolation and skeletonization defined the location DBs, which spanned many grains. The DB's mean orientation, as well as any local angular deviations, were assessed for all loading conditions and percolation strains. The DB statistics were then utilized to explore the number of DBs needed to minimize the overall mechanical error of a RVE and were compared with RVE values from literature.

It was found that DBs which formed parallel to the plane of MSS were longest and carried the largest degree of deformation. The spatial distribution of DBs was influenced by grain size, as they formed in grains there were, on average, 1.6 times larger than the average grain size. Smaller DBs, in both length and degree of deformation, formed an inter-connected network to maintain compatibility within the specimens. These inter-connected DBs were more susceptible to deviations from the plane of MSS. These deviations occurred near GBs. The largest strain accumulations within DBs were observed to occur near GBs. Both the macroscopic residual deformation and underlying DBs were used in tandem to describe a mesoscopic RVE edge length that could capture the overall deformation response as well as the population of the DBs within the RVE. The overall mechanical error is minimized when the RVE edge length is $1610\,\mu m$, which encompassed an average of 446 grains and 18 DBs for all three percolation strains. As the RVE became smaller, the mechanical response no longer matched the global response of the specimen, due to an exponential increase in the overall mechanical error. In order to capture well defined DB

features within an RVE, this 2D analysis recommends 18.7 grains per RVE edge length, which is significantly more than previous studies in the literature utilizing a similar material.

In Chapter 5, the effect of slip inter-connectivity between neighboring grains and strain localization was studied using a combination of DIC, EBSD, and calculated incremental slip in a Ni-based superalloy, RR1000. The presented results provide quantified evidence that grains containing inter-connected slip bands are locations of strain localization and consequently possible sites of crack initiation.

By incorporating the in-plane strain, local crystallographic information, and fcc yield locus, it was possible to identify the most likely active slip systems through a combination of theories originally proposed by Taylor [123] and Bishop and Hill [139]. The method to determine the active slip planes and slip direction was verified by identifying the crystallographic planes indicated by the slip bands observed via DIC and the in-plane displacements within the DIC slip bands, respectively. From the identification of active slip systems, slip transmission was investigated. Geometric criteria were used to rationalize slip transmission, which compared well with existing theories. Cases of slip transmission were evaluated based on the accumulation of incremental slip within the incoming and outgoing slip bands. Two cases of slip transmission were chosen, one of high slip system alignment, $m' = 0.9997$, and one case of highly misoriented slip systems, $m' = 0.45$. High misorientation lead to a significant barrier for slip transmission, based on an accumulation of the incremental slip value along the incoming slip band, which could suggest a type of dislocation pile-up. A high amount of alignment provided a more constant value of incremental slip along the incoming and outgoing slip systems, at the GB, which could suggest a configuration that offers easier slip transmission. From the slip events within the AOI, three categories of slip were identified:

1. Slip confined to a single grain;
2. Slip transmission, where a slip band extended between two neighboring grains; and
3. Inter-connected bands, where a slip band extended through three or more adjacent grains.

The shear strain increment along slip bands was consolidated using the incremental slip intensity, ISI, metric. The magnitude of ISI increased with additional slip transmission. Accordingly, inter-connected bands, case 3 above, accumulated the highest degree of ISI and case 1, slip confined to a single grain, possessed the lowest degree of ISI. It should be noted that more

disparity occurred in the ISI values, between the three aforementioned cases, with continued cycling.

Many inter-connected bands were oriented approximately 45° from the loading axis. The fact that these inter-connected bands produced the highest quantity of shear strain, as well as grain average strain, would suggest that multiple grains acting in concert are more prone to accumulate strain, thereby providing quantifiable evidence of the micromechanical fields that agree with existing theories and observations of crack initiation, such as the supergrain [16] or grain cluster [9] theories.

The strain coaxiality metric provided a comparison between the local in-plane strain state and the macroscopic applied strain. It was observed that the strain coaxiality values within slip bands were well aligned with the applied deformation axis, since the slip bands provided a plasticity mechanism to accommodate this deformation. More interesting, with increased applied loading cycles, the strain coaxiality values in regions between slip bands decreased, leading to an overall strain coaxiality decrease within each grain and the AOI. Grain rotation in polycrystalline materials is coupled with slip events and was quantified by comparing grain orientation information before and after loading cycles. One-to-one correlation was observed between crystal misorientations and the in-plane strain values. These trends were not observed consistently throughout, which suggests that an additional mechanism may be active, such as microplasticity or subdomain rotation between the slip bands. Further, work is needed to identify the potential grain reorientation relative to these slip bands.

In Chapter 6, two variants of RR1000, which contained planar and serrated HAGB morphologies, were studied under cyclic dwell-fatigue loading conditions, in a vacuum environment at a temperature of 700 °C. The HAGB morphologies affected each microstructure's ability to localize strain, resulting in a differing propensity to form GB cavities. The evolution of deformation with accumulated dwell-fatigue cycles indicates that serrated GBs localize strain and develop more cavities than planar HAGBs, due to key microstructural deficiencies that developed during the slow-cooling process, required to produce the serrated GBs.

The predominantly active deformation mechanisms, under the experimental loading conditions, were crystallographic slip and GB cavitation. The GB sliding magnitudes were quantified and found to be non-significant. Twice the length fraction of GB cavities were observed to form in the HSA serrated microstructure following each sequence of dwell-fatigue loading, as

compared to the HSA planar GB specimen. Plastic strain accumulations were more heterogeneous along HAGB in the serrated microstructure. Strain accumulations were, on average, 55% greater along serrated HAGBs which formed cavities versus those that did not form cavities, compared to only a 10% difference in the like comparison of planar GBs. The serrated GB variant contained both higher aspect ratio and larger γ' precipitates along the GBs, while maintaining an equivalent aspect ratio of the γ' phase within the bulk of a grain, as compared to the planar GB variant. The increased coarsening observed in the γ' phase agrees with the expected precipitation kinetics, wherein the decreased energy barrier near interfaces leads to discontinuous precipitation of secondary phases and additional time at higher temperatures results in a coarser precipitate structure.

Initial cavity formation was observed during LSA dwell-fatigue, along serrated GBs which contained coarse γ' and was denuded of the γ' phase. This GB also experienced strain localizations 5 to 10 times larger than the average AOI strain. Regions of coarse and/or denuded γ' are expected to exhibit a lower statistical strength. These regions localized deformation, resulting in GB cavity formation. Accumulation of plastic strain intensified with continued deformation causing cavities to grow and coalesce along GBs.

7.1   Future work

During the course of this thesis, the following additional experiments were conceived to investigate the covered topic further.

The first topic proposed for future research is the spatial evolution of DBs. In Chapter 4, the direction and deviation of DBs are explored. However, due to the perfectly plastic nature of the Ti7Al material, the evolution in DBs was difficult to capture. This was attempted during monotonic tensile loading, but the material yield and subsequent plastic strain accumulation occurs quickly over small deflections. It is recommended to utilize the same material under high cycle fatigue conditions (low stress, high cycle count) or change to a material that experiences appreciable hardening behavior to capture the evolution of these DBs.

The second topic proposed for future research is the occurrence and variance of behavior of grain clusters within Ni-based superalloys. Observing the measurements recorded within our study, the deformation occurring within grain clusters exists on a continuum. Many of our inter-connected slip bands extended beyond the edges of the AOI. Future work should extend the size

of the AOI, such that the impact of inter-connected slip band length can be determined. Further, GB character, specifically coherent twin boundaries, are known locations of strain localization, it would be interesting to understand if these features embedded within a grain cluster constitute a worst case scenario, in regard to strain localization.

The last topic proposed for future research is related to optimizing the GB morphology as a function of cavity formation. To fully realize the advantages of serrated GBs, the detrimental effect of cavity nucleation and coalescence must be suppressed. It is proposed to utilize a dual cooling rate scheme, wherein the material is more quickly cooled after the formation of the secondary γ'. This may eliminate regions that were denuded of the γ' phase and allow the material to retain a finer distribution of tertiary γ' along the grain boundary regions. It is proposed that this small change to the material pedigree will eliminate the primary mechanism responsible for cavity formation within our experiments. This would allow for a comparison of deformation behavior at the GB interfaces between the legacy serrated and planar material. Wherein the behavior of the proposed experiment may transmit deformation between grains, rather than form cavities at the interfaces.

REFERENCES

1   Sangid MD. The physics of fatigue crack initiation. *Int J Fatigue*. 2013;57: 58–72.

2   Mitchell RJ, Lemsky JA, Ramanathan R, Li HY, Perkins KM, Connor LD. Process Development & Microstructure & Mechanical Property Evaluation of a Dual Microstructure Heat Treated Advanced Nickel Disc Alloy. *Superalloys 2008*. 2008: 347–356.

3   Read F, Thornton W. Dislocations in crystals. *McGraw-Hill*. 1953.

4   Stoltz RE, Pineau AG. Dislocation-Precipitate Interaction and Cyclic Stress-Strain Behavior of a γ′ Strengthened Superalloy. *Mater Sci Eng*. 1978;34: 275–284.

5   Fritzemeiert LG, Tien JK. The cyclic stress-strain nickel-base superalloys-ii. behavior of single crystals. 1988;36: 283–290.

6   Clavel M, Pineau A. Intergranular Fracture Associated with Heterogeneous Deformation Modes During Low Cycle Fatiue In A Ni-Base Superalloy. *Scr Mater*. 1982;16: 361–364.

7   Huang EW, Barabash RI, Wang Y, et al. Plastic behavior of a nickel-based alloy under monotonic-tension and low-cycle-fatigue loading. *Int J Plast*. 2008;24: 1440–1456.

8   Pineau A, McDowell DL, Busso EP, Antolovich SD. Failure of metals II: Fatigue. *Acta Mater*. 2015.

9   Sangid MD, Maier HJ, Sehitoglu H. The role of grain boundaries on fatigue crack initiation – An energy approach. *Int J Plast*. 2011;27: 801–821.

10 Kikuchi M, Shiozawa K, Weertman JR. Void nucleation in astroloy: theory and experiments. *Acta Metall*. 1981;29: 1747–1758.

11 Schmid E. Yield point of crystals, critical shear stress law. In: *Proceedings of the First International Congress for Applied Mechanics, Delft.* ; 1924:342.

12 Peters WH, Ranson WF, Sutton MA, Chu TC, Anderson J. Application of digital correlation methods to rigid body mechanics. *Opt Eng*. 1983;22: 738–742.

13 Sandlöbes S, Schestakow I, Yi S, et al. The relation between shear banding, microstructure and mechanical properties in Mg and Mg-Y alloys. *Mater Sci Forum*. 2011;690: 202–205.

14 Abuzaid WZ, Sangid MD, Carroll JD, Sehitoglu H, Lambros J. Slip transfer and plastic strain accumulation across grain boundaries in Hastelloy X. *J Mech Phys Solids*. 2012;60: 1201–1220.

15 Sangid MD, Book TA, Naragani D, et al. Role of heat treatment and build orientation in the microstructure sensitive deformation characteristics of IN718 produced via SLM additive manufacturing. *Addit Manuf*. 2018;22: 479–496.

16 Davidson DL, Tryon RG, Oja M, Matthews R, Ravi Chandran KS. Fatigue Crack Initiation In WASPALOY at 20 °C. *Metall Mater Trans A*. 2007;38: 2214–2225.

17 Tang YT, Wilkinson AJ, Reed RC. Grain Boundary Serration in Nickel-Based Superalloy Inconel 600: Generation and Effects on Mechanical Behavior. *Metall Mater Trans A*. 2018.

18 Li HY, Sun JF, Hardy MC, et al. Effects of microstructure on high temperature dwell fatigue crack growth in a coarse grain PM nickel based superalloy. *Acta Mater*. 2015: 355–369.

19 Mitchell RJ, Li HY, Huang ZW. On the formation of serrated grain boundaries and fan type structures in an advanced polycrystalline nickel-base superalloy. *J Mater Process Technol*. 2009;209: 1011–1017.

20 Hatherly M, Malin AS. SHEAR BANDS IN DEFORMED METAL. *Scr Metall*. 1984;18: 449–454.

21 Sangid MD, Ezaz T, Sehitoglu H. Energetics of residual dislocations associated with slip-twin and slip-GBs interactions. *Mater Sci Eng A*. 2012;542: 21–30.

22 Dillamore IL, Roberts JG, Bush AC. Occurrence of shear bands in heavily rolled cubic metals. *Met Sci*. 1979;13: 73–77.

23 Dieter GE. Mechanical metallurgy. 1961: 615 p.

24 Morii K, Nakayama Y. Shear Bands in Rolled Copper Single Crystals. *Trans Japan Inst Met*. 1981;22: 857–864.

25 Nakayama Y, Morii K. Transmission Formation Electron Microscopy of Shear Band in Rolled Copper Single Crystals. 1982: 422–431.

26 Dève HE, Asaro RJ. The development of plastic failure modes in crystalline materials: Shear bands in Fcc polycrystals. *Metall Trans A*. 1989;20: 579–593.

27 Korbel A, Embury JD, Hatherly M, Martin PL, Erbsloh HW. ASPECTS OF STRAIN IN Al-Mg ALLOYS. *Acta Metall*. 1986;34: 1999–2009.

28 Hirth JP. The Influence of Grain Boundaries on Mechanical Properties. *Metall Trans*. 1972;3: 3047–3067.

29 Stroh AN. The Formation of Cracks as a Result of Plastic Flow. *Proc R Soc A Math Phys Eng Sci*. 1954;223: 404–414.

30 Hall EO. The Deformation and Ageing of Mild Steel: III Discussion of Results. *Proc Phys Soc Sect B*. 1951;64: 747–753.

31 Petch NJ. The Cleavage Strength of Polycrystals. *J Iron Steel Inst*. 1953;174.

32 Fromm BS, Adams BL, Ahmadi S, Knezevic M. Grain size and orientation distributions: Application to yielding of α-titanium. *Acta Mater*. 2009;57: 2339–2348.

33   Lunt D, Ho A, Davis A, et al. The effect of loading direction on strain localisation in wire arc additively manufactured Ti–6Al–4V. *Mater Sci Eng A*. 2020;788.

34   Bodelot L. Investigation of the Relationship Between Microstructural Features and Strain Localization in Polycrystalline 316 L. *Exp Mech*. 2019;59: 691–702.

35   Bache MR, Evans WJ, Suddell B, Herrouin FRM. The effects of texture in titanium alloys for engineering components under fatigue. *Int J Fatigue*. 2001;23: 153–159.

36   Book TA, Sangid MD. Strain localization in Ti-6Al-4V Widmanstätten microstructures produced by additive manufacturing. *Mater Charact*. 2016;122: 104–112.

37   Harr ME, Daly S, Pilchak AL. The effect of temperature on slip in microtextured Ti-6Al-2Sn-4Zr-2Mo under dwell fatigue. *Int J Fatigue*. 2021;147: 106173.

38   Evans WJ, Jones JP, Whittaker MT. Texture effects under tension and torsion loading conditions in titanium alloys. *Int J Fatigue*. 2005;27: 1244–1250.

39   Ashby MF. The deformation of plastically non-homogeneous materials. *Philos Mag*. 1970;21: 399–424.

40   Lund CH. Physical Metallurgy of Nickel-base Superalloys. 1961.

41   Pollock TM, Tin S. Nickel-Based Superalloys for Advanced Turbine Engines: Chemistry, Microstructure and Properties. *J Propuls Power*. 2006;22: 361–374.

42   Thompson A, Backofen W. The effect of grain size of fatigue. *Acta Metall*. 1971;19.

43   Randle V. Twinning-related grain boundary engineering. *Acta Mater*. 2004;52: 4067–4081.

44   Ewing JA, Humfrey JCW. The Fracture of Metals under Repeated Alternations of Stress. *Philos Trans R Soc A Math Phys Eng Sci*. 1903;221: 241–253.

45   Chang K-M, Henry MF, Benz MG. Metallurgical control of fatigue crack propagation in superalloys. *JOM*. 1991;42: 29–35.

46   Thompson AW, Baskes MI, Flanagan WF. The dependence of polycrystal work hardening on grain size. *Acta Metall*. 1973;21: 1017–1028.

47   Brogdon ML, Rosenberger AH. Evaluation of the influence of grain structure on the fatigue variability of waspaloy. In: *Proceedings of the International Symposium on Superalloys*. ; 2008:583–588.

48   Healy JC, Grabowski L, Beevers CJ. Monitoring Fatigue of a Nickel-Base Superalloy at Positive and Negative Stress Ratios using an Optical System. *Fatigue Fract Eng Mater*. 1992;15: 309–321.

49   Tryon RG, Dey A, Krishnan G, Chandran KSR, Oja M. Indentifying sensitive parameters at fatigue crack nucleation sites using microstructual simulation models. *Mater Damage Progn*. 2005: 105–112.

50   Sinclair G, Craig W. Influence of grain size on work hardening and fatigue characteristics of alpha brass. 1952;18.

51   Thompson AW, Backofen W. The comparison of yield and fatigue strength dependence on grain size. *Scr Mater*. 1971;5.

52   Thompson A, Backofen W. Production and mechanical behavior of very fine-grained copper. *Matallurgical Mater Trans*. 1971.

53   Buque C, Bretschneider J, Schwab A, Holste C. Effect of grain size and deformation temperature on the dislocation structure in cyclically deformed polycrystalline nickel. *Mater Sci Eng A*. 2001;319–321: 631–636.

54   Keller R, Zielinski W, Gerberich WW. On the onset of low-energy dislocation substructures in fatigue: Grain size effects. *Mater Sci Eng A*. 1989;113: 267–280.

55   Rittner J, Seidman D. ⟨110⟩ Symmetric Tilt Grain-Boundary Structures in Fcc Metals With Low Stacking-Fault Energies. *Phys Rev B*. 1996;54: 6999–7015.

56   Olmsted DL, Foiles SM, Holm EA. Survey of computed grain boundary properties in face-centered cubic metals: I. Grain boundary energy. *Acta Mater*. 2009;57: 3694–3703.

57   Sangid MD, Ezaz T, Sehitoglu H, Robertson IM. Energy of slip transmission and nucleation at grain boundaries. *Acta Mater*. 2011;59: 283–296.

58   Hosford WF, Fleischer RL. Dislocation barriers and cross slip. *Acta Metall*. 1959;7: 816–817.

59   Jin ZH, Gumbsch P, Ma E, et al. The interaction mechanism of screw dislocations with coherent twin boundaries in different face-centred cubic metals. *Scr Mater*. 2006;54: 1163–1168.

60   Carter JLW, Kuper MW, Uchic MD, Mills MJ. Characterization of localized deformation near grain boundaries of superalloy René-104 at elevated temperature. *Mater Sci Eng A*. 2014;605: 127–136.

61   Kassner ME, Hayes TA. Creep cavitation in metals. *Int J Plast*. 2003;19: 1715–1748.

62   Shinde S, Gravett P. The Effects of Dwell on the LCF Behavior of IN617. *J ASTM Int*. 2011;8: 1–11.

63   Furrer DU, Fecht H-J. Gamma Prime Formation in SUPERALLOY U720LI. *Acta Metall*. 1999;40: 1215–1220.

64   Alexandre F, Deyber S, Pineau A. Modelling the optimum grain size on the low cycle fatigue life of a Ni based superalloy in the presence of two possible crack initiation sites. *Scr Mater*. 2004;50: 25–30.

65   Detrois M, Rotella J, Hardy M, Tin S, Sangid MD. Tailoring the Properties of a Ni-Based Superalloy via Modification of the Forging Process: an ICME Approach to Fatigue Performance. *Integr Mater Manuf Innov*. 2017.

66   Danflou HL, Marty M, Walder a. Formation of Serrated Grain Boundaries And Their Effect On The Mechanical Properties In a P/M Nickel Base Superalloy. *TMS Superalloys*. 1992: 63–72.

67   Hong HU, Kim IS, Choi BG, Kim MY, Jo CY. The effect of grain boundary serration on creep resistance in a wrought nickel-based superalloy. *Mater Sci Eng A*. 2009;517: 125–131.

68   Koul AK, Gessinger GH. On the Mechanism of Serrated Grain Boundary Formation in Ni-Based Superalloys with Low γ′ Volume Fraction. *Acta Metall*. 1983;31: 1061–1069.

69   Koul AK, Thamburaj R. Serrated grain boundary formation potential of Ni-based superalloys and its implications. *Metall Trans A*. 1985;16: 17–26.

70   Knowles DM, Hunt DW. The influence of microstructure and environment on the crack growth behavior of powder metallurgy nickel superalloy RR1000. *Metall Mater Trans A Phys Metall Mater Sci*. 2002;33: 3165–3172.

71   Gifkins RC. Grain-boundary participation in high-temperature deformation: An historical review. *Mater Charact*. 1994;32: 59–77.

72   Shen Y, Li W, Sulsky DL, Schreyer HL. Localization of plastic deformation along grain boundaries in a hardening material. *Int J Mech Sci*. 2000;42: 2167–2189.

73   Lim LC. Cavity nucleation at high temperatures involving pile-ups of grain boundary dislocations. *Acta Metall*. 1987;35: 1663–1673.

74   Lim LC. Cavity nucleation at high temperatures involving pile-ups of grain boundary dislocations-effect of solutes and impurities. *Acta Metall*. 1989;37: 969–977.

75   Dyson BF, Loveday MS, Rodgers MJ. Grain Boundary Cavitation Under Various States of Applied Stress. *Proc R Soc London Ser A*. 1976;349: 245–259.

76   Greenwood JN, Miller DR, Suiter JW. Intergranular cavitation in stressed metals. *Acta Metall*. 1954;2: 250–258.

77   Gifkins RC. A Mechanism for the Formation of Intergranular Cracks when Boundary Sliding Occurs. *Acta Metall*. 1956;4: 98–99.

78   Riedel H. Cavity nucleation at particles on sliding grain boundaries. A shear crack model for grain boundary sliding in creeping polycrystals. *Acta Metall*. 1984;32: 313–321.

79   Field DP, Adams BL. Interface cavitation damage in polycrystalline copper. *Acta Metall Mater*. 1992;40: 1145–1157.

80   Abuzaid W, Sehitoglu H, Lambros J. Plastic strain localization and fatigue micro-crack formation in Hastelloy X. *Mater Sci Eng A*. 2012;561: 507–519.

81   Carroll LJ, Cabet C, Carroll MC, Wright RN. The development of microstructural damage during high temperature creep-fatigue of a nickel alloy. *Int J Fatigue*. 2013;47: 115–125.

82   Dyson BF, Rodgers MJ. Prestrain, Cavitation, and Creep Ductility. *Met Soc*. 1974;8: 261–266.

83   Kontis P, Alabort E, Barba D, Collins DM, Wilkinson AJ, Reed RC. On the role of boron on improving ductility in a new polycrystalline superalloy. *Acta Mater*. 2017;124: 489–500.

84   Hill R. Elastic properties of reinforced solids: Some theoretical principles. *J Mech Phys Solids*. 1963;11: 357–372.

85   Ozturk D, Kotha S, Pilchak AL, Ghosh S. Two-way multi-scaling for predicting fatigue crack nucleation in titanium alloys using parametrically homogenized constitutive models. *J Mech Phys Solids*. 2019;128: 181–207.

86   Yeratapally SR, Glavicic MG, Hardy M, Sangid MD. Acta Materialia Microstructure based fatigue life prediction framework for polycrystalline nickel-base superalloys with emphasis on the role played by twin boundaries in crack initiation. *Acta Mater*. 2016;107: 152–167.

87   Efstathiou C, Sehitoglu H, Lambros J. Multiscale strain measurements of plastically deforming polycrystalline titanium: Role of deformation heterogeneities. *Int J Plast*. 2010;26: 93–106.

88   Sangid MD, Rotella J, Naragani D, Park J-S, Kenesei P, Shade PA. A complete grain-level assessment of the stress-strain evolution and associated deformation response in polycrystalline alloys. *Acta Mater*. 2020;201: 36–54.

89   Balzani D, Scheunemann L, Brands D, Schröder J. Construction of two- and three-dimensional statistically similar RVEs for coupled micro-macro simulations. *Comput Mech*. 2014;54: 1269–1284.

90   Pilchak AL, Li J, Rokhlin SI. Quantitative comparison of microtexture in near-alpha titanium measured by ultrasonic scattering and electron backscatter diffraction. *Metall Mater Trans A Phys Metall Mater Sci*. 2014;45: 4679–4697.

91   Glavicic MG, Morton T, Broderick T, et al. Progress in the Advanced Titanium Microstructure and Modeling Program. *Proc 13th World Conf Titan*. May 2016: 1863–1873.

92   Mello AW, Nicolas A, Sangid MD. Fatigue strain mapping via digital image correlation for Ni-based superalloys: The role of thermal activation on cube slip. *Mater Sci Eng A*. 2017;695: 332–341.

93 Ozturk D, Pilchak AL, Ghosh S. Experimentally validated dwell and cyclic fatigue crack nucleation model for α–titanium alloys. *Scr Mater*. 2017;127: 15–18.

94 Detrois M, Rotella J, Goetz RL, Helmink RC, Tin S. A Grain boundary engineering of powder processed Ni-base superalloy RR1000 : Influence of the deformation parameters. *Mater Sci Eng A*. 2015;627: 95–105.

95 Detrois M, Rotella J, Goetz RL, Helmink RC, Tin S. The Influence of the Starting Grain Size During High-Temperature Grain Boundary Engineering of Ni-Base Superalloy RR1000. *Superalloys 2016 Proc 13th Internaltional Symp Superalloys*. 2016.

96 Buckingham RC, Argyrakis C, Hardy MC, Birosca S. The effect of strain distribution on microstructural developments during forging in a newly developed nickel base superalloy. *Mater Sci Engng A*. 2016;654: 317–328.

97 Parr IM., Jackson TJ, Hardy M, et al. INHOMOGENEOUS GRAIN COARSENING BEHAVIOR IN SUPERSOL VUS HEAT TREATED NICKEL-BASED SUPERALLOY RRIOOO. *Superalloys 2016 Proc 13th Internaltional Symp Superalloys*. 2016: 447–456.

98 GRABIT (https://www.mathworks.com/matlabcentral/fileexchange/7173-grabit), MATLAB Central File Exchange. Retrieved April 30, 2015.

99 Schneider CA, Rasband WS, Eliceiri KW. NIH Image to ImageJ: 25 years of image analysis. *Nat Methods*. 2012;9: 671–675.

100 Dong YL, Pan B. A Review of Speckle Pattern Fabrication and Assessment for Digital Image Correlation. *Exp Mech*. 2017;57: 1161–1181.

101 Nicolas A, Mello A, Sangid M. The effect of strain localization on galvanic corrosion pitting in AA7050. *Corrosion*. 2018: 2729.

102 Di Gioacchino F, Quinta da Fonseca J. Plastic Strain Mapping with Sub-micron Resolution Using Digital Image Correlation. *Exp Mech*. 2013;53: 743–754.

103 Peters WH, Ranson WF. Digital imaging techniques in experimental stress analysis. *Opt Eng*. 1982;21: 427–431.

104 Sutton M, Mingqi C, Peters W, Chao Y, McNeill S. Application of an optimized digital correlation method to planar deformation analysis. *Image Vis Comput*. 1986;4: 143–150.

105 Rosenfeld A. From Image Analysis to Computer Vision: An Annotated Bibliography, 1955–1979. *Comput Vis Image Underst*. 2001;84: 298–324.

106 Javier Esquivel. Digital Image Correlation of Heterogeneous Deformations in Polycrystallince Material with Electron Backscatter Diffraction. 2014.

107 Sutton MA, Li N, Joy DC, Reynolds AP, Li X. Scanning electron microscopy for quantitative small and large deformation measurements Part I: SEM imaging at magnifications from 200 to 10,000. *Exp Mech*. 2007;47: 775–787.

108 Sutton MA, Li N, Garcia D, et al. Scanning electron microscopy for quantitative small and large deformation measurements Part II: Experimental validation for magnifications from 200 to 10,000. *Exp Mech*. 2007;47: 789–804.

109 Kammers AD, Daly S. Digital Image Correlation under Scanning Electron Microscopy: Methodology and Validation. *Exp Mech*. 2013;53: 1743–1761.

110 Kammers AD, Daly S. Self-Assembled Nanoparticle Surface Patterning for Improved Digital Image Correlation in a Scanning Electron Microscope. *Exp Mech*. 2013;53: 1333–1341.

111 Kammers AD, Wongsa-Ngam J, Langdon TG, Daly S. The effect of microstructure heterogeneity on the microscale deformation of ultrafine-grained aluminum. *J Mater Res*. 2014;29: 1664–1674.

112 Mello AW, Book TA, Nicolas A, Otto SE, Gilpin CJ, Sangid MD. Distortion Correction Protocol for Digital Image Correlation after Scanning Electron Microscopy: Emphasis on Long Duration and Ex-Situ Experiments. *Exp Mech*. 2017: 1–15.

113 Tracy J, Waas A, Daly S. A new experimental approach for in situ damage assessment in fibrous ceramic matrix composites at high temperature. *J Am Ceram Soc*. 2015;98: 1898–1906.

114 Sutton MA, Li N, Garcia D, et al. Metrology in a scanning electron microscope: theoretical developments and experimental validation. *Meas Sci Technol*. 2006;17: 2613.

115 Rotella J, Pilchak AL, Sangid MD. Examining the pathways for deformation band formation at the mesoscale. *Mater Charact*. 2021;182: 111552.

116 Di Gioacchino F, Quinta Da Fonseca J. An experimental study of the polycrystalline plasticity of austenitic stainless steel. *Int J Plast*. 2015;74: 92–109.

117 McNelley TR, Swisher DL, Prez-Prado MT. Deformation bands and the formation of grain boundaries in a superplastic aluminum alloy. *Metall Mater Trans A Phys Metall Mater Sci*. 2002;33: 279–290.

118 Arora D, Cooper I. AN INTRODUCTION TO PERCOLATION THEORY A MATLAB SIMULATION. github. Available at: https://d-arora.github.io/Doing-Physics-With-Matlab/mpDocs/percolation.htm. Accessed July 8, 2021.

119 Niezgoda SR, Turner DM, Fullwood DT, Kalidindi SR. Optimized structure based representative volume element sets reflecting the ensemble-averaged 2-point statistics. *Acta Mater*. 2010;58: 4432–4445.

120 Fullwood DT, Kalidindi SR, Niezgoda SR, Fast A, Hampson N. Gradient-based microstructure reconstructions from distributions using fast Fourier transforms. *Mater Sci Eng A*. 2008;494: 68–72.

121 Lunt D, Orozco-Caballero A, Thomas R, et al. Enabling high resolution strain mapping in zirconium alloys. *Mater Charact*. 2018;139: 355–363.

122 Rotella J, Sangid MD. Microstructural-based strain accumulation during cyclic loading of Ni-based superalloys: The role of neighboring grains on interconnected slip bands. *Fatigue Fract Eng Mater Struct*. 2020;43: 2270–2286.

123 Taylor GI. Plastic strain in metals. *J Inst Met*. 1938: 62: 307-325.

124 Blochwitz C, Tirschler W. Twin boundaries as crack nucleation sites. *Cryst Res Technol*. 2005;40: 32–41.

125 Hirth JP. The Influence of Grain Boundaries on Mechanical Properties. *Chem Phys Met Comm AIME*. 1957;3: 1955–1957.

126 Miao J, Pollock TM, Wayne Jones J. Crystallographic fatigue crack initiation in nickel-based superalloy René 88DT at elevated temperature. *Acta Mater*. 2009;57: 5964–5974.

127 Schuren JC, Shade PA, Bernier J V, et al. New opportunities for quantitative tracking of polycrystal responses in three dimensions. *Curr Opin Solid State Mater Sci*. 2015;19: 235–244.

128 Chatterjee K, Venkataraman A, Garbaciak T, et al. Study of grain-level deformation and residual stresses in Ti-7Al under combined bending and tension using high energy diffraction microscopy (HEDM). *Int J Solids Struct*. 2016;94–95: 35–49.

129 Livingston JD, Chalmers B. Multiple slip in bicrystal deformation. *Acta Metall*. 1957;5: 322–327.

130 Hauser JJ, Chalmers B. The plastic deformation of bicrystals of f.c.c. metals. *Acta Metall*. 1961;9: 802–818.

131 Maloth T, Ozturk D, Hommer GM, Pilchak AL, Stebner AP, Ghosh S. Multiscale modeling of cruciform dwell tests with the uncertainty-quantified parametrically homogenized constitutive model. *Acta Mater*. 2020;200: 893–907.

132 Ghosh S, Shahba A, Tu X, Huskins EL, Schuster BE. Crystal plasticity FE modeling of Ti alloys for a range of strain-rates. Part II: Image-based model with experimental validation. *Int J Plast*. 2016;87: 69–85.

133 Anahid M, Ghosh S. Homogenized constitutive and fatigue nucleation models from crystal plasticity FE simulations of Ti alloys, Part 2: Macroscopic probabilistic crack nucleation model. *Int J Plast*. 2013;48: 111–124.

134 Liu Y, Zhang X, Zhu Y, Hu P. Dislocation density informed eigenstrain based reduced order homogenization modeling : verification and application on a titanium alloy structure subjected to cyclic loading Dislocation density informed eigenstrain based reduced order homogenization model. 2020.

135 Kotha S, Ozturk D, Ghosh S. Parametrically homogenized constitutive models (PHCMs) from micromechanical crystal plasticity FE simulations, part I: Sensitivity analysis and parameter identification for Titanium alloys. *Int J Plast*. 2019;120: 296–319.

136 Ozturk D. QUANTIFICATION OF DEFORMATION AND FATIGUE CRACK NUCLEATION IN TITANIUM ALLOYS USING. 2019.

137 Payton EJ. Revisiting Sphere Unfolding Relationships for the Stereological Analysis of Segmented Digital Microstructure Images. *J Miner Mater Charact Eng*. 2012;11: 221–242.

138 Follansbee PS, Gray GT. An analysis of the low temperature, low and high strain-rate deformation of Ti-6Al-4V. *Metall Trans A*. 1989;20: 863–874.

139 Bishop JFW, Hill R. A theoretical derivation of the plastic properties of a polycrystalline face-centred metal. *Philos Mag A*. 1951;42: 1298–1307.

140 Hutchinson JW. Bounds and self-consistent estimates for creep of polycrystallin materials. *Proc R Soc London Ser A*. 1976;348: 101–127.

141 Hill R. Generalized Constitutive Relations for Incremental Deformation of Metal Crystals by Multislip. *J Mech Phys Solids*. 1966;14: 95–105.

142 Hill R. The Essential and Structure for Metal of Composites Polycrystals. *J Mech Phys Solids*. 1967;15: 79–95.

143 Asaro RJ. Crystal plasticity. *J Appl Mech*. 1983;50: 921–934.

144 Sangid MD, Sehitoglu H, Maier HJ, Niendorf T. Grain boundary characterization and energetics of superalloys. *Mater Sci Eng A*. 2010;527: 7115–7125.

145 Lee TC, Robertson IM, Birnbaum HK. Prediction of slip transfer mechanisms across grain boundaries. *Scr Metall*. 1989;23: 799–803.

146 Luster J, Morris MA. Compatibility of deformation in two-phase Ti-Al alloys: Dependence on microstructure and orientation relationships. *Metall Mater Trans A*. 1995;26: 1745–1756.

147 Lim LC, Hall B. Slip-Twin Interactions in Nickel at 573K at Large Strains. *Scr Metall*. 1984;18: 1139–1142.

148 Lee TC, Robertson IM, Birnbaum HK. An in-situ transmission electron microscope deformation study of the slip transfer mechanisms in metals. *Metall Trans A*. 1990;21: 2437–2447.

149 Misra A, Gibala R. Slip transfer and dislocation nucleation processes in multiphase ordered Ni-Fe-Al alloys. *Metall Mater Trans A Phys Metall Mater Sci*. 1999;30: 991–1001.

150 Spearot DE, Sangid MD. Insights on slip transmission at grain boundaries from atomistic simulations. *Curr Opin Solid State Mater Sci*. 2014;18: 188–195.

151 Bieler TR, Eisenlohr P, Zhang C, Phukan HJ, Crimp MA. Grain boundaries and interfaces in slip transfer. *Curr Opin Solid State Mater Sci*. 2014;18: 212–226.

152 Ritz H, Dawson P, Marin T. Analyzing the orientation dependence of stresses in polycrystals using vertices of the single crystal yield surface and crystallographic fibers of orientation space. *J Mech Phys Solids*. 2010;58: 54–72.

153 Venkataraman A, Linne M, Daly S, Sangid MD. Criteria for the prevalence of grain boundary sliding as a deformation mechanism. *Materialia*. 2019;8.

154 Lieberman EJ, Rollett AD, Lebensohn RA, Kober EM. Calculation of grain boundary normals directly from 3D microstructure images. *Model Simul Mater Sci Eng*. 2015;23: 035005.

155 Rovinelli A, Sangid MD, Proudhon H, Guilhem Y, Lebensohn RA, Ludwig W. Predicting the 3D fatigue crack growth rate of small cracks using multimodal data via Bayesian networks: In-situ experiments and crystal plasticity simulations. *J Mech Phys Solids*. 2018;115: 208–229.

156 Bourdin F, Stinville JC, Echlin MP, et al. Measurements of plastic localization by heaviside-digital image correlation. *Acta Mater*. 2018;157: 307–325.

157 Qiu CL, Andrews P. On the formation of irregular-shaped gamma prime and serrated grain boundaries in a nickel-based superalloy during continuous cooling. *Mater Charact*. 2013;76: 28–34.